ULTRASHORT PULSES IN OPTICAL MICRORESONATORS WITH KERR NONLINEARITY

A Dissertation
Presented to
The Academic Faculty

By

Hossein Taheri

In Partial Fulfillment
of the Requirements for the Degree
Doctor of Philosophy
in
Electrical and Computer Engineering

School of Electrical and Computer Engineering
Georgia Institute of Technology
May 2017

Copyright © 2017 by Hossein Taheri

ULTRASHORT PULSES IN OPTICAL MICRORESONATORS WITH KERR NONLINEARITY

Approved by:

Ali Adibi, Advisor
Professor, School of ECE
Georgia Institute of Technology

Rick Trebino
Professor, School of Physics
Georgia Institute of Technology

Benjamin Klein
Professor, School of ECE
Georgia Institute of Technology

Kurt A Wiesenfeld
Professor, School of Physics
Georgia Institute of Technology

Stephen E Ralph
Professor, School of ECE
Georgia Institute of Technology

Date Approved: November 30, 2016

سعدی به لب دریا دردانه کجا یابی؟
در کام نهنگان رو گر می طلبی کامی

This thesis belongs more to my family than me.

On their behalf, it is dedicated to all men and women who sacrificed their lives for peace and justice among mankind. And to their families who had to live after them, without them.

Among them, to ***Hussain (January 10, 626 — October 10, 680 AD), son of Fatimah and Ali****, who stood up for justice, sought peace, and strove toward his ideal against all odds. And to his family. It must have been painful to walk the earth after him.*

It is hard to bear the responsibility of carrying his name. I wish this thesis was more worthy.

ACKNOWLEDGMENTS

"I tell you, the more I think it over, the more I feel that there is nothing more truly artistic than to love people."

Vincent van Gogh, Letter to his brother Theo (September 1888)

Although a PhD degree is an affidavit of some degree of resilience, perseverance, creativity, and knowledge (among other traits) for the awardee, many other individuals contribute, to difference extents, to it. It is hard to clearly pinpoint and duly acknowledge these contributions. One can only try.

First and foremost, I would like to heartily and sincerely thank my advisor, Dr. Ali Adibi, for his continued support throughout my master's and PhD studies at Georgia Tech. He is kind and personable, and at the same time highly demanding as a research advisor. He is sharp in grasping ideas, and a truly wonderful presenter and speaker. I am grateful to him for giving me the freedom and support to choose my research topic. In the capacity of the president of the OSA Student Chapter at Georgia Tech, I had a wonderful experience working with him, organizing numerous technical talks and the International Year of Light (IYL2015) workshop. During the rather long time I spent in the US and was deprived of face-to-face interaction with my parents, he was indeed a great friend and mentor whose advice and guidance greatly contributed to my transformation from an awkward college graduate to a (hopefully reasonably) professional researcher and colleague. The lessons I learned from him, I believe, will serve me for the rest of my career. I would also like to thank his wife Samineh for her kindness and hospitality over the years, and wish their children all the very best.

Then, I would like to wholeheartedly thank Dr. Kurt Wiesenfeld. His collaboration was crucial to the progress and completion of my research project. His deep curiosity about problems of science and particularly his area of nonlinear science, and his ability to break problems down to simple tractable pieces, amenable to a researcher's

interrogation, were truly instructive. It happened a lot that I raised a question and he, by asking clarifying questions, narrowed the problem down and guided me to the answer. I also learned a lot from his wise amiable character about how to collaborate effectively and how to extend one's network of long-term collaborators in academic circles. We also share a love of teaching (and relearning what we teach by looking at the same problem from different angles), calligraphy, and beautiful typesetting, i.e., LaTeX.

I would like to thank other members of my thesis reading committee, Dr. Stephen Ralph, Dr. Rick Trebino, and Dr. Benjamin Kline.

Through the years, I learned a great deal from Dr. Ralph's vibrant presentation and teaching style, his discipline, punctuality, and sense of responsibility. His optical fiber networks course is comprehensive and the material covered highly practical. I also worked with him on organizing the IYL2015 workshop at Georgia Tech, where his involvement was instrumental in the success of the program.

Dr. Trebino has always been very kind and resourceful. I was lucky to have a head start learning the fundamentals of ultrafast optics from him. His clear way of thinking about physical concepts and his ability to explain them in words always fascinated me. His knowledge of the workings of lasers and the details of ultrashort pulse measurement systems and techniques (not only FROG, but all of them) is most certainly unrivaled. I am grateful to him for hosting me in his lab, where I worked on making a complex pulse measurement setup, and for fruitful discussions about my research, particularly the phase locking model and jumps in microcomb phase spectra. I am also thankful to his wife Linda, for her kindness and help in difference capacities. I have many pleasant memories with them both.

My first introduction to lasers was through Dr. Kline's course the first summer after I joined Georgia Tech. His special way of talking about lasers in a rigorous yet fun way made me all the more interested in learning more about nonlinear optics and

lasers.

One of the Georgia Tech faculty who has my utmost respect and gratitude is Dr. Brian Kennedy. I got to know him early on in graduate school, so took all of the courses he taught during my time there, and I am glad I did that. He is an amazing theoretical physicist who understands experiments very well and has the great ability to explain things both mathematically rigorously and in simple intuitive ways. In his occasional witty remarks, he reminds his class that there is no boundary for the difficulty of a problem a graduate student dares to attack. That is great advice for a young researcher (and a necessary reminder while working out some of his homework problems). I also benefitted from insightful discussions with him about my research, particularly on seeding comb generation with a phase-modulated pump and the phase locking model.

Dr. Ali Eftekhar has been my research mentor over the years. He is quick with ideas and very affable. I learned much discussing science with him and observing the way he thinks, in terms of very simple problems, about any seemingly complicated topic. I am also grateful to his wife, Sara. They are a wonderful family and very friendly. I wish the best for them and their children.

For a large portion of my PhD (close to four years), I taught labs and classes. This opportunity gave me a venue to practice teaching labs and large classes, develop teaching material, and mentor students. It was extremely valuable in giving me solid teaching experience and allowing me to make new acquaintances within Georgia Tech. For the electrical and electronics lab, I worked with Dr. Thomas Brewer and Dr. Allen Robinson, and for the circuits and electronics course, I got to know Dr. Bonnie Ferri and Dr. Joy Harris, as well as many fellow graduate instructors. They were kind and helpful and working with them was highly rewarding. I should particularly thank Dr. Ferri whose sense of calm is contagious, who genuinely cares for her students, and who demonstrates exemplary patience and mentorship for the instructors working

under her guidance. I should also thank Dr. John Buck, who was a sounding board at multiple stages during my time at Georgia Tech and whose great example of a teacher I greatly admire.

Many other Georgia Tech and University of Tehran (where I did my undergrad) faculty have also positively impacted my graduate and undergraduate school experience over the years. In particular, I am grateful to Dr. David Citrin, Dr. Jennifer Curtis, Dr. Thomas Gaylord, Dr. Glenn Smith, Dr. Jalil Rashed-Mohassel, and Dr. Mahmoud Shahabadi. They are genuinely kind and caring individuals.

Dr. Sina Khorasani visited Georgia Tech during part of my PhD years at Georgia Tech. His kind and humble personality led to a rapid rapport and we had weekly friendly conversations about quantum mechanics and quantum optics where, obviously, he talked and I listened and asked questions. He is an extremely talented and hardworking person with great vision. I regret he could not stay longer; I am sure my research on optical frequency combs could have benefited greatly from his presence and knowledge. I thank him for his friendship and for setting a great example of dedication to science and family.

During my long PhD years at grad school, I was blessed to have wonderful friends and group members. I shared many memories with past and present group members Saeed Mohammadi, Babak Momeni, Majid Sodagar, Farshid Ghasemi, Reza Pourabolghasem, Payam Alipour, Amir Atabaki, Maysam Chamanzar, Ehsan Shah Hosseini, Murtaza Askari, Charles Camp Jr., Charles Reinke, Ali Behrooz, Qing Li, Zhixuan Xia, Arash Karbaschi, Razi Dehghannasiri, Hamed Shams Mousavi, Amir Hosseinnia, Hesam Moradinejad, Hossein and Mohammad Taghinejad, Ali Eshaghian, Sajjad Abdollah-Ramezani, Tianren Fan, Ahmad Usman, Xi Wu, and Fei Liu. I hope I haven't missed anyone. I can write line after line about the wonderful things I learned from each and every one of them, from research attitude and how to improve SEM images or MATLAB codes, to economics or history. These gentlemen are the best of

the best. I feel blessed I got to spend some of the best years of my youth with them.

I learned a great deal from Saeed Mohammadi, Ehsan Shah Hosseini, Maysam Chamanzar, Siva Yegnanarayanan, and particularly Amir Atabaki and Qing Li in the early stages of my work. For their mentorship and patience I am forevermore grateful. I also thank Reza Pourabolghasem, Razi, Majid Sodagar, Payam, Amir Hosseinnia, Hamed Mousavi, Hossein and Mohammad Taghinejad, Hesam, and Ali Eshaghian for numerous technical discussions. In multiple instances, I contacted Mohammad Soltani and Babak Momeni who left the group before and soon after I joined, and they were always responsive and patient despite their hectic schedules. They are excellent researchers, and patient and affable mentors. I am cordially thankful for their help and advice.

I was blessed by the friendship of many others, outside the group or Georgia Tech. Among them, I should mention Parsa Banihashemi, Ehsan Hosseinian, Hamidreza Hassanzadeh, Ahsan Rizvi, Amoreth Gozo, Esmaeil Esfandiari, Mehdi Kiani, Farzad Inanlou, Mohsen Sardari, Ahmad Beirami, Mojtaba Hodjat-Shamami, Arashk Norouzpour, Roozbeh Tabrizian, Mahdi Hasani, Zhe Guang, Milad Frounchi, Siavash Farzan, Hamed Koochaki, Ahmad Peivandi, Javad Feizollahi, Morteza Rezaei, Reza Abbaspour, Amirabbas Pirooz, and Rouhollah Mousavi. Ali Sazegarnejad and his wife Faezeh, Hamid Marvi and his wife Sara, and Hassan Jafarzadeh and his wife Nancy were like family to me and helped me whenever I needed them during my stay in Atlanta. Uncle Hassan and Aunt Nancy, in many occasions, did for me what my father and mother would have done if they were here with me. For that, I am indebted to them. I am also cordially grateful to my special friend, a true older brother, Zahir Momin. He is a truly hardworking and kind-hearted person and a highly-regarded radiologist.

I had the opportunity to work as a research intern at OEwaves during part of my PhD. This opportunity was made possible by Dr. Lute Maleki. For that, and for the

many things I learned from him, I am deeply grateful to him. During my time at OEwaves, I came to know him as a charismatic and able leader demanding of the best from his team while considering his employees with highest regard. Despite his busy daily schedule, he nurtures his keen interest in science by being involved in all technical aspects and levels of product development and research. The depth and breadth of his knowledge, owing to the different topics and projects he has worked on during his career—from Bose-Einstein condensates to optoelectronic oscillators and optical frequency combs—is quite amazing. At OEwaves, I worked more closely than anyone with Dr. Andrey Matsko. He is a wonderful person who, beside his great achievements as a successful and well-published researcher, is ultimately humble and friendly. He is sharp and quick in analyzing ideas, his excitement about new ideas is energizing, and his depth of knowledge and intuition in quantum optics and optical frequency combs (and in fact, any physical subject so far as I noticed) truly fascinating. For all the amazing things I learned from him, about Kerr combs, presentation, paper writing, life in academia and industry, and for our many after-hours random discussions, I am heartily grateful to him. I also benefitted from multiple discussions with Dr. Vladimir Ilchenko, who is a wonderful scientist, very creative and hands-on, and has exciting stories and lessons based on his years of experience in academia and industry. Same goes with Dr. Anatoliy Savchenkov, Dr. Wei Liang, and Dr. Danny Eliyahu, who are always willing to help and very down-to-earth. Debra, Laura, Magda, Andrea, Terri, and Danny Fung were extremely kind and supportive both before and after I joined OEwaves. With these amazing people and hardworking staff, it is no wonder why this company is doing so well. It was an honor being part of OEwaves.

During my stay in Pasadena, I also greatly enjoyed the friendship and company of Mohammad Mirhosseini, Amir Arbabi, Mahdi Hasani and his wife Negin, Gita Mahmoudabadi, Sadegh Faraji-Dana, Ehsan Arbabi and his wife Mahsa. I very much enjoyed our technical and non-technical chats with Mohammad over meals or while

walking in the city. Mahdi and Negin have been amazing friends since my time in Atlanta. Ehsan and Mahsa are exceedingly generous and were extremely helpful in different occasions. For all the wonderful moments, to all these friends I am grateful.

The staff of the School of Electrical and Computer Engineering Administrative Office at Georgia Tech are the kindest and most helpful one can ask for. I am particularly thankful to Dr. Daniela Staiculescu, who is always willing to help. I should also thank Dr. Riley, Dr. Hertling, Tasha, Jackie, Rochelle, Siri, Ashley, and Chris. Past and present assistants of Dr. Adibi, Sharon Lawrence, Maria Metheson, Kristy Moller, Janine Lyn, and Katrine Torres, were always extremely friendly and supportive. I thank them for their always ready and unreserved support.

Some of my teachers from elementary school, middle school, and high school deserve great respect and gratitude. Among them, I would like to single out my first teacher Mrs. Taryakchi, as well as my physics, math, and biology teachers Mr. Safaei, Mr. Rowshan, and Mr. Pahlavan. I feel indebted to them and how greatly they cared for us, their students, is the reason many of my friends and I were able to flourish later on at in life.

Most special thanks are due to my family. I am ultimately and infinitely grateful to my parents, Fatemeh and Hedayatollah Taheri, and my only sister Dr. Zainab and her husband Dr. Ammar Mirzaei. My parents did everything in their power to make sure my sister and I always had everything we needed to pursue our passion for science and learning. They instilled in us the determination to work hard and encouraged us to think deeply, ask questions, and look for answers, be it about science or religion. I love them and to them I owe everything.

I got interested in math and physics first by seeing my sister's interest in these subjects and through reading her books. Her diligence and sharp mind for math was inspiring since I went to kindergarten. My sister and her husband also tried really hard to fill my void for my parents during these long years despite their heavy load

of studies, night shifts at the hospital, and work. For everything they have done for me, I am deeply grateful.

I am also immensely thankful to my mother- and father-in-law, Dr. Abdollah and Monir Eskandari, who have treated me like their very own son in all these years. They have become my family in the long years of living away from my parents and only sister. Same goes with my brother- and sister-in-law Dr. Mahdi and Maryam Eskandari, their spouses, Dr. Amaneh Moulavi-Eskandari and Dr. Arjun Nair, as well as Amaneh's parents, Uncle Hassan and Aunt Debbie. And to my niece and nephew, Morteza and Laila, whose smiles light up our days. For having such wonderful family, I feel extremely blessed. To my family and to God I am thankful.

At the top of this long list of people, comes my wife, soon-to-be Dr. Mona Eskandari, who has been my most avid supporter in this long journey. Mona is the kindest, wisest, strongest, smartest, most pure-hearted, most pious, and most resourceful life-partner and friend one can ask for. Our long-distance cross-country relationship would not have worked had it not been for her wisdom, diligence, strength, and faith. We have shared countless fun moments together taking trips to different cities in the US, and she has been with me in brightest and darkest days alike. I do not know what I did in life to deserve her, but to her and to God who led me to her I am indebted and indefinitely appreciative.

Last but most certainly not least, I thank God for all the blessings He has honored me with, for my family, my good friends, and for His patience with me when He tested me and I failed, and again tested me and I failed, and yet again, He gave me another chance. The highs and lows of life in the past years have naturally given me a certain perspective over life. For that and for everything that came upon me, to my Lord, I am grateful.

TABLE OF CONTENTS

ACKNOWLEDGMENTS v

LIST OF FIGURES xv

SUMMARY xx

CHAPTER 1 OPTICAL FREQUENCY COMB GENERATION IN NONLINEAR DIELECTRIC MICRORESONATORS 1

1.1 Optical frequency combs 2
1.2 Applications of optical frequency combs 2
1.3 Optical frequency comb as a mathematical object 4
1.3.1 An offset-free optical frequency comb 5
1.3.2 Carrier envelope offset frequency 10
1.4 Self-stabilization of an optical frequency comb 12
1.5 Mode-locked lasers and microresonator-based frequency combs . . . 15
1.6 Nonlinear photonics and the prospect of microcombs 17
1.7 Microresonator-based optical frequency combs 19
1.8 Resonator types used in optical frequency comb generation 21
1.9 Frequency conversion in optical microresonators 26
1.10 Review of microresonator optics 28
1.11 Microresonator dispersion 31
1.12 Outline of the thesis 35

CHAPTER 2 ANATOMY OF PHASE LOCKING IN KERR-NONLINEAR HYPERPARAMETRIC OSCILLATIONS 37

2.1 Introduction 38
2.2 Description of frequency comb generation by coupled nonlinear equations and the Lugiato-Lefever equation 40
2.2.1 Some history 40
2.2.2 Overview of derivation 41
2.2.3 Normalization 45
2.3 Homogeneous Solutions of the Lugiato-Lefever Equation and their Modulational Instability 46
2.4 Description of Optical Frequency Combs in the Frequency Domain . 48
2.5 Injection Locking of the Pumped Mode 51
2.6 Few-mode Truncations of the LLE 53
2.6.1 Three-mode Truncation 53
2.6.2 Five-mode Truncation 54
2.7 Summary and Outlook 57

CHAPTER 3 SELF-SYNCHRONIZATION PHENOMENA IN MICRO-RESONATOR-BASED OPTICAL FREQUENCY COMBS 58
3.1 Introduction . . . 59
3.2 Is there a self-synchronization process is action in optical microcombs? 61
3.3 Reduction of the Lugiato-Lefever Equation . . . 63
3.4 Reduced Equation Fixed Points . . . 69
3.5 Stability of the Fixed Points . . . 71
3.6 Discussion . . . 73
3.7 Explanation of jumps in frequency comb phase spectrum measurements 75
3.8 Mathematical details of the derivation and stability of the reduced phase model . . . 79
3.8.1 Derivations . . . 79
3.8.2 Linear stability analysis . . . 81
3.9 Summary and Outlook . . . 83

CHAPTER 4 SOLITON FORMATION THROUGH PARAMETRIC SEEDING . . . 84
4.1 Introduction . . . 85
4.2 Seeding by pump phase modulation . . . 87
4.3 Soliton formation and manipulation . . . 90
4.4 Discussion . . . 93
4.4.1 Cavity field momentum . . . 93
4.4.2 Removing the pump modulation . . . 95
4.4.3 Thermal resonance drift . . . 97
4.5 Summary and outlook . . . 98

CHAPTER 5 HIGH-ORDER DISPERSION OPTICAL FREQUENCY COMBS IN CRYSTALLINE RESONATORS FOR OPTICAL CLOCK APPLICATIONS . . . 100
5.1 Introduction . . . 101
5.2 High-order GVD in dispersion engineered optical resonators . . . 104
5.3 Dispersive waves and phase-matching condition . . . 110
5.4 Change of repetition rate due to higher-order dispersion . . . 112
5.5 Dominant third-order dispersion . . . 116
5.6 Effect of anomalous quartic dispersion . . . 119
5.6.1 Microcombs in the presence of quadratic and quartic dispersion 119
5.6.2 Simultaneous attractors in the presence of anomalous quadratic and quartic dispersion . . . 121
5.7 Broadband NIR combs in CaF_2 for optical clock applications . . . 128

CHAPTER 6 THESIS CONTRIBUTIONS . . . 136

REFERENCES . . . 138

LIST OF FIGURES

Fig. 1.2.1 Some of the metrological applications of frequency combs. 5

Fig. 1.3.1 Optical frequency comb as a mathematical object. 9

Fig. 1.3.2 Carrier envelope phase offset and carrier envelope frequency. 12

Fig. 1.4.1 Self-referencing of an optical frequency comb using the $f-2f$ technique. 14

Fig. 1.5.1 Frequency comb generation in pulsed lasers and optical microresonators. 16

Fig. 1.7.1 Schematic showing FWM in an integrated photonic waveguide. . . 21

Fig. 1.7.2 Schematic showing frequency comb generation in a microring resonator driven by a CW laser. 22

Fig. 1.8.1 Examples of optical resonators frequently utilized in nonlinear photonics, cavity optomechanics, and quantum information, which have been particularly successfully in frequency combs studies. 25

Fig. 2.3.1 (a)-(c) CW equilibrium $\rho_{\mathrm{e}} = |\psi_{\mathrm{e}}|^2$ solutions of the LLE vs. pump magnitude F_{P}, and (d)-(f) modulational instability gain profile for different values of the detuning α. Each gain profiles in (d)-(f) corresponds to the point marked by the white dots on the $|\psi_{\mathrm{e}}|^2$ vs. F_{P} curve above it. Parameter values are (a) $\alpha = 0$, (b) $\alpha = 1.7607 = \sqrt{3.1}$, (c) $\alpha = 2.1$,(d) $(\rho_{\mathrm{e}}, F_{\mathrm{P}}) = (1.1472, 1.63)$, (e) $(\rho_{\mathrm{e}}, F_{\mathrm{P}}) = (1.05, 1.2571)$, (f) $(\rho_{\mathrm{e}}, F_{\mathrm{P}}) = (2.3, 1.595)$. In all cases, $d_2 = -0.0124$. Note the difference between the y-axis scale in (f) and that in (d) and (e). 48

Fig. 2.3.2 Steady-state frequency combs for the parameters used for the gain profiles in Fig. 2.3.1(d)-(f). (a) and (d) correspond to Fig. 2.3.1(d), (b) and (e) to Fig. 2.3.1(e), and finally (c) and (f) to Fig. 2.3.1(f). (a)-(c) show the intra-cavity field envelope while (d)-(f) are the power spectra (top column) and phase spectra (bottom column). The phase spectra show the alignment of the phases for phase-locked combs. 49

Fig. 2.5.1 Evolution of the comb teeth magnitudes and phases in the three-mode truncation of the LLE. (a) Pumped mode and sideband magnitudes. (b) The difference between the sideband magnitudes, which tend to zero soon after the comb starts evolving irrespective of the initial conditions, and confirming the power spectrum symmetry assumption. (c) Pumped mode and sideband phases. (d) The difference between the sideband phases, which tend to a constant irrespective of the initial conditions. 52

Fig. 2.6.1 Evolution of the pumped mode and sideband magnitudes and phases in the five-mode truncation of the LLE for comb parameters as in Fig. 2.3.1(d). (a) Pumped mode and sideband magnitudes. (b) Pumped mode and sideband phases. (c) Evolution of the comb teeth complex amplitudes in polar coordinates. (d) Zoomed-in version of (c) showing the complex amplitude of the first and second sidebands. While different initial conditions lead to different final phase values, the relationship $\phi_{2\mu} - \phi_{-2\mu} = 2(\phi_\mu - \phi_{-\mu})$ is always satisfied in the steady state. In the example shown here $(\phi_{2\mu}-\phi_{-2\mu})/2 = \phi_\mu-\phi_{-\mu} = -0.104\pi$. 55

Fig. 2.6.2 The exponential decay of the phase misalignment parameter $s(\tau)$ with the normalized time τ in the full LLE, as predicted by Eq. (2.6.6). The early random oscillations are due to the small power in the sidebands early on in the generation of the comb, which leads to their phase wondering. The change in the slope of $s(\tau)$ reflects the growth of the sidebands as the comb evolves and is also captured by the few-mode models shown in Figs. 2.5.1 and 2.6.1. Note the dependence of the parameter f on the sideband powers in Eq. (2.6.5). 56

Fig. 3.2.1 Evolution of a soliton pulse under the Lugiato-Lefever equation after randomizing its phase spectrum profile. 64

Fig. 3.2.2 Closer look at the phase spectrum profile of a soliton pulse. 65

Fig. 3.3.1 Numerical solutions of Eq. (3.3.6). 67

Fig. 3.4.1 Phase alignment in (a) solitons and (b) Turing rolls in the steady-state solutions of Eqs. (3.3.1) and (3.3.2) 70

Fig. 3.5.1 Non-zero eigenvalues of the equilibrium (the Jacobian matrix $\mathbf{J}$) vs. comb span for Eq. (3.3.6) for (a) uniform and (b) mode-number–dependent comb teeth magnitude profile of $a_\eta \propto \exp(-k_0|\eta|)$, $(k_0 = 0.1)$. 72

Fig. 3.7.1 Simple vector addition problem used to explain π phase jumps in optical frequency combs. 76

Fig. 3.7.2 Frequency combs with π phase jumps and soliton repulsion. 78

Fig. 4.2.1 Schematic of a resonator driven by a phase-modualted laser pump. 89

Fig. 4.3.1 Evidence of soliton formation in optical in a microresonator pumped by a phase-modulated CW laser through the nuumerical integration of Eq. (4.2.5) using the split-step Fourier transform method. 92

Fig. 4.3.2 Soliton merging under the influence of a phase-modulated pump. . 93

Fig. 4.4.1 Comparison of the adiabatic and abrupt removal of the input phase modulation. 96

Fig. 4.4.2 Mechanical analogue for the adiabatic and abrupt removal of the phase modulation. 97

Fig. 5.2.1 Second-order dispersion (D_2) (a) and residual (or integrated) dispersion curve (b) for a realistic crystalline CaF_2 resonator in the near-IR regime. 105

Fig. 5.2.2 Microcomb generated when only the second-order dispersion coefficient D_2 is considered. 107

Fig. 5.2.3 Microcomb generated when the second- and third-order dispersion coefficients, D_2 and D_3 are considered. 107

Fig. 5.2.4 Microcomb generated when the second-, third-, and fourth-order dispersion coefficients, D_2, D_3, and D_4 are considered. 108

Fig. 5.2.5 Microcomb generated when the second-, third-, fourth-, and fifth-order dispersion coefficients, D_2, D_3, D_4, and D_5 are considered. . . 108

Fig. 5.2.6 Microcomb generated when all dispersion coefficients, D_2 through D_6 are considered. Higher-order dispersion terms do not change power spectrum of the comb significantly, and can therefore be dropped for this pumping power and frequency. 109

Fig. 5.2.7 The power specturm of the microcomb shown in Fig.5.2.6 vs. wavelength, which shows a broadband NIR comb spanning more than 40 nm. 109

Fig. 5.2.8 The generated microcomb shown in Figs. 5.2.6 and 5.2.7 is stable as shown here, where it propagates stably over 50 normalized times, equal to 100 cavity photon lifetimes. 110

Fig. 5.3.1 Higher-order dispersion can lead to dispersive wave emission in optical frequency combs. 112

Fig. 5.4.1 Pulse momentum as center of mass for an optical frequency comb. . 114

Fig. 5.4.2 The relationship between pump power fluctuations and the change of pulse repetition rate in optical microresonators. 115

Fig. 5.5.1 Dispersion parameters for a magnesium fluoride crystalline resonator and the residual dispersion for two pumping points at 1553.5 nm and 1558.5 nm. 117

Fig. 5.5.2 Numerical simulations based on the LLE, performed for the residual dispersion curve shown in Fig. 5.5.1(b). 118

Fig. 5.5.3 Numerical simulations using the LLE, performed for the residual dispersion curve shown in Fig. 5.5.1(c). 119

Fig. 5.6.1 Pulse shape (left column), comb spectrum (middle column), and oscillation settling (right panel) for the cases of pure quadratic (a-c), pure quartic (d-f), and mixed quadratic-quartic GVD (g-i). . . . 120

Fig. 5.6.2 Residual dispersion in units of the pumped mode half-width at half-maximum (HWHM). 122

Fig. 5.6.3 Two competing pulses observed in the presence of both anomalous quadratic and quartic GVD. 123

Fig. 5.6.4 Two competing phase-locked combs observed in the case of the presence of both quadratic and quartic GVDs for the residual dispersion curve shown in Fig. 5.6.2 (red curve). 124

Fig. 5.6.5 There are two stable attractors for the combs shown in Fig. 5.6.4, as traced here by looking at the immediate sideband of the pumped mode. 125

Fig. 5.6.6 Derivatives of a smooth function, sech$(\cdot)$ calculated numerically using FFT, which shows the influence of periodic boundary conditions in this spectral method. 126

Fig. 5.6.7 The numerical error defined as the absolute value of the difference between the analytical derivatives and the derivatives found using FFT. 127

Fig. 5.6.8 Effect of increasing the number of points on the numerical error caused by FFT. 127

Fig. 5.7.1 Total comb power vs. pump-resonance detuning for a CaF_2 resonator with normal dispersion pumped at 795 nm. 129

Fig. 5.7.2 Comb generation using a CaF_2 resonator for use in a rubidium-based atomic optical clock. 131

Fig. 5.7.3 Residual (or integrated) dispersion curve vs. relative mode number (a) and wavelength (b), as well as second-order dispersion (D_2) (c) for a realistic crystalline CaF_2 resonator in the near-IR regime designed for use in an atomic optical clock. 133

Fig. 5.7.4 The microcomb generated with the resonator described in Fig. 5.7.3. 134

Fig. 5.7.5 Power spectrum vs. wavelength for the comb shown in Fig. 5.7.4. The generated microcomb has a span of more than 40 nm and covers 795 nm with detectable power. 134

Fig. 5.7.6 The generated comb is stable as evidenced by the spectrograms shown here. The left panel shows the intra-cavity pulse while the right panel is the power spectrum. 135

SUMMARY

A frequency comb consists of a number of equidistant discrete frequency tones. Over the last decade, optical frequency combs have become indispensable tools for molecular fingerprinting, low-phase-noise and spectrally-pure radio frequency signal synthesis, astronomical spectrograph calibration and search for exoplanets, frequency metrology, and timekeeping. While originally realized by mode-locked lasers, frequency combs have in recent years been generated in high-quality-factor Kerr-nonlinear optical resonators driven by a continuous wave (CW) laser pump. "Microcombs" hold great promise for light-weight, small-footprint, robust, and power-efficient comb sources with larger repetition rates and in frequency regimes not available to mode-locked lasers. In addition to their many practical applications, microcombs provide a rich and flexible platform for the study of nonlinear optical, quantum optical, and nonlinear dynamical phenomena.

This thesis focuses on ultrashort pulse generation in Kerr-nonlinear optical microresonators, which arise when the tones of a frequency comb oscillate in synchrony. In the first part of the thesis, I study the phase locking mechanism responsible for the emergence of sharply-peaked pulses. I introduce and analyze a novel synchronization model for mode locking in parametric frequency combs, which is also applicable to mode-locked laser systems with saturable absorbers. Based on this model, I explain recent reports of phase jumps in some measured microcomb phase spectra. With the understanding gained from the phase locking model, I also propose and analyze a new technique for reliable deterministic generation of robust microresonator-based solitons through the phase modulation of the driving CW pump. This technique (which was recently demonstrated in experiments by researchers from Moscow State University and École Polytechnique Fédérale de Lausanne) paves the path for chip-scale ultrashort pulse sources. In the final part of the thesis, I provide a detailed

analysis of the influence of higher-order chromatic dispersion of microresonators on microcombs with the goal of increasing the span and stability of generated optical frequency combs and achieving shorter pulses. Following this in-depth investigation, I show that record broadband combs can be generated in crystalline microresonators in the near infra-red regime. Such frequency combs are generated with experimentally feasible pump and resonator parameters and will provide the basis for rubidium-based atomic optical clocks. Investigation of microresonator chromatic dispersion also leads to identifying novel pulses of Gaussian shape in resonators with quartic group velocity dispersion.

CHAPTER 1

OPTICAL FREQUENCY COMB GENERATION IN NONLINEAR DIELECTRIC MICRORESONATORS

"Never measure anything but frequency."

Arthur Schawlow, quoted in T. W. Hänsch's Nobel Lecture (2005)

This chapter introduces optical frequency combs and reviews different relevant notions used in the remainder of this thesis and required for understanding the current literature. I first introduce frequency combs through their simple structural properties and applications, without reference to the comb generating source. Their structure is then mathematically derived and explained in terms of their repetition rate and carrier envelope offset phase. This closer look at frequency combs is followed by a brief review of frequency comb self referencing techniques. I then compare and contrast comb generation in mode-locked lasers with that based on parametric frequency conversion. Microresonator-based frequency comb generation is then introduced and the advantages it can add to those provided by the already-available laser-based combs are briefly discussed. Next, resonator types used for frequency comb generation and frequency conversion in such resonators are discussed and fundamentals of optical microresonators are reviewed. The closing section focuses on chromatic dispersion in whispering-gallery-mode and waveguide-based resonators, and the relation between the common dispersion description in both resonator families. The material covered in this introductory chapter are essentially a review of frequency comb basics presented in a way I find more appealing, excepting, to some extent, the final section, which has practical relevance to any experimental and theoretical study of combs. Some results presented in

this section have been used by different groups and have appeared in the literature before, but the generic approach, even though straightforward, has not been presented separately.

1.1 Optical frequency combs

A frequency comb consists of a number of (almost ideally) equidistant discrete frequencies. When viewed on the frequency axis, this set of frequencies (laser lines of small linewidth) looks very much like the teeth of a comb, hence the name *frequency comb*. As will unfold in the remainder of this chapter (and thesis), this seemingly simple and innocent physical object has intriguing properties and various applications, understanding it entails exploring a wealth of physical phenomena, and generating it requires a large toolset of engineering techniques. While a frequency comb could be generated using difference techniques (e.g., modulation of a carrier frequency, quadratic or cubic nonlinear wave mixing, or a combination thereof) and can, in principle, reside at any point on the (positive) frequency axis, this thesis is concerned mainly with combs generated through cubic nonlinear optical interaction of high-frequency laser light with the host material of a resonator (hence the adjective *optical* for frequency combs). Since the cubic or Kerr nonlinearity is the basic physical phenomenon responsible for the creation of a comb from a single-frequency continuous-wave (CW) laser in a microresonator with large quality factor (Q), frequency combs of interest to this work are as well commonly referred to as *Kerr combs* or *microcombs* in the current literature.

1.2 Applications of optical frequency combs

While optical frequency combs (OFCs), especially those based on nonlinear light-matter interactions in high-Q optical microresonators, provide a unique platform for

the study of nonlinear dynamical and nonlinear optical phenomena and are therefore intriguing from a purely scientific perspective, much of the interest optical combs have attracted originates from their broad range of applications and the improved performance (compared to currently-used techniques) they can render.

The simple structure of a frequency comb (which was described in the previous section, and will be discussed in further detail in Section 1.3) allows stabilization and precise knowledge of all of its frequency lines (*comb teeth*) for a sufficiently wide OFC. Such a "known" comb, can then be used as an *optical ruler*, enabling precise measurement of any unknown frequency which lies between a pair of comb teeth. Some of their most important applications arise from this ability empowered by OFCs. OFCs are the basis for the most accurate clocks based on precise measurement of optical atomic transitions. When a frequency is known with great accuracy, it can in principle define the unit of time and as such OFC-based time standards are expected to replace the current definition of second based on transitions in the Cesium atom. OFCs can even be utilized for investigating minuscule changes in physical constants such as the proton-to-electron mass ratio and the fine-structure constant [1]. Optical combs have enabled high-precision calibration of astronomical spectrographs and have been used for astronomical observations and planet search. Molecular spectroscopy and remote chemical sensing have also seen remarkable advances owing to OFCs. In spectroscopy, in particular, OFCs hold great promise and techniques such as dual-comb spectroscopy allow rapid spectroscopic measurements in a wide range of frequencies including the important mid-infrared (mid-IR) regime where many molecules have strong finger-prints. LIDAR (higher-resolution counterpart of RADAR) and real-time distance measurement are among OFC applications which are attracting more interest recently, for example for self-driving cars or surveillance applications. The comb teeth in the broad spectrum of a frequency comb can be utilized as telecommunication channels. The superior frequency stability of these frequency lines has

been exploited to demonstrate high-bit-rate data transmission, signifying and upholding the potential of OFCs for improving telecommunication network capacities. The beating frequency of adjacent comb teeth of stable OFCs has been used to generate high-spectral-purity radio frequency (RF) signals with superior phase noise compared to electronic RF sources. Line-by-line shaping of a comb spectrum (adjusting each line's intensity and phase) can be used for the generation of arbitrary waveforms, which, among others, can be utilized for coherent control, where chemical processes sensitive to the intensity and phase of an external pulse can be controlled. Finally, phase-synchronized (i.e., phase- or mode-locked) frequency combs can be used for medical applications such as eye or skin surgery. For a list of references for these applications, the reader can refer to [1].

Some of the applications counted above require high precision and accuracy (e.g., optical clocks and low-phase-noise microwave generation) while some others ask for robustness and simplicity (such as arbitrary waveform generation and LIDAR). For the former group, a wide-band comb is needed (so it can be self-referenced, see Section 1.3), but only a few comb teeth will be utilized in the desired application. In contrast, for the second set of applications a modest spectral span is sufficient, while all of the comb teeth will be used. This notion is emphasized in Fig. (1.2.1).

1.3 Optical frequency comb as a mathematical object

The applications briefly discussed in the preceding section did not concern the reader with the source which generated the OFC. In this Section, I will continue to keep the reader in a state of oblivion or disregard for the source of the frequency comb and have a closer look at the characteristic features of the structure of a frequency comb. This discussion will introduce the two main frequencies which define an OFC, the *repetition rate* (f_{rep}) and the *carrier envelope offset frequency* (f_{CEO}), and hint

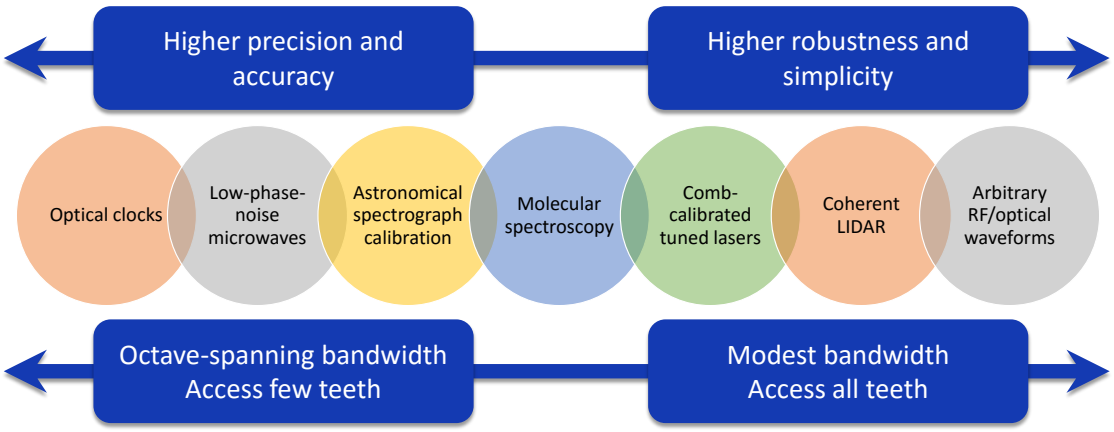

Fig. 1.2.1: Some of the metrological applications of frequency combs. The arrows at the top and bottom indicate the significance of frequency comb attributes in terms of accuracy, robustness, simplicity, spectral coverage, and the portion of comb (or number of comb teeth) exploited in the relevant application. For instance, optical clocks use only a few of the comb teeth near the optical clock laser frequency, molecular spectroscopy uses many more comb teeth (ideally all of the comb teeth across the molecular lines of interest), whereas arbitrary RF and optical waveform generation uses the entirety of the available comb teeth. This diagram is inspired by [2].

at the link between them. This will lay the foundations for the next Section on comb stabilization and self-referencing.

In what follows, we will first consider the simpler special case in which the carrier envelope offset frequency is zero. The influence of a non-zero f_{CEO} is included in a second step.

1.3.1 An offset-free optical frequency comb

Before we begin, I will review a few results from Fourier analysis, which will come in handy multiple times along the way in this Section. The purpose is merely to give the reader who has already seen these results a memory refresher and one who may not have prior familiarity with these results reassurance that the steps taken in the analysis provided in this Section have solid footing. As such, the review statements

will be ultimately brief. The reader can refer to [3] or other standard texts which deal with Fourier analysis and its applications for more heedful definitions and proofs.

First, let's recall the "convolution theorem" which states that multiplication in one domain translates into convolution in the conjugate domain of the Fourier transform. Next, the Fourier transform of a train of Dirac delta functions is itself a train of Dirac delta functions. Different names and notations are used for this train. I will denote it with the $\text{Ш}_T(t)$,

$$\text{Ш}_T(t) = \sum_{m=-\infty}^{+\infty} \delta(t - mT), \tag{1.3.1}$$

where T is the time period such that $\text{Ш}_T(t+T) = \text{Ш}_T(t)$, and $\delta(\cdot)$ is the Dirac delta function. The function $\text{Ш}_T(t)$ is called the impulse train, the sampling function, the Shah function, or the Dirac comb. Because the Dirac comb is periodic, it can be written as a Fourier series,

$$\text{Ш}_T(t) = \frac{1}{T} \sum_{n=-\infty}^{+\infty} \mathrm{e}^{\mathrm{i}n\frac{2\pi}{T}t}. \tag{1.3.2}$$

Additionally, its Fourier transform exists and, interestingly, is another Dirac comb, namely,

$$\mathcal{F}\{\text{Ш}_T(t)\} = \frac{1}{T}\text{Ш}_{1/T}(f) = \sum_{n=-\infty}^{+\infty} \mathrm{e}^{-\mathrm{i}n\,2\pi T\,f}. \tag{1.3.3}$$

After this brief digression, let's get back to the normal flow of the discussion.

Let's remember, at the outset, that an optical pulse $p(t)$ has a carrier frequency and an envelope. The electromagnetic wave of the pulse can mathematically be written as the product of the carrier wave and the envelope: $E(t) = p(t) \times \cos(\omega_c t)$, where $p(t)$ is the pulse envelope and ω_c is the carrier frequency. Using the convolution theorem, the influence of the carrier frequency in the frequency domain is to shift the center frequency of the pulse envelope transform from zero to the carrier frequency. Consequently, the carrier frequency, no matter how large it may be for an optical pulse, can be ignored so far as one is concerned with the pulse shape (envelope). Therefore, in the figures throughout this thesis and in the frequency comb literature,

the spectrum of a comb is commonly drawn around zero frequency (or, zero mode number), and the existence of an offset carrier frequency (or, its corresponding mode number in the optical resonator) is to be understood. Nonetheless, as will become clear shortly, the carrier envelope can indeed not be left out, especially when an OFC is to be considered in its entirety and put to practice.

In general, the Fourier transform of a single isolated pulse constitutes a continuum of frequencies. As soon as one looks at a train of pulses (i.e., a periodic waveform of, naturally, infinite length), however, the frequency spectrum will change into a discrete set of frequencies. The mathematical structure of such a train of pulses can be described in both the time and frequency domain using the Dirac comb. In particular, an infinite train $p_T^{\text{train}}(t)$ made of T-shifted copies of a pulse envelope $p(t)$ can be written as

$$p_T^{\text{train}}(t) = \sum_{m=-\infty}^{+\infty} p(t - mT) = \text{Ш}_T(t) \star p(t), \tag{1.3.4}$$

where the $\star$ denotes convolution. Exploiting the convolution theorem, the Fourier transform of $p_T^{\text{train}}(t)$ is equal to the product of the Fourier transforms of the impulse train and the pulse envelope; see Fig. (1.3.1). But the Fourier transform of the impulse train is another impulse train, see Eq. (1.3.3). As a result, an infinite train of equally-spaced pulses in the time domain is an equally-spaced train of Dirac delta functions in the frequency domain in which the "height" of each spike is determined by the Fourier transform of the pulse shape (envelope) at the discrete spike locations.

In the preceding discussion, we have assumed that the pulse train is infinite, starting at $t = -\infty$ and continuing till $t = +\infty$. However, this can never happen in practice. A pulse train appears at the out through the partially reflecting mirror of a laser cavity shortly after the laser warms up and mode locking takes place and disappears when the laser is turned off. In a simplified model, the infinite train of pulses is multiplied by a rather long rectangular window in the time domain with a width equal to the time difference between the laser switch-on and switch-off moments

(imagine switch on and off lead to abrupt turn on and off of the pulses). Mathematically speaking, the pulse train we dealt with so far should be multiplied by $\text{rect}(t/\tau_w)$, where τ_w is much larger than the pulse width as well as the temporal separation of the pulses. Again, the convolution theorem of Fourier analysis tells us that in the frequency domain, the Fourier transform of the $\text{rect}(t/\tau_w)$, which is $\tau_w \text{sinc}(\tau_w f)$, will be convolved with the Fourier transform of the pulse train. What will change as a result? Each Dirac delta function will be replaced with a very thin sinc function. This means each comb tooth will have a finite width. In practice. other physical sources will also contribute to a finite linewidth for each tooth in the frequency comb and their influence masks that of the realistic finite duration of the pulse train.

The discussion of the preceeding paragraph was meant to reassure the reader that the finite length of a real pulse train can be put aside for almost all cases of interest to this thesis. It is worth noting that definitions for the $\text{rect}(\cdot)$ and $\text{sinc}(\cdot)$ functions used in this Section follow those of [3].

Finally, it is worth noting that although I have talked about a "pulse" in this Section, no notion of phase synchronization and mode locking is necessary for the forgoing discussion to hold, so long as one is talking about a frequency comb spectrum in steady state. Although a pulse will not form when the comb teeth are not oscillating synchronously, the output waveform (which includes the superposition of all of the comb teeth powers and phases) will still be periodic and hence the analysis presented herein will still be applicable. Even when the comb is in a chaotic state and the resonator output cannot be considered periodic, a frequency comb, i.e., an array of discrete frequencies, will proudly exist, quite indifferently of its time-domain appearance.

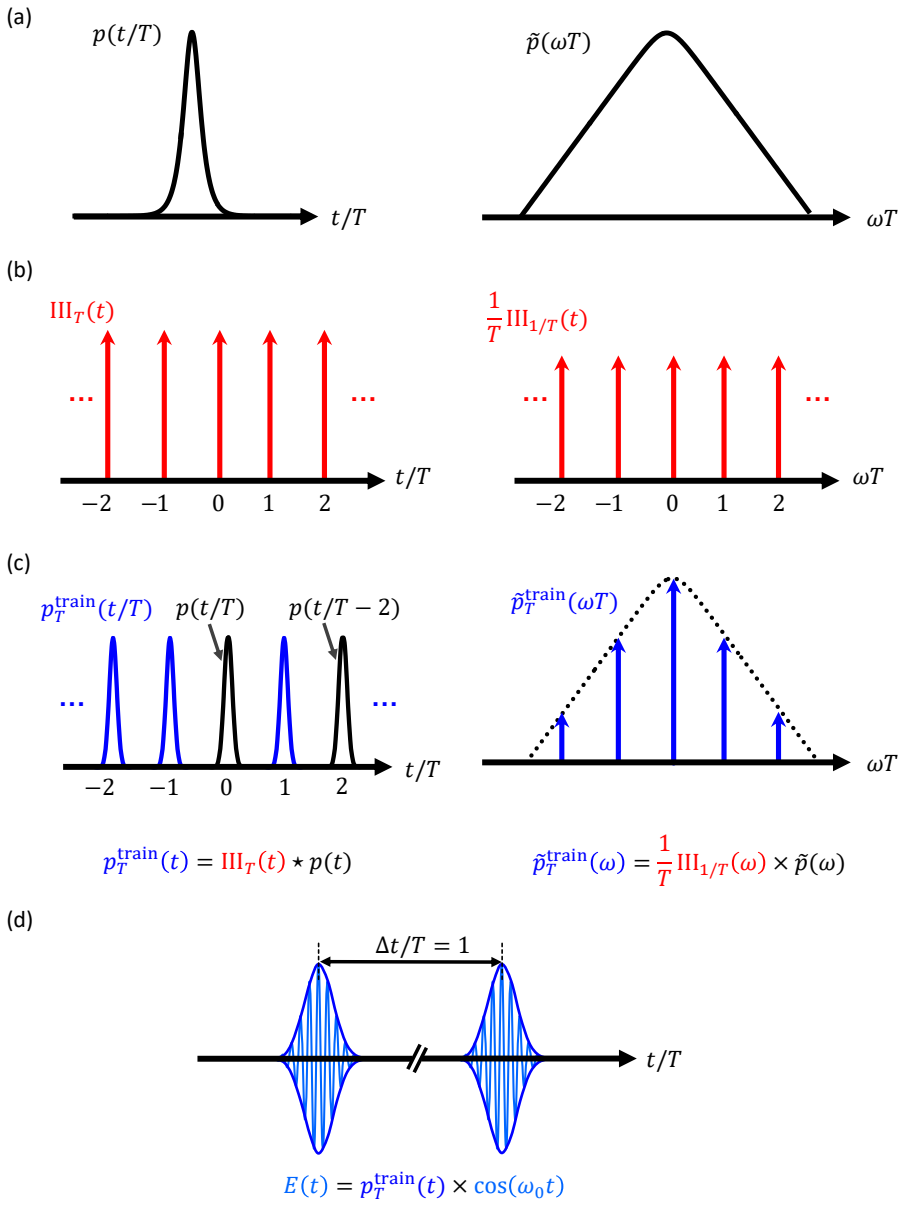

Fig. 1.3.1: Optical frequency comb as a mathematical object. (a) The Fourier transform of a single pulse $p(t)$ (left) includes a continuum of frequencies (right). The parameter T is an arbitrary constant with units of time while ω is frequency. (b) The Fourier transform of a periodic impulse train is yet another impulse train in the frequency domain. Here, T is the temporal period of the impulse train. (c) An infinite pulse train, mathematically, can be considered the result of the convolution of the pulse envelop (left panel in (a)) and the temporal impulse train (left panel in (b)). In the frequency domain, the continuous spectrum of the pulse envelope (right panel in (a)) should multiply the frequency impulse train (right panel in (b)). (d) In (a)-(c), the carrier frequency was ignored. The effect of the carrier frequency is to shift the center frequency of the comb spectrum (position of the spectral peak in the right panel in (c)) from zero to the carrier frequency.

1.3.2 Carrier envelope offset frequency

The foregoing treatment essentially ignored the carrier frequency. The hidden simplifying assumption was that the peak of the pulse train envelope is always aligned with the peak of the carrier sinusoid during one of the periods of the carrier (Fig. 1.3.1(d)). That fortunate concurrence is not always going to happen, as seen in Fig. 1.3.2(a). Here, I will include the forlorn carrier $\omega_{\rm c}$ into the analysis and comment on its practical importance.

To account for the phase offset between the envelope and carrier, one can write the electric field of the pulse train $E(t)$ in terms of the pulse envelope $p(t)$ with carrier frequency $\omega_{\rm c}$ (i.e., $p(t)\exp(\mathrm{i}\omega_{\rm c}t)$) and a phase $\phi_{\rm CEO} = \phi_0 + n\Delta\phi_{\rm CEO}$ for the nth pulse in the train. (This generalization will take into account the phase difference mentioned earlier.) Hence,

$$E(t) = \sum_n p(t-nT)\exp[\mathrm{i}(\omega_{\rm c}t - n\omega_{\rm c}T + \phi_0 + n\Delta\phi_{\rm CEO})]. \tag{1.3.5}$$

Let's define the (continuous-time) Fourier transform through $\tilde{g}(\omega) = \int_{-\infty}^{\infty} g(t)\exp(\mathrm{i}\omega t)\mathrm{d}t$ for a generic function $g(t)$. Fourier transform of the previous expression for $E(t)$ leads to

$$\begin{aligned}\tilde{E}(\omega) &= \exp(\mathrm{i}\phi_0)\tilde{p}(\omega-\omega_{\rm c})\sum_n \exp[\mathrm{i}n(\Delta\phi_{\rm CEO} - \omega T)] \\ &= \exp(\mathrm{i}\phi_0)\tilde{p}(\omega-\omega_{\rm c})\sum_n \delta(\omega T - \Delta\phi_{\rm CEO} - 2\pi n).\end{aligned} \tag{1.3.6}$$

In going from the first line to the second, we have made use of Eq. (1.3.3). The latter expression means the spectrum of the pulse train will comprise a frequency comb at frequencies where the argument of the Delta function under the summation vanishes, i.e.,

$$\omega_n = \frac{\Delta\phi_{\rm CEO}}{T} + n\frac{2\pi}{T}. \tag{1.3.7}$$

Hence, the carrier envelope phase leads to an offset frequency, from the equidistant

grid of frequencies separated by $1/T$ and starting from zero, equal to $\Delta\phi_{\mathrm{CEO}}/T$ for each frequency of the pulse train.

I am afraid the story is not over yet. There is one consistency check we should do: the electric field is a continuous function, and therefore going from one comb envelope peak (on the carrier wave) to the next, there should be an integer number of carrier frequency cycles, i.e.,

$$\omega_{\mathrm{c}}T - \Delta\phi_{\mathrm{CEO}} = 2\pi m, \tag{1.3.8}$$

where m is an integer. Hence,

$$\omega_{\mathrm{c}} = \frac{\Delta\phi_{\mathrm{CEO}}}{T} + m\frac{2\pi}{T}. \tag{1.3.9}$$

Comparison of this equation with Eq. (1.3.7) shows that the carrier frequency itself should be on tooth of the OFC.

To summarize, the frequencies of an OFC can be written as

$$f_n = f_{\mathrm{CEO}} + nf_{\mathrm{rep}}, \tag{1.3.10}$$

where

$$f_{\mathrm{CEO}} = \frac{\Delta\phi_{\mathrm{CEO}}}{2\pi T} = \frac{\Delta\phi_{\mathrm{CEO}}}{2\pi}f_{\mathrm{rep}} \tag{1.3.11}$$

is the offset frequency of the comb from zero frequency and

$$f_{\mathrm{rep}} = 1/T \tag{1.3.12}$$

is the repetition rate, c.f. Eq. (1.3.7). This is the expression I had promised at the beginning of Section 1.3. While an OFC comprises frequencies in the optical regime, each of its frequencies can be defined in terms of only two frequencies f_{CEO} and f_{rep}, which are smaller frequencies. For femto-second lasers these frequencies are usually in the RF regime. For microresonator-based OFCs they can be larger, up to THz, depending on the resonator size. For a similar treatment with further details, the reader can refer to [4].

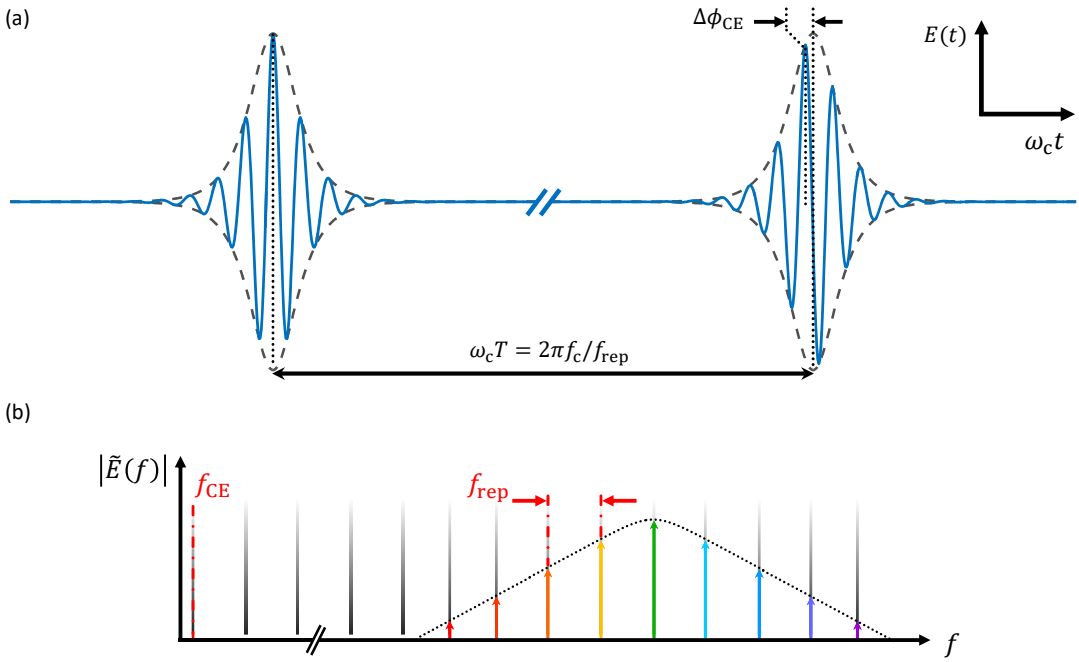

Fig. 1.3.2: Carrier envelope phase offset and carrier envelope frequency. (a) The carrier wave, in general, has a phase offset with respect to the pulse envelope; if the peak of the pulse envelope is aligned with the maximum value of the carrier sinusoid for one pulse, it will not, generally, keep this synchrony in the following pulse. The carrier envelope phase offset originates from the difference between group velocity and phase velocity. (b) The carrier envelope offset phase can easily be included in the mathematical description of a frequency comb (see text), and shown to be proportional to the offset frequency of the frequency comb from zero: if the comb is virtually extended toward the zero frequency, there will, generally, be an offset from the origin, smaller than the repetition rate and given by Eq. (1.3.11).

1.4 Self-stabilization of an optical frequency comb

Any frequency of an optical frequency comb can be identified in terms of the two frequencies f_{CEO} and f_{rep}, as prescribed by Eq. (1.3.10). If these two frequencies are measured, then all frequencies of the comb are known. While frequencies of an OFC are in the optical range, the carrier envelope offset frequency and repetition rate are

much smaller and commonly in a range measurable by electronic equipment (e.g., up to few tens of GHz, if the resonator the frequency comb is made in is not *too* small). The measurement of the repetition rate is rather straightforward. It is equal to the beating frequency of any two adjacent frequencies in the comb and be measured using a (*fast*) photodetector (PD). The carrier envelope offset frequency, on the other hand, is not so easy to measure. Let's recall that this frequency is in fact the offset from zero frequency of a fictitious extension of the comb down toward DC ("direct current", a term borrowed from electronics) frequencies. To measure f_{rep}, a technique known as the $f-2f$ is used, Fig. 1.4.1. A frequency $f_m = f_{\text{CE}} + mf_{\text{rep}}$ on the low-frequency side of the comb skirt is passed through a nonlinear $\chi^{(2)}$ media and, through second-harmonic and sum-frequency generation (SHG and SFG, respectively), a tone equal to $2f_m = 2f_{\text{CE}} + 2mf_{\text{rep}}$ is generated. Another frequency $f_{2m} = f_{\text{CE}} + 2mf_{\text{rep}}$ on the high-frequency side of the comb skirt is then sent with the latter doubled frequency to a photodetector. The beating of these two frequencies reveals the missing carrier offset frequency

$$2f_m - f_{2m} = 2f_{\text{CE}} + 2mf_{\text{rep}} - (f_{\text{CE}} + 2mf_{\text{rep}}) = f_{\text{CE}}. \tag{1.4.1}$$

If the two defining frequencies of a comb, f_{CE} and f_{rep}, are measured, it is called *self-referenced*. The $f-2f$ technique assumes that the comb is so wide that two frequencies separated from each other by a factor 2 are part of it. This assumption poses technical challenges, as the width of a physical comb is always limited; beyond certain frequencies, on both ends, the comb is soaked in noise. Only frequencies above the noise level could be measured and if a tone is to be used for the carrier offset measurement it should be strong enough to cause nonlinear interactions when passing through a quadratic nonlinear media and not so weak to be seen by the PD as well. These considerations hint at one of the major expectations of a frequency comb in metrology applications: a wide span. In particular, for self-referencing using the $f-2f$ method, the comb should at least cover one octave (from one frequency up to another,

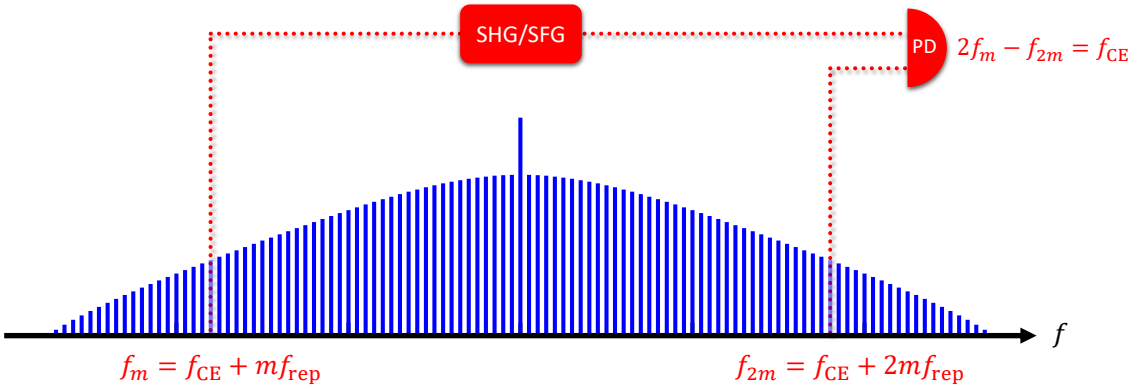

Fig. 1.4.1: Self-referencing of an optical frequency comb using the $f - 2f$ technique. If the optical frequency comb is wide enough that there is detectable power in two comb teeth in its skirt separated by an octave, the smaller frequency f_m can be doubled and passed through a photodetector with the larger frequency f_{2m}. This method will resolve the unknown carrier envelope offset frequency, as noted in Eq. (1.4.1). Similarly, $f_{\rm CE}$ might be found using the $2f - 3f$ technique, as described in the text. This surrogate method will require more power in the lower frequency which is to be tripled using a cubic nonlinear material, but the comb span can be smaller than octave-spanning.

twice as large), i.e., be an *octave-spanning* frequency comb. One can think of other similar techniques which require a smaller comb span. For instance, if a frequency f_m on the lower-side of the comb is tripled (using a cubic nonlinear medium) and another f_n is doubled (in a quadratic medium), and if $3m = 2n$, then $f_{\rm CE}$ can again be found, and instead of an octave-spanning comb, one spanning three quarters of an octave could be self-referenced. However, such techniques cannot always be easily implemented, as, e.g., nonlinear effects based on quartic and quintic wave mixing processes (that is, involving $\chi^{(4)}$ and $\chi^{(5)}$ nonlinear susceptibilities) need exceedingly higher powers. The discussion in this Section highlights one of the "*holy grails*" of frequency comb technology, i.e., octave-spanning combs.

1.5 Mode-locked lasers and microresonator-based frequency combs

So far, I have made no mention of the specific source generating the pulse train (or equivalently, the frequency comb). An OFC can be generated by a pulsed laser, more commonly referred to as *mode-locked* lasers. In fact, from a historical perspective, optical frequency combs were originally demonstrated and studied in the context of mode-locked femto-second lasers and utilized in a broad range of applications (Section 1.2 and Fig. 1.2.1) before their realization based on parametric frequency generation in optical microresonators [5–7]. Among the most prominent achievements of frequency combs in terms of their applications were laser-based spectroscopy and frequency metrology (i.e., the measurement of absolute optical frequencies with unrivaled precision [8], which led also to the demonstration of optical atomic clocks [9]). It was these outstanding results based on mode-locked laser combs which earned Theodor W. Hänsch[1] and John L. Hall (a share of) the 2005 Nobel Prize in physics for

> "contributions to the development of laser-based precision spectroscopy, including the optical frequency comb technique."

A pulsed laser consists of three essential elements: a laser cavity, a gain medium, and a saturable absorber, Fig. 1.5.1(a). The laser cavity has multiple modes in the gain bandwidth of the gain medium, so that many modes start lasing in the cavity. The saturable absorber serves to make these modes oscillate synchronously (or, in more technical terms, *mode lock*) and generate sharply-peaked bursts of electromagnetic radiation, i.e., pulses. The pulses are out-coupled through the partially reflecting

[1] The spellings Hansch or Haensch might be preferred over Hänsch in an English text, because the character ä does not technically exist in the English alphabet. However, I use the original German form because this use is now common in the literature for names of individuals. Same policy is adopted for similar situations in this thesis, e.g., for Schrödinger.

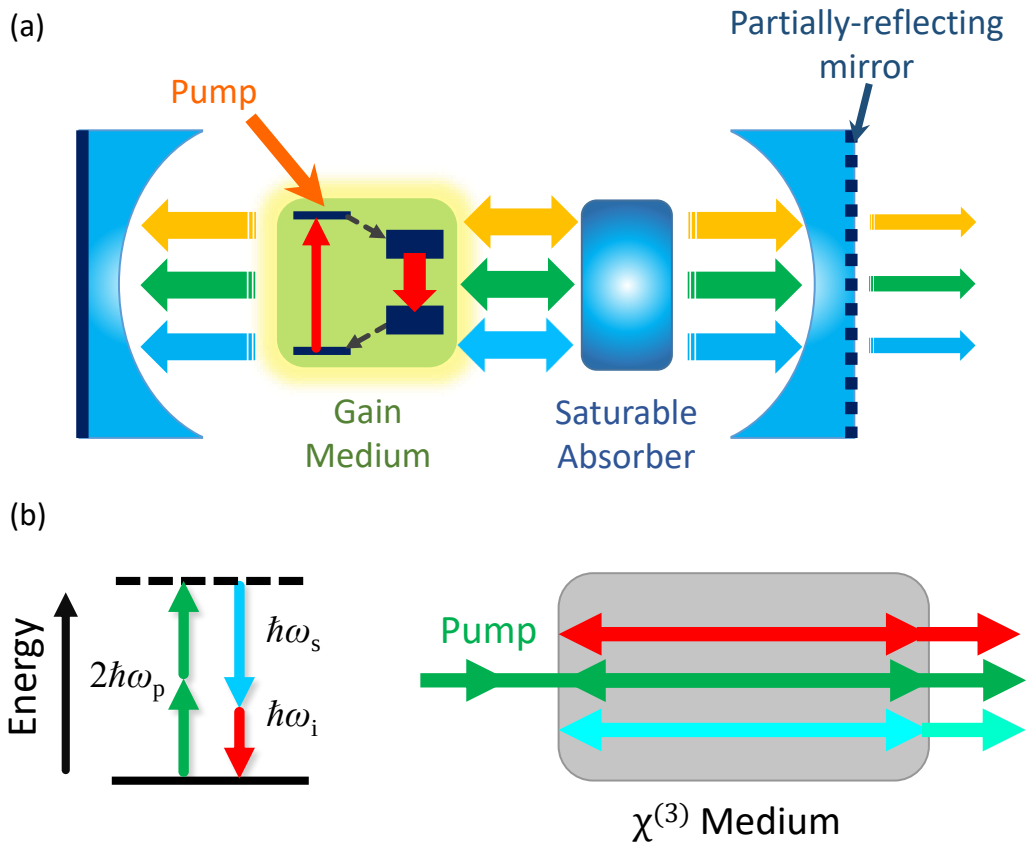

Fig. 1.5.1: Frequency comb generation in pulsed lasers and optical microresonators. (a) A mode-locked pulsed laser with a laser cavity, a gain medium which is pumped to create population inversion, and a saturable absorber. A saturable absorber makes mode-locked laser oscillation and pulse generation possible. (b) Frequency comb generation based on parametric frequency conversion in a $\chi^{(3)}$-material. The cubic nonlinear material leads to the generation of new frequencies from the pump frequency. In this process, signal and idler photons are generated at the expense of two pump photons. The generated signal and idler frequencies can then interact with each other and with the pump through the nonlinear media to generated new frequencies given their intensities are high enough and they can meet the phase-matching condition.

mirror to generate pulse train (a "mode-locked" frequency comb). Historically, femtosecond pulsed lasers have been the conventional devices for OFC generation.

One can replace the saturable absorber with a small block of Kerr-nonlinear material and an aperture. This is referred to as Kerr-lens mode-locking (KLM). The Kerr medium provides an intensity-dependent refractive index such that the central part of the beam inside the laser cavity feels a larger refractive index than the out parts.

This effect focuses the beam, which is then filtered by the aperture; the outer lower-intensity parts of the beam feel larger losses. As a result, an intensity-dependent loss, similar to a saturable absorber, is emulated. The advantage of KLM compared to a saturable absorber is that the response time of a Kerr medium is very fast; it is practically instantaneous for most applications and therefore passive KLM is superior to mode locking based on saturable absorbers.

Now, if the laser cavity and gain medium could be replaced by a resonator made of Kerr-nonlinear material and pumped by an external continuous-wave laser pump, a procedure similar to what happens in pulsed laser will occur. In this case, instead of gain provided by population inversion in the gain medium, parametric gain will lead to the generation of new frequencies. Two pump photons are annihilated to give rise to one photon of higher energy and another of lower energy (signal and idler), Fig. 1.5.1(b). If the losses of the resonator are sufficiently low such that the intensity of the generated signal and idler waves can increase, they can interact with each other as well as with the pump through the nonlinear material of the resonator. This process will lead to the generation of yet other frequencies. Conservation of energy and momentum ensures equal spacing between the subsequent generated frequencies. This notion will be visited in further detail in Section 1.9.

It is worth noting that while OFC generation based on parametric frequency conversion is now slowly but confidently claiming the achievements of frequency combs based on mode-locked lasers, the two approaches to comb generation should in fact be considered complementary, see Section 1.7.

1.6 Nonlinear photonics and the prospect of microcombs

Microresonator-based OFC generation, as noted in the previous section, relies on nonlinear optical processes. Nonlinear optics is concerned with the interaction of matter

with light of high intensity. The intensities required for nonlinear optical effects in typical materials are so high that their observation in the laboratory had to await the invention of the laser in the second half of the twentieth century. It was the high intensity and coherence of lasers which allowed the observation of second harmonic generation by Franken *et al.* in 1961 [10]. Ever since, a myriad of nonlinear optical phenomena have been discovered and studied theoretically and experimentally. These phenomena include sum and difference frequency and third harmonics generation, self- and cross-phase modulation, four-wave mixing (FWM), and stimulated Raman and Brillouin scattering, to name some. These effects have been studied using both classical electrodynamics and quantum optics [11, 12].

Different material platforms have been explored and improved for optical applications. Extremely low-loss crystalline resonators have been developed for quantum and nonlinear optical applications [1, 13, 14]. Additionally, the advancement in fabrication techniques, which have matured since the advent of the transistor technology, has made available low-loss materials that can be patterned and etched at the sub-micron level to yield compact low-cost electronic and optical devices, including integration of multiple functionalities on a single chip, the so-called *monolithic* devices. Waveguides, resonators, and gratings are the fundamental elements, or Lego pieces, of photonics and have enabled the demonstration of fundamental operations such as guiding, bending, delaying, and filtering of electromagnetic waves. Light confinement in these low-loss micron-sized optical devices enhances light-matter interaction. Benefiting from the luxuries of modern fabrication technology and the large body of knowledge in nonlinear and quantum optics, photonics—the science and technology of generation, control, and detection of photons—is poised to unleash the great potentials of nonlinear optics towards novel, low-cost, compact, and energy-efficient applications of light in addressing the ever-increasing demands of information technology, metrology, and instrumentation [15].

Of areas where nonlinear phonotics is having salient impact are all-optical signal processing, ultra-low-power all-optical switching, quantum photonics, cavity optomechanics, and optical frequency comb generation where basic photonic elements such as waveguides, resonators, gratings, and devices based on them (e.g., couplers, Y-junctions, Mach-Zehnder interferometers, etc.) enable various functionalities [1, 15–17]. Utilizing the quasi-instantaneous Kerr optical nonlinearity (resulting from the third-order nonlinearity, $\chi^{(3)}$, of a material) can provide all-optical signal processing at the femto-second time-scale and obviate the current power-hungry optical-electrical-optical conversion in optical networks. Photonic crystal microcavities and microring resonators have been used for power-efficient all-optical switching based on dispersive or absorptive optical bistabilities [18, 19]. Integrated photonic devices are also ideal candidates for quantum signal processing, quantum communication, and quantum computing where nonlinear effects have enabled many encouraging demonstrations including heralded single-photon sources, entangled photon sources, and integrated quantum frequency conversion ([20, 21], see also [15] and references therein). Among these areas, optical frequency comb generation, in particular, relies strictly on resonators with high quality factors [1].

1.7 Microresonator-based optical frequency combs

If the intensity of the electromagnetic wave (light beam) in a waveguide made of Kerr-nonlinear dielectric materila is high enough, and if the requirement of phase matching can be satisfied [11, 22], nonlinear wave mixing will lead to the generation of new frequencies. Integrated photonic devices, such as the simple waveguide shown in Fig. (1.7.1), offer the flexibility crucial to effective nonlinear interactions like dispersion and material engineering, and effective nonlinear modal area reduction. If the waveguide is bent onto itself and formed into a resonator, nonlinear interaction

processes can occur at reduced power thresholds, Fig.(1.7.2). Because of the small losses and field enhancement in a high-Q resonator, the generated frequencies can give rise to other new frequencies. This cascaded process will result in multiple (and in practice, hundreds and even thousands of) frequencies. While for nonlinear frequency conversion in a waveguide two signals (pump and signal) are necessary, in a high-Q optical resonator one single pump frequency can ignite the process, Fig.(1.7.2).

The optical comb thus generated has the same structure as one based on a mode-locked laser, and comes, in addition, with some distinctive advantages. One of the main distinctions is the possibility of making combs with larger repetition rates, in the few tens of GHz to THz range, which is more than one order of magnitude larger than common mode-locked laser combs. High-repetition-rate combs are required for different applications, such as low-phase-noise microwave generation, spectral line-by-line pulse shaping and waveform synthesis, and high-capacity optical telecommunication. The repetition rate is inversely proportional to the laser cavity length: $f_{\mathrm{rep}} = 1/T = c/2L$, where L is the cavity length and c is the speed of light, and it has been assumed that the length of the gain medium inside the cavity is small compared to L. Increasing the repetition rate amounts to reducing the cavity length, thereby shrinking the gain medium and the saturable absorber. Since the gain medium upholds lasing and the saturable absorber stabilizes and mode-locks the comb, shrinking them is not desirable and practically possible. High-repetition-rate combs can, however, rather easily be generated in small optical high-Q resonators where $f_{\mathrm{rep}} = c/2\pi R n_{\mathrm{g}}$ (R being the cavity radius and n_{g} the group velocity index of refraction) is in the few tens of GHz range for millimeter-scale radii and larger for smaller resonator sizes.

Other advantages of microresonator-based combs are the relatively small pump powers required for their generation (typically a few to a few hundred milli-Watts, in

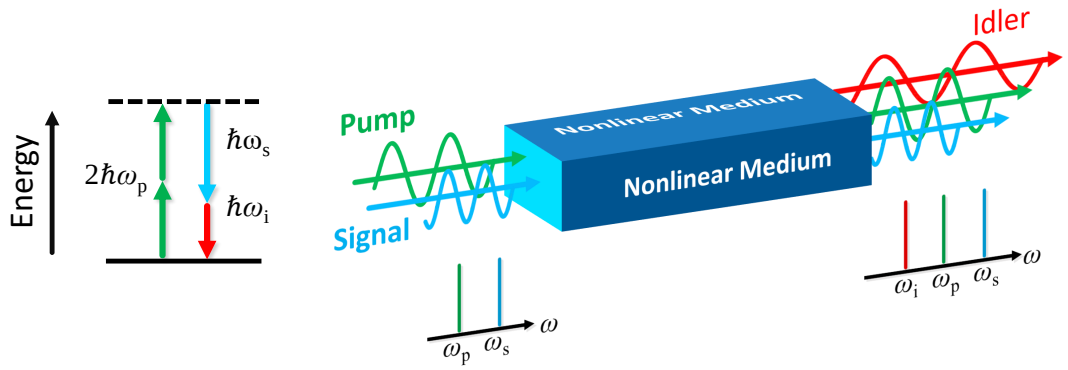

Fig. 1.7.1: Schematic showing FWM in an integrated photonic waveguide. In pump-degenerate FWM, two pump photons are converted into signal and idler photons. This nonlinear process is mediated by the $\chi^{(3)}$ nonlinearity of the waveguide material.

contrast to tens of Watts for mode-locked lasers) and the possibility of high-Q resonator mass fabrication. Power efficient comb generation in optical microresonators, together with their small footprint, places them in high demand for a variety of applications where weight and power constraints apply, e.g., accurate time-keeping in space. Ease of mass fabrication of resonators for OFC generation is desirable for applications outside well-equipped technical laboratories. For instance, silicon nitride (Si_3N_4) microresonators with multi-million optical quality factors are now commonly fabricated by CMOS-compatible fabrication techniques and used in research labs. They augur well for comb applications such as telecommunication, mobile optical clocks, and medical spectroscopy where low-cost and small-footprint devices are required.

1.8 Resonator types used in optical frequency comb generation

The advantages of microresonator-based optical frequency combs highlighted in the previous section have proven microcomb generation to be one of the most promising areas of nonlinear photonics. Optical resonators [13] are the indispensible enabling

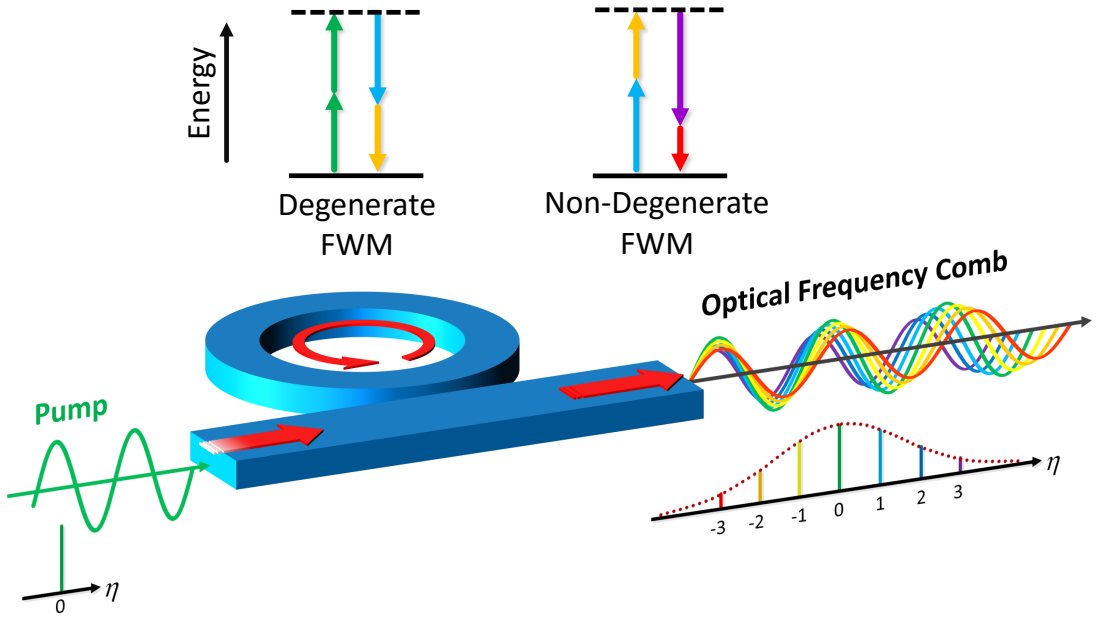

Fig. 1.7.2: Schematic showing frequency comb generation in a microring resonator driven by a CW laser. Field enhancement inside a high-Q microresonator results in nonlinear optical interactions at reduced powers; c.f. Fig. (1.7.1). A set of new frequencies are generated as a result of cascaded FWM: seeded by vacuum fluctuations, pump-degenerate FWM generates photons at two new side-band frequencies. The generated photons can mix with the pump photons and with each other to create photons at other frequencies through non-degenerate FWM. Frequency generation in this process is both energy- and momentum-conserved. η is the azimuthal microresonator mode number relative to the mode number of the pumped resonance.

elements in nonlinear photonics and particularly frequency comb generation. Despite their compactness, they confine photons in very small volumes for extended periods of time. As such, they enhance electromagnetic field intensity, increase effective light-matter interaction length, and boost conversion efficiency, thereby significantly reducing thresholds for nonlinear optical phenomena. Microresonator efficiency for nonlinear optical as well as sensing applications is usually quantified by the quality factor to mode volume ratio (Q/V_{mode}), which is a measure of *how long* and *to what spatial volume* a resonator can store electromagnetic energy. Owing to their large Q/V_{mode} ratio, optical microcavities have been used for such applicatoins as hazardous

and biomaterial sensing [23] as well as ultralow-threshold lasing[2] [24, 25].

Different resonator shapes and material platform have been used for frequency comb generation, see, for instance, [1, 26, 27] and references therein. Figure 1.8.1 shows examples of optical microresonators used frequently in nonlinear photonics, cavity optomechanics, and quantum information, which have been utilized particularly successfully in frequency combs studies: microspheres, microtoroids, wedge resonators, polished crystalline resonators, microdisks, and microrings. Light coupling and read-out to and from microshperes, toroids, wedge, and polished crystalline resonators can be done using tapered fiber or prisms while integrated waveguides are used for pump laser coupling to the microdisks and microrings. Microspheres are geometrically simple structures, which support whispering-gallery-modes (WGM's) with well-studied mode profiles [28]. Silicon dioxide (SiO_2, also known as silica) microshperes have been utilized for cavity quantum electrodynamics (QED) since 1990s because of their ultra-high, close to material-limited, optical quality factors [29]. Microtoroids are a close relatives of the spheres with the added advantage that they can be integrated on a chip. Both spheres and toroids have also been extensively utilized in cavity optomechanics. Wedge resonators rectify the lack of precise size control in toroid resonators. With radii on the order of millimeter to centimeter, wedge resonators have demonstrated very high Qs close to 10^8, and have been used to demonstrate on-chip microwave synthesizers, microcombs with microwave to millimeter wave FSR, and solitons with microwave repetition rate [30]. Polished crystalline microresonatrs have been used in many studies, including in demonstration of broadband phase-locked combs in the form of temporal solitons. Microdisk and microring resonators have the advantage of CMOS-compatible monolithic planar fabrication which makes them more suitable for integrated applications. Additionally

[2]Strictly speaking, the lasing threshold in lasers with intensity-dependent gain coefficient, such as the Raman laser, is proportional to Q^2/V_{mode}, i.e., the quality factor multiplied by the Purcell factor. Therefore, a large quality factor has a two-fold benefit of increased gain and reduced loss per round trip.

they can be covered with a layer of cladding material, different from the waveguide and resonator material (e.g., SiO_2 cladding for Si_3N_4 resonators). Although this layer can, to some extent (depending on the refractive index contrast between the core and cladding), reduce cavity Q, it can act as a protective covering and enhance robustness of the devices[3]. Phase-locked combs have been demonstrated in microring (and their close relative, racetrack) resonators, an important milsestone towards chip-based frequency combs. Waveguides can be coupled to disk and ring microresonators in either point- or pulley-coupling geometries and have been used to demonstrate integrated photonic delay lines and filters [31]. In particular, pulley coupling of the waveguide to the resonator in add-and-drop geometries has recently been used to improve the span of on-chip microcombs by the more efficient extraction of the nonlinear waves generated inside the resonator [32]. Quality factors of spheres and toroids are typically higher than those of disks and rings of comparable diameter because the fabrication process of the former (based on, e.g, heating the tip of a fiber in the fabrication of spheres and on shining CO_2 laser on a silica disk supported by a silicon post in the case of the toroid [33]) exploits surface tension, resulting in extremely small surface roughness and therefore very low loss. Polished crystalline resonators have also demonstrated some of the highest Q factors reported so far; in fact Qs of $10^9 - 10^{11}$ are commonly being used by some researchers [14]. It is worth noting that the techniques and theoretical models studied and proposed in this thesis are generic and apply to all of the resonators shown in Fig. 1.8.1.

It is necessary to emphasize the role of dispersion in microcomb generation, especially on the comb span and dynamic range of parameters such as pump power and pump-resonance detuning. Generation of octave-spanning microcombs would enable the demonstration of compact self-referenced combs and is currently being persued

[3]Unless the inherent material loss in the cladding limits the quality factor, in principle cladding can enhance the quality factor as the reduction in the refractive index contrast lowers the radiation loss and sensitivity to the sidewall roughness.

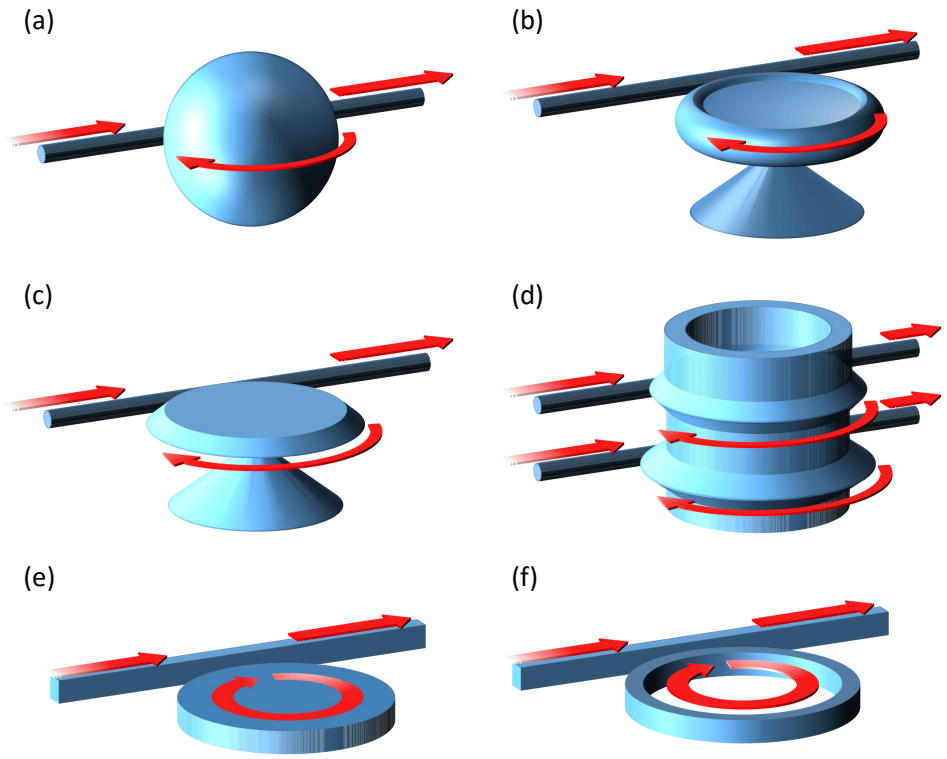

Fig. 1.8.1: Examples of optical resonators frequently utilized in nonlinear photonics, cavity optomechanics, and quantum information, which have been particularly successfully in frequency combs studies. The red arrows show typical directions of light propagation in the access waveguides (optical fibers or planar waveguides) and the resonators. (a) A microspheres. Light is coupled into the sphere through a (tapered) fiber or a prism. This figure shows excitation with a fiber. (b) A microtoroid. The toroid resides on an undercut post as a result of subsequent dry- and wet-etching. (c) A wedge resonator. These resonators rectify the lack of precise size control in toroid resonators. (d) Polished crystalline resonators. Crystals in the shape of a cylinder are polished (e.g., manually) to form the protruded rims on the surface of the cylinder, the high-Q crystalline resonators. (e) A microdisk resonator, coupled to an access waveguide. (f) A microring resonator, which is essentially a waveguide closed on itself. Just as a microdisk, input coupling is through a bus waveguide.

by multiple research groups. Consequently, dispersion engineering and measurement are of immense significance. Dispersion requirements for broadband comb generation have been studied meticulously [34, 35], and extensive work has been done on dispersion management in different resonator geometries, including polished crystal (e.g.,

the photonic belt resonator [36]), microring [37], and wedge resonators [38]. Additionally, innovative methods have been developed for the measurement of dispersion in cold and hot optical resonators [39, 40]. Dispersion will be discussed in further detail in Section 1.11.

1.9 Frequency conversion in optical microresonators

As noted earlier, starting from a continuous-wave pump laser, parametric frequency conversion [41] in a high-Q optical resonator can give rise to a wide spectrum of equidistant frequency lines known as an optical frequency comb. New frequencies are generated as a result of cascaded parametric FWM (see Fig. 1.7.2): seeded by *vacuum fluctuations*, pump-degenerate FWM generates photons at two new sideband frequencies, where parametric gain outweighs losses, at the expense of two pump photons. Because of the inherent feedback mechanism in the resonator, the generated photons can interact with the pump photons and with each other to create photons at other frequencies through degenerate and non-degenerate FWM.

Parametric frequency generation is subject to both energy and momentum conservation. In Fig. 1.7.2, $\eta \in \{0, \pm 1, \pm 2, \pm 3, \dots\}$ is the *relative* azimuthal resonator mode number, which also labels the frequency comb teeth with respect to the pumped mode. The pumped mode (the one closest in frequency to the pump laser frequency) satisfies the resonance condition $j_0 \lambda_{j_0} = 2\pi R n_{\mathrm{e}}$, where j_0 is the mode number (an integer, usually a few hundred to a few thousand, based on resonator size), λ_{j_0} is the resonance wavelength, R is the resonator radius[4], and $n_{\mathrm{e}} \equiv n_{\mathrm{e}}(\lambda_{j_0})$ is the modal effective refractive index at wavelength λ_{j_0}. Other modal frequencies satisfy a similar

[4]To be slightly more fastidious, the parameter R in this equation is an *effective* radius, measured roughly from the peak of the modal intensity profile to the cavity center [42]. As such, different mode families in a cavity cannot be phase-matched, even if energy degeneracy allows energy conservation requirement of the nonlinear mode coupling to be respected. They may, however, couple as a result of linear processes, such as light scattering by surface roughness and material impurities, which shift modal frequencies through avoided mode crossing (see [34] and the Supplementary Material thereof).

resonance condition, $j\lambda_j = 2\pi R n_{\mathrm{e}}(\lambda_j)$. The relative mode number is therefore equal to $\eta = j - j_0$, such that the pumped mode is labeled by $\eta = 0$ and the rest of the comb teeth are numbered with respect to it. If four resonator modes $\eta = l, m, n$, and μ are to interact efficiently in a nonlinear process based on Kerr nonlinearity, their mode numbers should respect the constraint $l - m + n = \mu$, see Section 2.4. Now, modes of a circular resonator are angular momentum eigenstates with discrete propagation constants proportional to the mode number,

$$k_j = k_{j_0+\eta} = \frac{2\pi n_{\mathrm{e}}(\lambda_j)}{\lambda_j} = \frac{j_0 + \eta}{R}, \tag{1.9.1}$$

such that $l - m + n = \mu$ is equivalent to

$$k_{j_0+l} - k_{j_0+m} + k_{j_0+n} = k_{j_0+\mu}. \tag{1.9.2}$$

(Note that addition of j_0 to all four integers in the former equality keeps it intact.) Equation (1.9.2) is in fact the phase matching condition or conservation of momentum [11]. Consequently, modes of a resonator can harbor light frequencies interacting through Kerr nonlinearity and the interaction will automatically be phase-matched.

Conservation of energy,

$$\hbar\omega_l - \hbar\omega_m + \hbar\omega_n = \hbar\omega_\mu \tag{1.9.3}$$

where $\hbar$ is the reduced Planck constant and

$$\omega_\eta = \frac{2\pi c}{\lambda_{j_0+\eta}} = \frac{j}{R} \cdot \frac{c}{n_{\mathrm{e}}}, \tag{1.9.4}$$

(for $\eta \in \{l, m, n, \mu\}$) is the resonance frequency in radians per second, on the other hand, places stringent requirements on the resonator material and geometric dispersion. The reason is that the effective index n_{e} is not a constant and is affected by both change of frequency and resonator shape. In other words, the modes of a resonator are not necessarily equally spaced and the resonator free spectral range is not constant because of chromatic dispersion so that the resonance frequencies ω_η will not be

equidistant. Equation (1.9.3), however, means the generated frequencies must maintain a constant spacing, i.e., $\omega_l - \omega_m = \omega_\mu - \omega_n$. Based on this simplified argument, conservation of energy should hinder FWM in a resonator. However, sufficiently close to the pump, the accumulated FSR variations are small and energy conservation will be respected as well. The influence of modal dispersion and energy conservation is then limiting the comb span: even if abundant laser power is available, comb span will be limited and power in the comb teeth will not be uniform.

1.10 Review of microresonator optics

In this section, I will briefly review the main resonator concepts required to understand microcombs. Let's consider a resonance mode given by

$$j\lambda_j = 2\pi R n_{\mathrm{e}}(\lambda_j), \tag{1.10.1}$$

where, as before (see Section 1.9), j is the mode number, λ_j is the resonance wavelength, R is the resonator radius, and n_{e} is the modal effective refractive index at wavelength λ_j. The resonance frequency of the mode is given by $\omega_j = 2\pi c/\lambda_j$. Imagine that the resonator is coupled to an access or bus waveguide (a tapered fiber or an integrated waveguide, depending on the platform and resonator type; see Fig. (1.8.1)), and that somehow there is already some power in the resonator (maybe, a pump laser coupled some light into the resonator through the access waveguide and was then turned off). The field dynamics inside the resonator can then be described by[5]

$$\frac{\mathrm{d}A_j}{\mathrm{d}t} = -\frac{\Delta\omega_j}{2}A_j. \tag{1.10.2}$$

Here, $\Delta\omega_j$ is called the resonance full-width at half-maximum (FWHM), and is a measure of resonance linewidth. The field A_j is proportional to the square root of energy stored in the resonator in the relevant mode. Different normalizations can

[5]The oscillatory term $\mathrm{i}\omega_j A_j$ on the right-hand-side of Eq. (1.10.2) has been removed here by a simple change of variable.

be used; in this thesis, I will assume the field is normalized in a way that $|A_j|^2$ is equal to the number of photons in mode j, with frequency (close to) ω_j, in the cavity. Nonetheless, as details are immaterial for the current discussion, I will simply refer to $U_j = |A_j|^2$ as build-up energy inside the resonator. (In the discussion of the power inside the resonator, the distinction will be important; see Eq. (1.10.15).) Fourier transform of Eq. (1.10.2) yields

$$\tilde{U}_j = \frac{U_j(0)}{(\Delta\omega_j/2)^2 + \omega^2} \tag{1.10.3}$$

where $U_j(0) = |A_j(0)|^2$ is the initial amount of power in mode j (power in this mode when the pump laser was turned off). The latter equation suggests that the resonance has a Lorentzian lineshape. It also justifies why $\Delta\omega_j$ is called the resonance full-width at half-maximum.

Using Eq. (1.10.2), the following equation can easily be found for the energy,

$$\frac{\mathrm{d}U_j}{\mathrm{d}t} = -\Delta\omega_j U_j. \tag{1.10.4}$$

This equation has a straightforward solution

$$U_j(t) = U_j(0)\exp(-t/\tau_j), \tag{1.10.5}$$

where $\tau_j = 1/\Delta\omega_j$ is called the resonance photon lifetime or ring-down time. The power loss is

$$P_\mathrm{L} = -\frac{\mathrm{d}U_j}{\mathrm{d}t} = \Delta\omega_j U_j. \tag{1.10.6}$$

The quality factor (Q-factor) of the resonance mode is defined by

$$Q_\mathrm{L} = \omega_j \frac{U_j}{P_\mathrm{L}}, \tag{1.10.7}$$

which is, 2π times the ratio of the power stored to the power lost in the cavity while the field traversed the cavity perimeter once. The subindex "L" stands for *loaded*; the reason for this terminology will become clear shortly. Combining Eq. (1.10.6) and

(1.10.7), another expression for the quality factor can be inferred

$$Q_{\mathrm{L}} = \frac{\omega_j}{\Delta\omega_j} = \omega_j \tau_j. \tag{1.10.8}$$

Equations (1.10.5) and (1.10.8) suggest two ways for measuring the qualify factor, by monitoring cavity energy while ring down and finding τ_j or through measuring transmission as a function of wavelength and finding the FWHM. Since the measured quality factor combines the effects of coupling to the access waveguide and intrinsic losses of the cavity (e.g., radiation loss, scattering loss, etc.), it is called the "loaded" Q.

It is beneficial to define (external) coupling quality factor and intrinsic quality factor as well, namely

$$Q_{\mathrm{c}} = Q_{\mathrm{ext}} = \frac{\omega_j}{\Delta\omega_{\mathrm{ext}}} = \omega_j \tau_{\mathrm{ext}}, \tag{1.10.9}$$

and

$$Q_{\mathrm{i}} = Q_{\mathrm{int}} = \frac{\omega_j}{\Delta\omega_{\mathrm{int}}} = \omega_j \tau_{\mathrm{int}}. \tag{1.10.10}$$

In the above definitions, $\Delta\omega_{\mathrm{ext}}$ and $\Delta\omega_{\mathrm{int}}$ are the contributions to the resonance linewidth due to external coupling and intrinsic cavity losses, respectively: $\Delta\omega_j = \Delta\omega_{\mathrm{ext}} + \Delta\omega_{\mathrm{int}}$. One can easily verify the following relationship between the different Q's:

$$\frac{1}{Q_{\mathrm{L}}} = \frac{1}{Q_{\mathrm{ext}}} + \frac{1}{Q_{\mathrm{int}}}. \tag{1.10.11}$$

If $Q_{\mathrm{ext}} = Q_{\mathrm{int}}$, the resonator is said to be critically coupled to the access waveguide, while it is called under-coupled if $Q_{\mathrm{ext}} > Q_{\mathrm{int}}$ and over-coupled when $Q_{\mathrm{ext}} < Q_{\mathrm{int}}$. Frequency comb generation is commonly done in the over-coupled regime for the coupling of the pump laser to the pumped resonance.

If the resonator is being driven by a laser at frequency ω_{P}, instead of Eq. (1.10.2), the following will hold

$$\frac{\mathrm{d}A_j}{\mathrm{d}t} = -\frac{\Delta\omega_j}{2} A_j + \sqrt{\Delta\omega_{\mathrm{ext}}} s_{\mathrm{in}} \exp[\mathrm{i}(\omega_{\mathrm{P}} - \omega_j)t], \tag{1.10.12}$$

where $\Delta\omega_{\text{ext}}$ is the contribution to the resonance linewidth due to external coupling to the access waveguide and s_{in} is the external drive, normalized such that $\hbar\omega_{\text{P}}|s_{\text{in}}|^2$ gives the power in the access waveguide P_{in}. The exponent on the right-hand-side of the latter equation can readily be removed and replaced by a detuning term

$$\frac{\mathrm{d}A_j}{\mathrm{d}t} = -\frac{\Delta\omega_j}{2}A_j - \mathrm{i}(\omega_{\text{P}} - \omega_j)A_j + \sqrt{\Delta\omega_{\text{ext}}}s_{\text{in}}. \tag{1.10.13}$$

In steady-state ($\mathrm{d}/\mathrm{d}t = 0$) and for single frequency driving conditions, Eq. (1.10.13) yields

$$A_j = \frac{\sqrt{\Delta\omega_{\text{ext}}}}{\Delta\omega_j/2 + \mathrm{i}(\omega_{\text{P}} - \omega_j)}s_{\text{in}}. \tag{1.10.14}$$

Recalling that the actual energy inside the resonator mode of interest is $\hbar\omega_{\text{P}}|A_j|^2$, the above equation can be written as

$$P_j = \frac{\omega_{\text{P}}}{T}|A_j|^2 = \frac{2}{\pi}\frac{\Delta\omega_{\text{ext}}}{\Delta\omega_j}\mathcal{F}\frac{1}{1 + \left[\frac{2(\omega_{\text{P}} - \omega_j)}{\Delta\omega_j}\right]^2}P_{\text{in}}, \tag{1.10.15}$$

where

$$\mathcal{F} = \frac{\omega_{\text{FSR}}}{\Delta\omega_j} = \frac{2\pi f_{\text{rep}}}{\Delta\omega_j}. \tag{1.10.16}$$

is the cavity finesse.

1.11 Microresonator dispersion

Dispersion, as mentioned earlier, plays a major role in optical frequency comb generation as it highly affects the required pump power for comb generation, the span of the generated comb, the shape of the power spectrum envelope, and even the repetition rate of the generated pulse in the resonator (if the comb is phase-locked and pulsation is observed). Dispersion engineering, therefore, is a key practice for the generation of frequency combs with specific applications in mind. For example, if a comb is to be locked to two atomic transitions of a material (e.g., the rubidium gas) to fix its two degrees of freedom (f_{CE} and f_{rep}) and be used for frequency metrology

or timekeeping, it should cover these two specific transition frequencies. As a result, the dispersion of the resonator used for this application should be engineered such that a *stable* comb can be generated in a specific range and with a specific span.

Figure 1.7.1 is a schematic illustrating pump-degenerate FWM in an integrated photonic waveguide. Integrated nonlineear photonic devices, like the one depicted in this figure, offer flexible features crucial to effective nonlinear interactions such as dispersion and material engineering, and effective nonlinear area reduction. Dispersion or nonlinearity coefficient management is possible, for instance, through engineering the waveguide geometry [43], covering waveguides or resonators by a blanket layer of a suitable different material [44], or by doping or altering the stoichiometric ratios in compound nonlinear materials (e.g., increasing the ratio of silicon (Si) in silicon nitride (Si_3N_4) to get Si-rich SiN_x) [45]. Dispersion engineering can be done in other resonator types as well, e.g., in wedge resonators by changing the wedge angels or adding extra edges [46] and in polished crystalline resonators by careful control of chamfer angles.

Dispersion engineering amounts to engineering dispersion coefficients in a Taylor series expansion of the propagation constant vs. frequency in a waveguide-based resonator (e.g., a ring or racetrack) and of the resonator modal frequencies vs. mode number. In this section, I present the mathematical framework used for describing dispersion in both types of platforms (waveguide-based and WGM resonators) and present the relationship between the two descriptions.

For a waveguide, it is customary to define dispersion in terms of the coefficients in a Taylor series expansion of the propagation coefficient (also sometimes referred to as the *wavenumber*) $\beta(\omega)$ in the frequency ω around the pump or carrier frequency ω_0. The expansion is usually written as

$$\beta(\omega) = \beta_0 + \beta_1(\omega - \omega_0) + \frac{1}{2!}\beta_2(\omega - \omega_0)^2 + \frac{1}{3!}\beta_3(\omega - \omega_0)^3 + \dots . \tag{1.11.1}$$

The wavenumber β has dimensions of $[L]^{-1}$ (SI units of m^{-1}). The coefficients in

Eq. (1.11.1) are defined through

$$\beta_k = \frac{\mathrm{d}^k \beta}{\mathrm{d}\omega^k}, \tag{1.11.2}$$

where all of the derivative are evaluated at ω_0.

A ring (or more generally racetrack) resonator is formed when a waveguide is bent onto itself and its two ends are connected to each other. This recipe will lead to periodic boundary conditions and as a result the continuum of waveguide modes will change into a set of discrete resonator modal frequencies. The angular frequency ω will then have to bear a label ω_j found from the resonance condition $j\lambda_j = 2\pi R \times n(\omega_j)$, with $\lambda_j = 2\pi c/\omega_j$, c the vacuum speed of light, R the ring radius, and $n(\omega_j)$ the modal effective refractive index at the frequency of the mode of interest. If the radius of curvature of the bends in this resonator are not very small (i.e., are a few tens of microns), the dispersion parameters of the waveguide could be used for the resonator as well.

The modal dispersion in a resonator could also be identified by looking at the frequency dependence of the modal frequencies, rather than that of the propagation coefficient (as is the case for waveguides). This approach is in fact more suited especially when a resonator supporting whispering-gallery modes is considered, and is indeed practically relevant because it is common to experimentally measure the spectral position of different modes involved in comb generation [47]. When these modal frequencies are known, they can be fit to a polynomial in the modal number j around a pumped mode number j_0,

$$\omega_j = \omega_{j_0} + D_1(j - j_0) + \frac{1}{2!} D_2 (j - j_0)^2 + \frac{1}{3!} D_3 (j - j_0)^3 + \cdots . \tag{1.11.3}$$

The coefficients D_k are defined in a similar way to the β_k's, with the caveat that their definition is based on differences rather than continuous variable derivatives. In practice, they can be found by polynomial curve fitting.

It is straightforward, in principle, to find the D_k coefficients with a knowledge

of the β_k's, or vice versa. To find their relationship, one notes that the resonance condition for a mode of frequency ω_j can be written as

$$\frac{j}{R} = \frac{2\pi}{\lambda_j} n(\omega_j) = \frac{\omega_j}{c} n(\omega_j) = \beta(\omega_j). \tag{1.11.4}$$

Hence,

$$\frac{j - j_0}{R} = \beta(\omega_j) - \beta(\omega_{j_0}). \tag{1.11.5}$$

Using Eq. (1.11.1) for $\omega = \omega_j$ at $\omega_0 = \omega_{j_0}$, and using the result in the equation above leads to

$$\frac{j - j_0}{R} = \beta_1(\omega_j - \omega_{j_0}) + \frac{1}{2!}\beta_2(\omega_j - \omega_{j_0})^2 + \frac{1}{3!}\beta_3(\omega_j - \omega_{j_0})^3 + \dots . \tag{1.11.6}$$

This expression gives us $j - j_0$ in terms of $\omega_j - \omega_{j_0}$. It is then possible to replace the different powers of $j - j_0$ in Eq. (1.11.3) with the above summation in terms of $\omega_j - \omega_{j_0}$.

$$\begin{aligned}
\omega_j - \omega_{j_0} &= D_1(j - j_0) + \frac{1}{2!}D_2(j - j_0)^2 + \frac{1}{3!}D_3(j - j_0)^3 + \dots \\
&= D_1\left[R\beta_1(\omega_j - \omega_{j_0}) + \frac{R}{2!}\beta_2(\omega_j - \omega_{j_0})^2 + \frac{R}{3!}\beta_3(\omega_j - \omega_{j_0})^3 + \dots\right] \\
&+ \frac{1}{2!}D_2\left[R\beta_1(\omega_j - \omega_{j_0}) + \frac{R}{2!}\beta_2(\omega_j - \omega_{j_0})^2 + \frac{R}{3!}\beta_3(\omega_j - \omega_{j_0})^3 + \dots\right]^2 \\
&+ \frac{1}{3!}D_3\left[R\beta_1(\omega_j - \omega_{j_0}) + \frac{R}{2!}\beta_2(\omega_j - \omega_{j_0})^2 + \frac{R}{3!}\beta_3(\omega_j - \omega_{j_0})^3 + \dots\right]^3 \\
&+ \dots .
\end{aligned} \tag{1.11.7}$$

Comparing the coefficients of different powers of $(\omega_j - \omega_{j_0})$ on both sides of Eq. (1.11.7) leads to expressions with link D_k's to β_k's. For instance,

$$1 = D_1 R\beta_1 \rightarrow D_1 = \frac{1}{R\beta_1} \tag{1.11.8}$$

$$0 = \frac{1}{2}D_1 R\beta_2 + \frac{1}{2}D_2 R^2\beta_1^2 \rightarrow D_2 = \frac{-\beta_2}{\beta_1^3 R^2}. \tag{1.11.9}$$

This algorithm can, in principle, give the relationship between any D_k coefficient with the β_k's, although collecting all powers of $(\omega_j - \omega_{j_0})$ on the right-hand-side of

Eq. (1.11.7) rapidly becomes algebraically elaborate as the index k increases. For $k = 3, 4$ one finds

$$D_3 = \frac{-\beta_3}{R^3\beta_1^4} + 3\frac{\beta_2^2}{R^3\beta_1^5}, \tag{1.11.10}$$

$$D_4 = \frac{-\beta_4}{R^4\beta_1^5} - 33\frac{\beta_2^3}{R^4\beta_1^7} + 16\frac{\beta_2\beta_3}{R^4\beta_1^6}. \tag{1.11.11}$$

It is noted that although I have derived equations for D_k's strictly in terms of β_k's only (and not D_ks with smaller index value), in a numerical routine, the D_k's can be found recursively (i.e., first D_1, then D_2, then D_3, etc.) and not all at once. Hence, polishing the algebraic equations as was done above is not necessary. Obviously, same holds for finding β_k's given D_k's.

1.12 Outline of the thesis

This thesis is organized in 5 chapters.

Chapter 1, the current chapter, covered the fundamentals of microresonators and optical frequency combs. In the final section, the two mathematical approaches commonly used for the description of dispersion in waveguide-based and whispering-gallery-mode resonators were discussed in detail and their relationship was clarified.

Chapter 2 discusses mode locking in hyperparametric oscillators in the presence of modulational instability and explains how sidebands seeded by random vacuum fluctuations grow into phase-locked comb teeth. The predictions by the simple analytical expressions found in this chapter are confirmed through numerical integration of the Lugiato-Lefever equation (externally driven damped nonlinear Schödinger equation).

Chapter 3 extends the analysis of its preceding chapter and introduced a novel phase locking model for micrcomb generations. This model is applicable to both hyperparametric oscillations seeded by modulational instability (Turing patterns) and dispersive Kerr solitons. The introduced model is argued to apply to pulse generation based on mode-locked lasers as well. This chapter also provides a stability analysis

for the introduced reduced model. This chapter concludes with a simple and intuitive explanation of the phase steps recently measured in optical microresonators [40].

Chapter 4 introduces a novel technique for deterministic single soliton generation and pulse manipulation in microresonator-based optical frequency combs. This model helps pave the path towards turn-key chip-scale pulsed lasers. The analysis presented in this chapter clarified some experiments in fiber cavities which preceded this work. This suggested technique has recently been successfully implemented in crystalline MgF_2 resonators [48].

Chapter 5 presents a detailed study of higher-order dispersion in microcombs. It is shown that higher-order dispersion can lead to dispersive wave emission as well as change of the repetition rate in microresonator-based phase-locked combs (pulses). One important limitation of the split-step Fourier transform method, which is widely utilized for theoretical studies of microcombs (as well as pulse propagation in fibers), is highlighted and explained. Finally, wideband near-infra-red optical frequency combs in realistic crystalline calcium fluoride resonators for use in optical atomic clocks (stabilize through two lasers locked to rubidium D_1 and D_2 transitions) are presented.

CHAPTER 2

ANATOMY OF PHASE LOCKING IN KERR-NONLINEAR HYPERPARAMETRIC OSCILLATIONS

"To see the world for a moment as something rich and strange is the private reward of many a discovery."

Edward M. Purcell, Nobel Lecture (1952)

One of the important regimes of frequency comb generation in optical microresonators is that of hyperparametric oscillations. In this regime, a continuous-wave input pump laser is turned into a frequency comb at the resonator output port. The emergence of this frequency comb is seeded by random vacuum fluctuations which grow as a result of parametric gain in a process of great significance in nonlinear systems, called "modulational instability". Although ignited by random noise, hyperparametric oscillations are phase locked and correspond to a pulse train, sometime also called Turing patterns or Turing rolls [49]. Additioanlly, they are very robust against pump frequency and amplitude noise and, therefore, ideally suited for applications such as RF microwave generation and long-haul optical telecommunication [14, 50, 51]. In this chapter, an investigation of the dynamical origin of spontaneous synchronization and phase locking of hyperparametric oscillations in Kerr-nonlinear media is presented. In other words, I set out to figure out how oscillations which arise from vacuum noise end up oscillating in harmony. Using few-mode approximations of the governing equation of frequency comb generation (an externally driven, damped nonlinear Schödinger equation, commonly referred to as the Lugiato-Lefever equation), it is shown that the pumped mode

of the comb injection-locks to the driving laser pump following the Adler equation. Additionally, based on experimentally-motivated assumptions, analytical expressions which reveal the essence of phase locking in hyper-parametric oscillations in frequency combs are derived. The predictions based on this theoretical analysis are confirmed numerically. The study presented here sheds light on the process of phase locking and provides guidelines for an optical choice of pump powers and relative phases if the resonator is to be pumped by more than one laser with the goal of improving stability. The results are mathematically generic and apply also to other systems described by an externally driven, damped nonlinear Schödinger equation[1].

2.1 Introduction

Phase-locked wideband optical frequency combs have in recent years been demonstrated in Kerr-nonliear media in multiple platforms [1, 30, 37, 53–55]. These combs have shown to be ideally suited for ultra-high–capacity optical communication [50, 51] and pure radio frequency (RF) wave generation [14]. The superior performance of micro-resonator-based combs for such applications hinges on the stable spacing between the comb teeth and their synchronized oscillations, which leads to the low phase noise of the generated comb teeth. Phase locking of the frequency comb, i.e. the establishment of a temporally enduring relationship between the phases of the discrete frequencies comprising the comb, is key to the emergence of such stable comb lines.

Despite significant theoretical and experimental studies and demonstrations on microcombs, the phenomenon of phase locking in these nonlinear systems is not yet well understood. The generation of frequency combs in Kerr nonlienar media is

[1]This chapter is based on results presented in [52].

described by a damped, externally driven nonlinear Schrödinger equation [56, 57], also referred to as the Lugiato-Lefever equation (LLE) [58–61]. While it is known that this equation has sharply peaked solutions in the form of hyper-parametric oscillations (or Turing patterns) and solitons [54, 56, 57, 59, 60, 62, 63]—which evidence phase-locked states—the evolutions of the comb teeth phases toward these solutions has scarcely been studied. Clear understanding of the phenomenon of phase locking in optical microresonators can lead to devising novel techniques for achieving phase-locked states or improving the coherence properties of frequency combs. It is also necessary for understanding and justifying some recent phase measurements of steady-state optical frequency combs [40, 64].

Coillet and Chembo [65] provided an explanation of phase locking of optical microcombs in terms of the cascaded emergence of phase-locked triplets, while Loh *et al.* explained the phase offset of pumped mode phase with respect to the rest of the comb in Turing patterns. Wen *et al.* [66] suggested a link between phase locking in parametric frequency combs and the famous Kuramoto model for the synchronization of globally-coupled nonlinear oscillators. The analysis in [66] noted that anti-symmetrization of the comb phase profile occurs prior to phase locking and soliton formation, and justifies the phase offset between the pumped mode and the rest of the comb lines in solitons.

In this section, I present a study of phase locking in parametric frequency combs based on 3- and 5-mode truncations of the master equation describing comb generation in microresonators (the LLE). The relative tractability of the truncated model allows one to find analytical expressions for the temporal evolution of the comb teeth phases, which clearly show how the frequency sidebands seeded by the random phase of vacuum fluctuations end up lying on a straight line. I show that the pumped mode of the comb injection-locks to the driving pump laser through the Adler equation and find that the anti-symmetrization of the sideband phases with respect to the pumped

mode phase is predicted by the simplified 3-mode description. Considering the 5-mode truncation of the LLE, it is possible to find an analytical expression describing how the phases of the comb teeth evolve, on a longer time scale, to their final locked state. It is noteworthy that the externally-driven, damped nonlinear Schrödinger equation has been used for describing a variety of physical phenomena in different nonlinear systems (see, e.g., [67] and references therein). Hence, the results presented in this chapter apply to other NLSE systems as well.

2.2 Description of frequency comb generation by coupled nonlinear equations and the Lugiato-Lefever equation

2.2.1 Some history

Four-wave mixing can in fibers can be described using coupled nonlinear ordinary differential equations [68]. This description is based on modal expansion. A similar approach can be used for frequency comb generation in high-Q optical resonators. Chembo and Yu adopted this approach in 2010 [69]. This work ignited great interest within the optical frequency comb community; it allowed numerical simulation of the frequency comb generation process with significant flexibility and rapid progress on the theoretical front ensued. It took a year or two till the news reached the ears of the nonlinear spatial cavity and fiber-based resonator community. They had been using a mean-field approximation of an Ikeda map since early 1990s and had described a wealth of phenomena using it [59]. In 2013, Chembo and Menyuk showed that the coupled equations found earlier through the modal expansion approach can be converted into a single partial differential equation in the form of a damped and driven nonlinear Schrödinger equation (NLSE) [61]. In the same year, Coen *et al.* showed that the mean field description can be used for optical microresonators as well [60].

Within the frequency comb community, therefore, this damped, driven NLSE is usually referred to as the Lugiato-Lefever equation (LLE), after Lugiato and Lefever who first introduced it in 1987 in the context of spatial dissipative resonators [58]. The same equation has been used by nonlinear dynamicists from around the same time, and called the externally (or ac-) driven damped NLSE; see [67] and references therein. Interestingly, Matsko *et al.* had used this NLSE before the introduction of the modal expansion approach in 2009, and had predicted the existence of mode-locked combs (i.e., pulses) in microresonator-based combs. It is an old story in science.

2.2.2 Overview of derivation

The goal of this section is not to rederive the LLE. My goal here is to justify the form of this equation physically and review the derivation steps briefly. For a detailed derivation, the reader can refer to the available literature [59, 61, 69]. This understanding will enable the reader to derive variants of the LLE if necessary; see Chapter 4. I will start by the coupled-mode equations and then find the LLE based on them.

The nonlinear coupled mode equation describing frequency comb generation can be found starting from a modification of Eq. (1.10.12) for the temporal evolution of the A_j's, where $|A_j|^2$ is the number of photons in the mode labeled j.

$$\begin{aligned}\frac{\mathrm{d}A_j}{\mathrm{d}t} = &-\frac{\Delta\omega_j}{2}A_j \\ &+ \text{Terms due to Kerr nonlinearity} \\ &+ \text{Drive term (only for the pumped mode).}\end{aligned} \tag{2.2.1}$$

The nonlinear terms arising from the Kerr nonlinearity are, as one could expect from a nonlinear interaction based on $\chi^{(3)}$, triple products of the comb teeth complex amplitudes (beam intensities of the different frequencies involved) and are proportional to the third-order nonlinear susceptibility $\chi^{(3)}$. These nonlinear terms appear in the

form on an intensity-dependent refractive index and any change of the refractive index causes an added phase. Hence, the nonlinear contribution in the above equation should be accompanied by the imaginary unit i. As in Section 1.11, I will label the mode number of the resonance closest to the pump frequency ω_{P} with j_0. Then, the general equation describing the complex amplitude (magnitude and phase) of the comb tooth closest to resonance with mode number j will read

$$\begin{aligned}\frac{\mathrm{d}A_j}{\mathrm{d}t} = &-\frac{\Delta\omega_j}{2}A_j \\ &- \mathrm{i}g_0 \sum_{l,m,n} A_l A_m^* A_n \exp[\mathrm{i}(\omega_l - \omega_m + \omega_n - \omega_j)t]\delta_{j_{lmn}j} \\ &+ \frac{\Delta\omega_{j_0}}{2}\mathcal{F}_0 \exp[\mathrm{i}(\omega_{\mathrm{P}} - \omega_{j_0})t]\delta_{j_0 j}. \end{aligned} \tag{2.2.2}$$

where $j_{lmn} = l - m + n$ and j's are integers. The parameter g_0 is the four-wave mixing gain and is given by

$$g_0 = \frac{n_2 c}{n_0^2}\frac{\hbar\omega_{j_0}^2}{V_{j_0}}. \tag{2.2.3}$$

In this expression, n_2 is the nonlinear (or second-order) index of refraction (see Chapter 4 in [22]), given by

$$n_2 = \frac{3}{4n_0^2\epsilon_0 c}\chi^{(3)}, \tag{2.2.4}$$

ϵ_0 being the permittivity of free space, c is the vacuum speed of light, n_0 is the (usual weak-field) index of refraction, $\hbar$ is the reduced Planck constant, ω_{j_0} is the resonance frequency of the pumped mode, and V_{j_0} is the effective nonlinear mode volume for the pumped mode. The latter parameter naturally arises in the derivation [69] and for a resonator of volume V_{cavity} is given by

$$V_{j_0} = \frac{\left[\int_\infty \mathrm{d}V|\vec{E}(\vec{r})|^2\right]^2}{\int_{V_{\mathrm{cavity}}} \mathrm{d}V|\vec{E}(\vec{r})|^4}. \tag{2.2.5}$$

Here, $\vec{E}(\vec{r})$ describes the spatial distribution of the electromagnetic modal field. For a resonator with periphery L and cross-section A_{cavity}, this expression can be simplified if one first evaluates surface integrals in the plane perpendicular to the direction of

wave propagation in the resonator and considers that it does not change for a mode over resonator perimeter, namely,

$$V_{j_0} = LA_{j_0} = L\frac{\left[\int_\infty \mathrm{d}A|\vec{E}_\mathrm{t}(\vec{r})|^2\right]^2}{\int_{A_\mathrm{cavity}} \mathrm{d}A|\vec{E}_\mathrm{t}(\vec{r})|^4}. \tag{2.2.6}$$

where A_{j_0} is the effective nonlinear modal area and $\vec{E}_\mathrm{t}(\vec{r})$ is the transverse part of the electromagnetic modal field. For a resonator of circular periphery with radius R, $L = 2\pi R$.

Resonator modes are identified by expanding modal frequencies around resonance labeled j_0 with frequency ω_{j_0} (see Section 1.11),

$$\omega_j = \omega_{j_0} + D_1(j - j_0) + \frac{1}{2!}D_2(j - j_0)^2 + \frac{1}{3!}D_3(j - j_0)^3 + \cdots . \tag{2.2.7}$$

The spatiotemporal intra-cavity waveform can be found from summing up the contributions of all the comb teeth

$$A(\theta, t) = \sum_j A_j(t) \exp[\mathrm{i}(\omega_j - \omega_{j_0})t - \mathrm{i}(j - j_0)\theta]. \tag{2.2.8}$$

Using the temporal derivative of the above expression,

$$\frac{\mathrm{d}A}{\mathrm{d}t} = \sum_j \left[\frac{\mathrm{d}A_j}{\mathrm{d}t} + \mathrm{i}(\omega_j - \omega_{j_0})A_j(t)\right] \exp[\mathrm{i}(\omega_j - \omega_{j_0})t - \mathrm{i}(j - j_0)\theta], \tag{2.2.9}$$

and its spatial n-th order derivative,

$$\mathrm{i}^n\frac{\partial^n A}{\partial\theta^n} = \sum_j (j - j_0)^n A_j(t) \exp[\mathrm{i}(\omega_j - \omega_{j_0})t - \mathrm{i}(j - j_0)\theta], \tag{2.2.10}$$

together with Eqs. (2.2.2), (2.2.7), and (2.2.8), the spatiotemporal equation describing frequency comb generation can be found,

$$\begin{aligned}\frac{\partial A}{\partial t} = &\left(-\frac{\Delta\omega_{j_0}}{2} - \mathrm{i}g_0|A|^2 + \sum_{n=1}^{N\geq 2} \mathrm{i}^{n+1}\frac{D_n}{n!}\frac{\partial^n}{\partial\theta^n}\right) A \\ &+ \frac{\Delta\omega_{j_0}}{2}\mathcal{F}_0 \exp\left[\mathrm{i}\left(\sigma_0 t\right)\right].\end{aligned} \tag{2.2.11}$$

Here, N is an integer describing the number of coefficients in Eq. (2.2.7) necessary to properly describe the particular resonator dispersion and $\sigma_0 = \omega_{\mathrm{P}} - \omega_{j_0}$ is the detuning of the pump from its nearest cavity resonance. In deriving the above equation, dispersion of resonator linewidth has been ignored, i.e.,

$$\forall j,\ \Delta\omega_j = \Delta\omega_{j_0}. \tag{2.2.12}$$

Equation (2.2.11) can be written in a rotating reference frame with angular velocity equal to D_1. This change of reference frame will remove the first-order spatial derivative of the intra-cavity field on the right-hand-side of Eq. (2.2.11), and is possible through the following change of variable

$$\theta - D_1 t = \theta'. \tag{2.2.13}$$

Considering also $t = t'$, it is easy to show that

$$\frac{\partial}{\partial\theta} = \frac{\partial}{\partial\theta'} \tag{2.2.14}$$

$$\frac{\partial}{\partial t} = -D_1\frac{\partial}{\partial\theta'} + \frac{\partial}{\partial t'}. \tag{2.2.15}$$

Eq.(2.2.11) can then be written in a simplified form,

$$\frac{\partial A}{\partial t} = \left(-\frac{\Delta\omega_{j_0}}{2} - \mathrm{i}\sigma_0 - \mathrm{i}g_0|A|^2 + \sum_{n=2}^{N\geq 2}\mathrm{i}^{n+1}\frac{D_n}{n!}\frac{\partial^n}{\partial\theta^n}\right)A + \frac{\Delta\omega_{j_0}}{2}\mathcal{F}_0. \tag{2.2.16}$$

In the latter equation, to simplify notation, the primes have been removed in the resulting equation; (θ, t) were replaced by (θ', t'). Note that the $D_1\partial A/\partial\theta$ term has disappeared as the summation now starts from $n = 2$. This simplification bears significance from a numerical integration perspective as it removes rapidly oscillating term. In Eq. (2.2.16), the detuning has been moved from the exponent of the driving force to the coefficient of the field envelope through $A \to A\exp(-\mathrm{i}\sigma t)$.

2.2.3 Normalization

Equation (2.2.16) is a nonlinear partial differential equation for the intracavity field envelope $A(\theta, t)$, in the azimuthal angle around the resonator circumference θ and time t [61]. For any theoretical analysis, it is beneficial to cast this equation in normalized form. Besides simplifying numerical integration, normalization will allow theoretical and numerical results to be generic and applicable to different material platforms and resonator shapes. The non-dimensional form of this equation reads

$$\frac{\partial \psi}{\partial \tau} = \left(-1 - \mathrm{i}\alpha + \mathrm{i}|\psi|^2 - \sum_{n=2}^{N\geq 2} (-\mathrm{i})^{n+1} \frac{d_n}{n!} \frac{\partial^n}{\partial \theta^n} \right) \psi + F, \tag{2.2.17}$$

which is the standard Lugiatio-Lefever equation (LLE). In this equation, the following normalizations have been used:

$$\frac{\Delta\omega_{j_0}}{2} t = \tau, \tag{2.2.18}$$

$$\frac{-\sigma_0}{\Delta\omega_{j_0}/2} = \alpha, \tag{2.2.19}$$

$$\frac{-D_n}{\Delta\omega_{j_0}/2} = d_n, \tag{2.2.20}$$

$$\frac{A^*}{\sqrt{\frac{\Delta\omega_{j_0}}{2g_0}}} = \psi, \tag{2.2.21}$$

$$\frac{\mathcal{F}_0^*}{\sqrt{\frac{\Delta\omega_{j_0}}{2g_0}}} = F. \tag{2.2.22}$$

In physical terms, time has been normalized to twice the photon lifetime, pump-resonance detuning has been normalized to resonance HWHM, n-th order dispersion coefficient has been normalized to resonance HWHM, and intra-cavity field envelope and drive term have been normalized to sideband generation threshold; see Section 1.10.

The derivation overview presented here yields a PDE in the azimuthal angle around the resonator and time, with periodic boundary conditions for the spatial coordinate (angle) [61, 69]. It is possible to start from an Ikeda map and find a

mean-field equation (a PDE) in a slow and a fast time variable [59, 60]. The equations resulting from both approaches are equivalent and can easily be converted to each other.

2.3 Homogeneous Solutions of the Lugiato-Lefever Equation and their Modulational Instability

Depending on the pump power $F = F_{\mathrm{P}} \exp(\mathrm{i}\phi_{\mathrm{P}})$ and detuning α values, the LLE, Eq. (2.2.17) may admit chaotic solutions [70], or solutions in the form of pulse trains called Turing rolls as well as dissipative cavity solitons [54, 56, 57, 59, 60, 62, 63]. Turing rolls evolve from the CW flat solutions of the LLE through modulational instability (MI) [71, 72], whereas solitons can be generated through changing the pump power and frequency or through parametric seeding [73, 74]. Creation of sharply peaked pulses in this equation (rolls and solitons) relies on the establishment of a balance between nonlinearity, dispersion, gain, and loss [75]. The aim in the remainder of this chapter is to understand how frequency sidebands generated from random vacuum fluctuations through the modulational instability of the spatially homogeneous solutions of the LLE phase lock to create sharply peaked pulses. Therefore, below I will briefly review bistability and MI gain for the LLE.

The simplest steady-state solutions of the LLE ($\partial/\partial\tau = 0$) is the spatially homogeneous or flat solution for which $\partial/\partial\theta = 0$ [54, 56, 69, 76, 77]. This CW equilibrium value ψ_{e}, can be found from the cubic algebraic equation

$$\rho_{\mathrm{e}}[1 + (\alpha - \rho_{\mathrm{e}})^2] = F_{\mathrm{P}}^2, \tag{2.3.1}$$

where $\rho_{\mathrm{e}} = |\psi_{\mathrm{e}}|^2$. The relation ρ_{e} vs. F_{P} is always non-negative; it is a function (single-valued) for $\alpha < \sqrt{3}$, but takes an S-shape and will have three possible values for specific values of F_{P} when $\alpha > \sqrt{3}$. MI occurs in both of these regimes for ρ_{e} larger than the threshold $\rho_{\mathrm{Th}} = 1$ (see Fig. 2.3.1). It can be shown [56, 77] that MI

gain at the early evolution of the comb can be found from

$$\lambda = -1 + \sqrt{\rho_{\mathrm{e}}^2 - (\alpha - d_2\eta^2/2 - 2\rho_{\mathrm{e}})^2}, \tag{2.3.2}$$

and will be positive if

$$\rho_{\mathrm{e}}^2 - (\alpha - d_2\eta^2/2 - 2\rho_{\mathrm{e}})^2 \geq 1. \tag{2.3.3}$$

For the case of $\alpha > \sqrt{3}$ the middle negative-slope branch of the ρ_{e} vs. F_{P} curve is unconditionally unstable while the upper and lower branches demonstrate homogeneous bistability. MI (instability with respect to perturbations with non-zero relative mode numbers) gives rise to Turing rolls on the upper branch as well as a small region on the lower branch for $\rho_{\mathrm{e}} > 1$ and $\sqrt{3} < \alpha < 2$. Examples are shown in Fig. 2.3.1(b) and (c). Panels (d)-(f) in Fig. 2.3.1 show the MI gain profile for the points marked by the white dots on the $\psi_{\mathrm{e}} - F_{\mathrm{P}}$ plane in the upper panels (a)-(c), respectively. The Turing patterns corresponding to these MI gain profile (i.e., detuning and pump power choices) are shown in Fig. 2.3.2.

It is worth noting that the Turing pattern in Fig. 2.3.2(a) is a so-called supercritical Turing pattern ($\alpha < 41/30$) while those in Fig. 2.3.2(b) and (c) are subcritical ($\alpha > 41/30$) [78]. While there are differences in existence threshold and shape between these LLE steady-state solutions [77], they are the same from the perspective of phase locking which is of interest to this work. We note that the spacing between the strongest sidebands of the pumped comb mode (upper row in Figs. 2.3.2(d)-(f)), or the peak of the MI gain profile (Figs. 2.3.1(d)-(f)) determines the number of peaks in the Turing patterns. The MI gain peak for Fig. 2.3.1(f) is on the 20th mode number, while the corresponding comb of Fig. 2.3.2(f) has 14 peaks. The reason is that the gain profiles in Fig. 2.3.1 shows the MI gain early on when the sidebands start to grow. If the gain profile is broad and falls on multiple mode numbers, apart from the mode number at the position of the MI gain maximum, nearby sidebands start occupying cavity modes as well, as is the case with Figs. 2.3.1(e) and (f). If

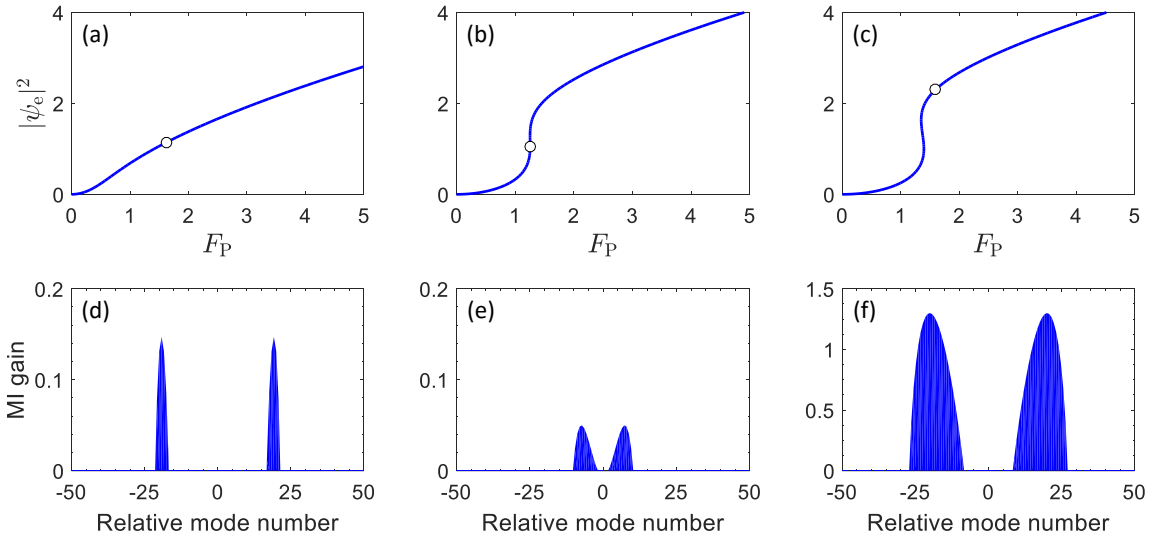

Fig. 2.3.1: (a)-(c) CW equilibrium $\rho_e = |\psi_e|^2$ solutions of the LLE vs. pump magnitude F_P, and (d)-(f) modulational instability gain profile for different values of the detuning α. Each gain profiles in (d)-(f) corresponds to the point marked by the white dots on the $|\psi_e|^2$ vs. F_P curve above it. Parameter values are (a) $\alpha = 0$, (b) $\alpha = 1.7607 = \sqrt{3.1}$, (c) $\alpha = 2.1$,(d) $(\rho_e, F_P) = (1.1472, 1.63)$, (e) $(\rho_e, F_P) = (1.05, 1.2571)$, (f) $(\rho_e, F_P) = (2.3, 1.595)$. In all cases, $d_2 = -0.0124$. Note the difference between the y-axis scale in (f) and that in (d) and (e).

the generated sharp peaks are too closely packed together in the resonator, some of them may merge and the rest will readjust their positions on an equally-spaced grid. While this was true for the Turing roll in the latter figure, the cascaded emergence of phase-locked comb teeth as a result of MI was the same as that of the simpler supercritical comb of Fig. 2.3.1(d) and 2.3.2(d). The integration of the LLE has been performed using the split-step Fourier transform method with seeding to account for noise (random vacuum fluctuations).

2.4 Description of Optical Frequency Combs in the Frequency Domain

Our goal is to explain how the sidebands which are seeded by noise (and hence have random phases) develop a simple phase relationship and give rise to sharply peaked pulses. Our approach is based on coupled nonlinear oscillators. The mathematical

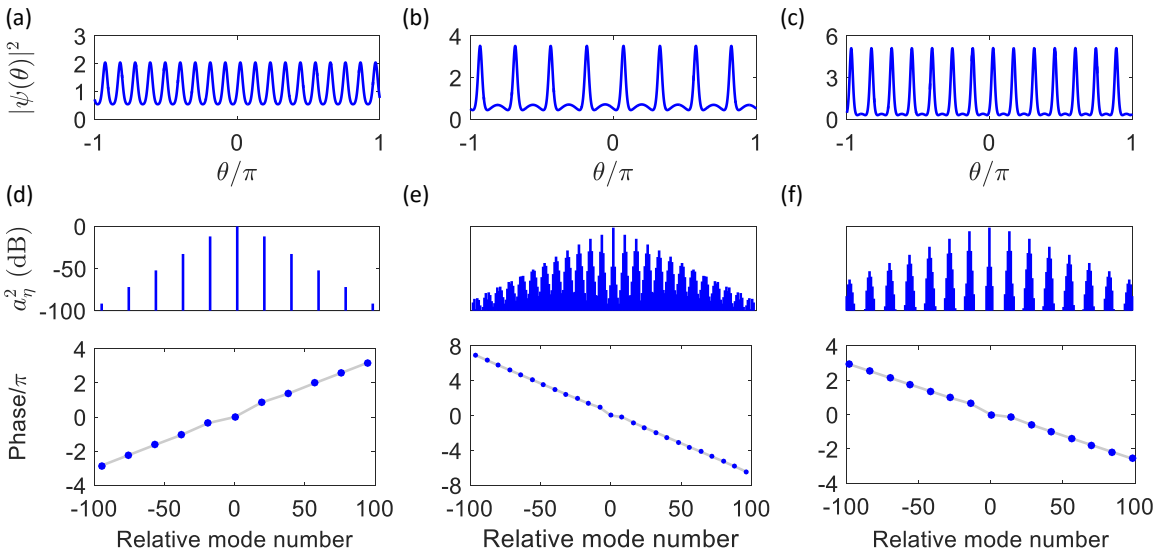

Fig. 2.3.2: Steady-state frequency combs for the parameters used for the gain profiles in Fig. 2.3.1(d)-(f). (a) and (d) correspond to Fig. 2.3.1(d), (b) and (e) to Fig. 2.3.1(e), and finally (c) and (f) to Fig. 2.3.1(f). (a)-(c) show the intra-cavity field envelope while (d)-(f) are the power spectra (top column) and phase spectra (bottom column). The phase spectra show the alignment of the phases for phase-locked combs.

tool which allows us to go from the LLE to the coupled oscillator picture is the discrete-time Fourier transform (DTFT). DTFT of Eq. (3.3.1), with the angle around the resonator θ and the comb mode number η as conjugate variables of the transform, leads to a set of coupled nonlinear ordinary differential equations (ODEs) [69],

$$\frac{\mathrm{d}\tilde{a}_\eta}{\mathrm{d}\tau} = -(1 + \mathrm{i}\alpha - \mathrm{i}\frac{d_2}{2}\eta^2)\tilde{a}_\eta + \mathrm{i}\sum_{l,m,n}\tilde{a}_l\tilde{a}_m^*\tilde{a}_n\,\delta_{\eta_{lmn}\eta} + \tilde{F}_\eta, \tag{2.4.1}$$

for the temporal evolution of the complex comb teeth amplitudes $\tilde{a}_\eta$ constituting the intra-cavity field envelope $\psi(\theta,\tau)$. For the Fourier pairs we have used the following equations and sign convention [79]:

$$\tilde{a}_\eta(\tau) = \frac{1}{2\pi}\int_{-\pi}^{\pi}\mathrm{d}\theta\,\psi(\theta,\tau)\,\exp(-\mathrm{i}\eta\theta), \tag{2.4.2}$$

and

$$\psi(\theta,\tau) = \sum_{\eta=-\infty}^{\infty}\tilde{a}_\eta(\tau)\,\exp(+\mathrm{i}\eta\theta), \tag{2.4.3}$$

The set of equations (3.3.2) (for difference integer values of the mode number η) are equivalent to the LLE [80]. In the coupled-modes picture, each comb mode labeled

with the integer η is a nonlinear oscillator and one of the coupled ODEs follows the temporal evolution of its complex amplitude $\tilde{a}_\eta(\tau)$. In Eq. (3.3.2), δ_{ij} (for integers i and j) is the Kronecker delta, $\eta_{lmn} = l - m + n$, and l, m, and n are integers; the summation runs over mode numbers l, m, and n satisfying $l - m + n = \eta$, a condition enforced by phase matching. The modes are numbered relative to the mode closest to the pump (the pumped mode) for which $\eta = 0$. We consider CW pumping and therefore $\tilde{F}_\eta = \delta_{0\eta} F_\mathrm{P} \exp(\mathrm{i}\phi_\mathrm{P})$, F_P being the pump magnitude as defined following Eq. (3.3.1) and ϕ_P representing its phase. In the frequency domain, Turing roll have power spectra which usually have multiple-FSR spacing between their adjacent teeth. In the model introduced here, $\eta \in \{0, \pm\mu, \pm 2\mu, \ldots, \pm N\mu\}$, where N is a positive integer and the integer $\mu \geq 1$ is the mode number at which MI gain peaks (as in Fig. 2.3.1(e)-(f)) and the primary combs are generated [76, 77, 81].

Equations of motion for the comb teeth magnitudes a_η and phases ϕ_η can readily be found by using $\tilde{a}_\eta = a_\eta \exp(\mathrm{i}\phi_\eta)$ in Eq. (3.3.2), dividing by $\exp(\mathrm{i}\phi_\eta)$, and separating the real and imaginary parts. The resulting equations read

$$\begin{aligned}\frac{\mathrm{d}}{\mathrm{d}\tau}\ln(a_\eta) = -1 + \frac{a_{-\eta}}{a_\eta} a_0^2 \sin(\phi_\eta + \phi_{-\eta} - 2\phi_0) + \frac{F_\mathrm{P}}{a_\eta}\cos(\phi_\mathrm{P} - \phi_\eta)\delta_{0\eta} \\ - \frac{a_0}{a_\eta}\sum_l a_l\{2a_{\eta+l}\sin(\phi_0 - \phi_l + \phi_{\eta+l} - \phi_\eta) + a_{\eta-l}\sin(\phi_l - \phi_0 + \phi_{\eta-l} - \phi_\eta)\},\end{aligned} \tag{2.4.4}$$

$$\begin{aligned}\frac{\mathrm{d}}{\mathrm{d}\tau}\phi_\eta = 2a_0^2 - \alpha + \frac{1}{2}d_2\eta^2 + \frac{a_{-\eta}}{a_\eta}a_0^2\cos(2\phi_0 - \phi_\eta - \phi_{-\eta}) + \frac{F_\mathrm{P}}{a_\eta}\sin(\phi_\mathrm{P} - \phi_\eta)\delta_{0\eta} \\ + \frac{a_0}{a_\eta}\sum_l a_l\{2a_{\eta+l}\cos(\phi_0 - \phi_l + \phi_{\eta+l} - \phi_\eta) + a_{\eta-l}\cos(\phi_l - \phi_0 + \phi_{\eta-l} - \phi_\eta)\}.\end{aligned} \tag{2.4.5}$$

In this work, the focus is on the phase evolution as comb teeth powers grow with time respecting $a_\eta(\tau) = a_{-\eta}(\tau)$. Therefore, while Eq. (3.8.3) is included for completeness, we won't refer to it after here. The phase equations, however, will be used in our analysis in the following sections.

As a natural consequence of the resonator chromatic and geometric modal dispersion and as evidenced by experiments and numerical simulations, in stable non-homogeneous solutions of the LLE (or the equivalent coupled ODEs of Eq. (3.3.2)), the power of the comb teeth falls off with increasing relative mode nubmer. Additionally, the pumped mode is usually much larger than the other modes; a condition which we refer as the strong pumping regime. In the absence of third- and higher-order dispersion, the power spectrum of these solutions is symmetric with respect to the pumped mode [37, 54, 77]. These conditions can be seen to clearly hold in Fig. 2.3.2. Consequenctly, we consider a truncation of the set of equations (3.3.2) in our study of phase locking based on MI. Similar truncated models have been successfully used in studies of pulse dynamics in fibers [82], microresonator-based frequency combs [83], and mode-locked lasers [84]. In the following sections, we first study the pumped mode and then consider 3- and 5-mode truncations of Eq. (3.3.2).

2.5 Injection Locking of the Pumped Mode

We first consider the magnitude and phase equations for the pumped mode,

$$\frac{\mathrm{d}}{\mathrm{d}\tau}\ln(a_0) = \frac{F_\mathrm{P}}{a_0}\cos(\phi_\mathrm{P}-\phi_0) - 1, \tag{2.5.1a}$$

$$\dot{\phi}_0 = \frac{F_\mathrm{P}}{a_0}\sin(\phi_\mathrm{P}-\phi_0) - \alpha + a_0^2. \tag{2.5.1b}$$

These pumped mode magnitude and phase equations include no linear contributions from $a_{\eta\neq 0}$ and, as a result, for the strong pumping regime we have dropped corrections arising from the primary and secondary sidebands (a_η^2 terms with $\eta = \pm 1, \pm 2$) in these equations. (We will verify the validity of this approximation using numerical integration of the truncated equations and the full LLE in what follows.) Hence, the pumped mode equations can be studies independently of the sidebands. Numerical integration of the pumped mode equations shows that a_0 settles on a fast time scale to the equilibrium intra-cavity field $a_0 = |\psi_\mathrm{e}|$ [85]. After the sidebands $a_{\pm 1}$ start to

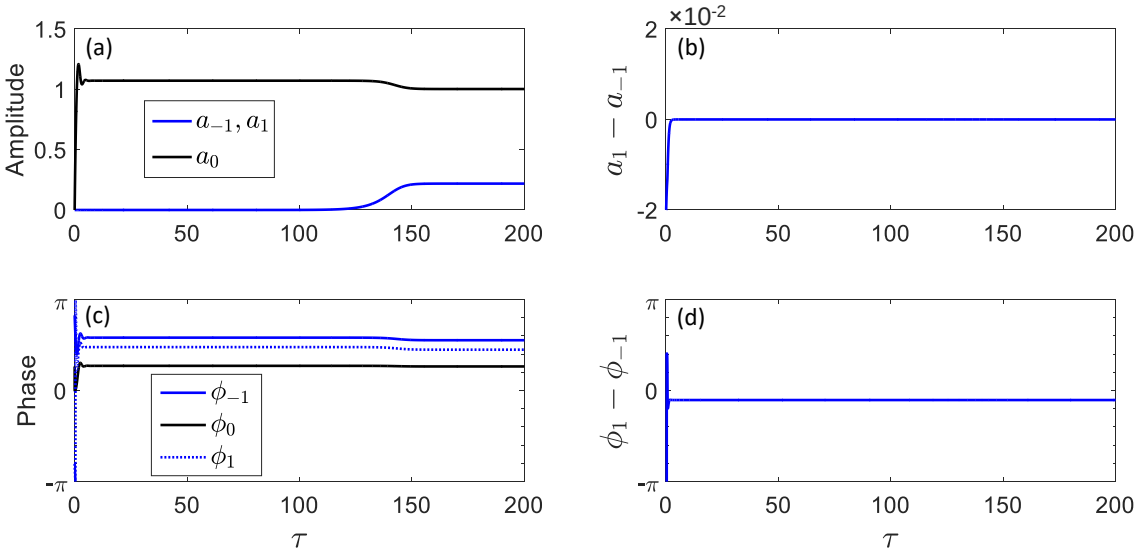

Fig. 2.5.1: Evolution of the comb teeth magnitudes and phases in the three-mode truncation of the LLE. (a) Pumped mode and sideband magnitudes. (b) The difference between the sideband magnitudes, which tend to zero soon after the comb starts evolving irrespective of the initial conditions, and confirming the power spectrum symmetry assumption. (c) Pumped mode and sideband phases. (d) The difference between the sideband phases, which tend to a constant irrespective of the initial conditions.

grow (i.e., at $\tau \approx 130$ in Fig. 2.5.1(a) and (c)), the relative change in the pumped mode power is small. Subsequently, a_0 can be treated as a constant to first order in $a_{\eta\neq 0}$. With that in mind, the phase equation, Eq. (3.3.3b), can be written as

$$\frac{\mathrm{d}\Phi_0}{\mathrm{d}\tau} = -B(\sin\Phi_0 - K), \tag{2.5.2}$$

where $\Phi_0 = \phi_\mathrm{P} - \phi_0$, $B = F_\mathrm{P}/a_0$, and $K = a_0(\alpha - a_0^2)/F_\mathrm{P}$. This equation is exactly in the form of the Adler equation for injection locking [86]. In his 1946 paper, Adler showed that the condition for synchronization through injection locking is $|K| < 1$. This condition corresponds to

$$|\alpha - a_0^2| < \frac{F_\mathrm{P}}{a_0} \tag{2.5.3}$$

and is guaranteed to hold when the intra-cavity flat-lock solution is achieved because the steady-state magnitude $a_0 = |\psi_\mathrm{e}|$ satisfies

$$a_0^2[1 + (\alpha - a_0^2)^2] = F_\mathrm{P}^2, \tag{2.5.4}$$

and therefore $F_{\rm P}^2/a_0^2 = 1 + (\alpha - a_0^2)^2 > (\alpha - a_0^2)^2$. For pump power $F_{\rm P}^2$ chosen such that $|\psi_{\rm e}|^2 \gg \alpha$, satisfying the synchronization condition becomes harder and this is where the system enters a chaotic state, as has been studied, for instance, in [70, 77]. Equation (2.5.2) can be integrated analytically and the final (steady-state) value of ϕ_0 equals $2\tan^{-1}[(\sqrt{1-K^2}-1)/K] = 0.2718\pi$ is within %3 of the value 0.26248π found from the numerical integration of the LLE of Eq. (3.3.1). We note that $\phi_{\rm P}$ defines a phase reference and its specific value is immaterial.

2.6 Few-mode Truncations of the LLE

2.6.1 Three-mode Truncation

Equations of the temporal evolution of the centered phase averages $\zeta_\eta = \bar{\phi}_\eta - \phi_0$, where the phase average $\bar{\phi}_\eta = (\phi_\eta + \phi_{-\eta})/2$ is centered to the pumped mode phase ϕ_0, can be found from Eqs. (3.8.4) and (3.3.3b). This equation, for the case of 3-wave truncation of the LLE ($\eta \in \{-\mu, 0, \mu\}$) reads

$$\frac{\mathrm{d}}{\mathrm{d}\tau}\zeta_\mu = \frac{1}{2}d_2\mu^2 + a_0^2[1+\cos(2\zeta_\mu)] - \frac{F_{\rm P}}{a_0}\sin(\phi_{\rm P}-\phi_0), \tag{2.6.1}$$

and can be integrated analytically:

$$\tan\zeta_\mu = \sqrt{\left|\frac{C+2}{C}\right|}\tanh[\sqrt{|C(C+2)|}a_0^2(\tau-\tau_0)]. \tag{2.6.2}$$

In this equation, $C = d_2\mu^2/2a_0^2 - F_{\rm P}\sin(\phi_{\rm P}-\phi_0)/a_0^3$, and τ_0 accounts for initial conditions. Equation (3.3.5) holds when $\rho_{\rm e} > |2\rho_{\rm e} - \alpha + d_2\mu^2/2|$, which is automatically satisfied when MI gain exists (see Sec. 2.3). The $\tanh(\cdot)$ function rapidly approaches unity as $\tau \to \infty$, and so $\bar{\phi}_\mu$ reaches the same constant irrespective of the initial conditions. As $\bar{\phi}_\mu - \phi_0$ is fixed, the phases $\phi_{\pm\mu}$ should take values symmetrically located relative to the constant average and follow the changes in ϕ_0, as can be seen in Fig. 2.5.1(c). This constraint on the phases was noticed numerically by Wen

et al. and termed "*phase anti-symmetrization*"; the expression given above simply justifies why phases anti-symmetrize. Therefore, the 3-mode truncation establishes that centered phase average ζ_μ can be treated as a constant to first order in $a_{\eta\neq 0}$. Note, however, that this approximation says nothing about the evolution of the phase differences (PDs) $\Delta_\mu = (\phi_\mu - \phi_{-\mu})/2$; the temporal evolution of the PDs simply follows $\mathrm{d}\Delta_\mu/\mathrm{d}\tau = 0$, stating that in the 3-mode truncation, the sideband phases will rapidly lock and become equal, as seen in Fig. 2.5.1(d). It is noteworthy that the assumed symmetry of the sideband powers (noted following Eq. (3.8.3)) indeed holds, as seen in Fig. 2.5.1(b).

2.6.2 Five-mode Truncation

We now proceed one step further by including the second pair of sidebands,$\eta = \pm 2\mu$. Figure 2.6.1 shows that the behavior of the pumped mode and primary sidebands magnitudes and phases does not change noticeably compared to the 3-mode truncation; this change is less than %2. However, the PD equations for $\eta = \mu$ changes. The temporal evolution of the PDs take the form

$$\frac{\mathrm{d}\Delta_\mu}{\mathrm{d}\tau} = -2a_0 a_{2\mu}\sin(\zeta_{2\mu} - 2\zeta_\mu)\sin(\Delta_{2\mu} - 2\Delta_\mu), \tag{2.6.3a}$$

$$\frac{\mathrm{d}\Delta_{2\mu}}{\mathrm{d}\tau} = -a_0\frac{a_\mu^2}{a_{2\mu}}[2\sin(\zeta_2) + \sin(\zeta_{2\mu} - 2\zeta_\mu)]\sin(\Delta_{2\mu} - 2\Delta_\mu). \tag{2.6.3b}$$

We note that these equations are written in the strong pumping regime to first order in $a_{\eta\neq 0}$, and can be combined to give a separable equation

$$\frac{\mathrm{d}}{\mathrm{d}\tau}(\Delta_{2\mu} - 2\Delta_\mu) = -a_0 f\sin(\Delta_{2\mu} - 2\Delta_\mu), \tag{2.6.4}$$

in which

$$f = 2\frac{a_\mu^2}{a_{2\mu}}\sin(\zeta_2) + \left(\frac{a_\mu^2}{a_{2\mu}} - 4a_{2\mu}\right)\sin(\zeta_{2\mu} - 2\zeta_\mu). \tag{2.6.5}$$

Equation (2.6.4) has analytical solution of the form

$$\tan[s(\tau)] = \tan[s(\tau_1)]\exp[-a_0 f(\tau - \tau_1)], \tag{2.6.6}$$

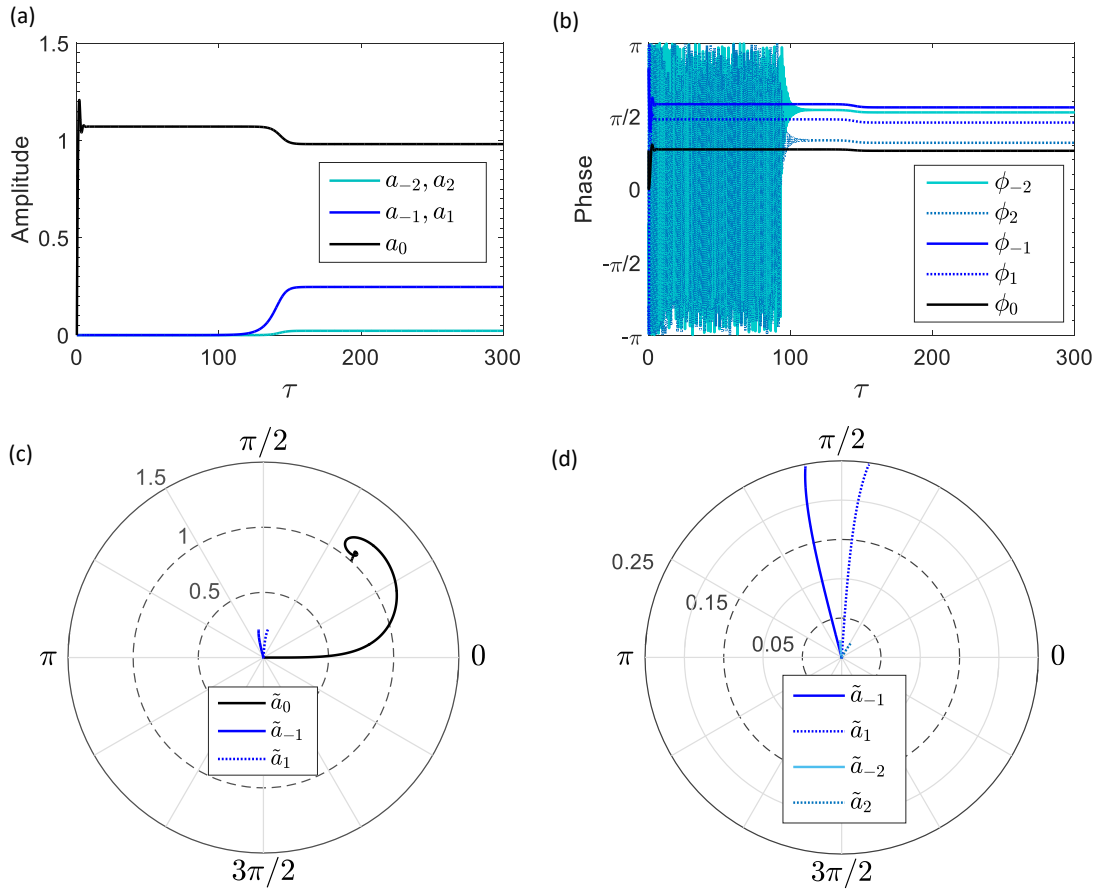

Fig. 2.6.1: Evolution of the pumped mode and sideband magnitudes and phases in the five-mode truncation of the LLE for comb parameters as in Fig. 2.3.1(d). (a) Pumped mode and sideband magnitudes. (b) Pumped mode and sideband phases. (c) Evolution of the comb teeth complex amplitudes in polar coordinates. (d) Zoomed-in version of (c) showing the complex amplitude of the first and second sidebands. While different initial conditions lead to different final phase values, the relationship $\phi_{2\mu} - \phi_{-2\mu} = 2(\phi_\mu - \phi_{-\mu})$ is always satisfied in the steady state. In the example shown here $(\phi_{2\mu} - \phi_{-2\mu})/2 = \phi_\mu - \phi_{-\mu} = -0.104\pi$.

where $s(\tau) = [\Delta_{2\mu}(\tau) - 2\Delta_\mu(\tau)]/2$ (called the phase misalignment parameter, for reason that will be clear shortly) and τ_1 is a constant of integration which can physically be thought of as marking the moment when second sideband powers $a_{\pm 2\mu}$ are above noise level such that divisions by $a_{2\mu}$ in Eqs. (2.6.3b) and (2.6.5) are mathematically valid. The integration leading to the above equation relies on the phase anti-symmetrization established in the 3-mode truncation, and shows that if $f > 0$, irrespective of the value of $\Delta_{2\mu} - 2\Delta_\mu$ at τ_1, the exponential decay will take $\Delta_{2\mu} - 2\Delta_\mu$ to zero. Physically, this amounts to the alignment of the phases of the first and second

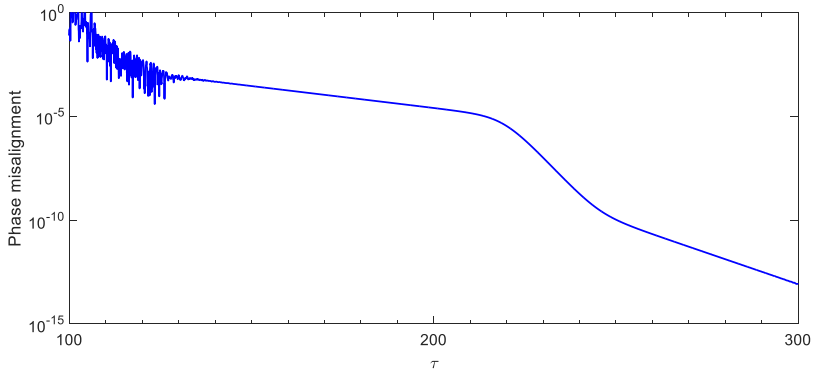

Fig. 2.6.2: The exponential decay of the phase misalignment parameter $s(\tau)$ with the normalized time τ in the full LLE, as predicted by Eq. (2.6.6). The early random oscillations are due to the small power in the sidebands early on in the generation of the comb, which leads to their phase wondering. The change in the slope of $s(\tau)$ reflects the growth of the sidebands as the comb evolves and is also captured by the few-mode models shown in Figs. 2.5.1 and 2.6.1. Note the dependence of the parameter f on the sideband powers in Eq. (2.6.5).

sideband pairs, because $\Delta_{2\mu}/2\mu = (\phi_{2\mu} - \phi_{-2\mu})/4\mu$ and $2\Delta_{\mu}/2\mu = (\phi_{\mu} - \phi_{-\mu})/2\mu$ are, respectively, slopes of the lines connecting $\phi_{2\mu}$ to $\phi_{-2\mu}$ and ϕ_{μ} to $\phi_{-\mu}$ in the phase vs. mode number plane. As a result, Eq. (2.6.6) predicts that the phase misalignment is dragged to zero upon phase locking. We show in Fig. 2.6.2 evolution of the misalignment parameter s as a function of the normalized time, found from the integration of the full LLE. This figure confirms that the requirement $f > 0$ is in fact met and the prediction of the exponential decay of $s(\tau)$ is correct (note the constant slopes and the logarithmic scale of the vertical axis). The changes in the slope at $\tau = 220$ and $\tau = 250$ occur because of the growth of the sideband powers as the comb evolves (recall the dependence of f on the sideband magnitudes in Eq. (2.6.5)). The reason these changes are shifted in time compared to those shown in Figs. 2.5.1 and 2.6.1 is that the power of seeding noise in our integration of the few-mode equations were not exactly matched with that in the split-step integration of the full LLE where noise power was smaller. The phase alignment described through the truncated equations and analytical expression in this section, justify the aligned phases of the Turing rolls shown in the lower panel of Figs. 2.3.2(d)-(f).

2.7 Summary and Outlook

In conclusion, based on few-mode truncations of the Lugiato-Lefever equation, we find analytical expressions which unfold the essence of the temporal evolution of comb teeth phases from random vacuum fluctuations toward locked steady states of sharply peaked pulses in the presence of modulational instability. We show that the pumped mode of the comb injection-locks to the driving pump laser frequency through the Adler equation. We also find, under assumptions motivated by experiments and using a three-mode truncation of the LLE, that sideband phases anti-symmetrize, i.e., their average becomes fixes with respect to the pumped mode phase before phase locking occurs. Considering the 5-mode truncation of the LLE, we drive an analytical expression describing how the phases of the comb teeth align irrespective of their initial values supplied by noise (random vacuum fluctuations). This analysis shows that the phase misalignment of the comb sidebands dies exponentially with time till these phases all lie on a straight line. We confirm this prediction through numerical integration of the full LLE. The LLE is an externally-driven, damped nonlinear Schrödinger equation and has been used for describing a variety of physical phenomena in different nonlinear systems. Therefore, the results presented here apply also to other NLSE systems beyond microcombs. Extension of the analysis presented here to the case of microcomb soliton formation leads to a novel self-synchronization model [87].

CHAPTER 3

SELF-SYNCHRONIZATION PHENOMENA IN MICRO-RESONATOR-BASED OPTICAL FREQUENCY COMBS

"The best discipline for making sure you understand something is to simplify it, simplify relentlessly."

Lloyd N. Trefethen, "Spectral Methods in Matlab" (2001)

The study of phase locking presented in Chapter 2 focused on hyperparametric oscillations supported by parametric gain, which leads to modulational instability and the emergence of a pulse train (Turing patterns). But optical frequency combs in microresonators lead to the generation of short pulses even when parametric gain and modulational instability are absent. In this chapter the study presented in the previous chapter is extended and a self-synchronization model which describes phase locking for both Turing patterns and optical temporal solitons is developed. As noted in the previous chapter, the Lugiato-Lefever equation (LLE) is a damped driven nonlinear Schrödinger equation (NLSE) which has been used to understand a range of physical phenomena in diverse systems. I show that studying this equation in the context of optical hyperparametric oscillators in dissipative cavities, one is led to a new, reduced nonlinear oscillator model governing the spontaneous creation of sharply peaked pulses in optical resonators. I identify attracting solutions for this model which correspond to stable cavity solitons and Turing patterns, and study their degree of stability. The reduced model embodies the fundamental connection between mode synchronization and spatiotemporal pattern formation,

and represents a novel class of self-synchronization processes in which coupling between nonlinear oscillators is governed by energy and momentum conservation.[1]

3.1 Introduction

Self-organization is an intriguing aspect of many nonlinear systems far from equilibrium, which leads to the emergence of coherent spatiotemporal structures [88]. Many such nonlinear systems have been modeled by the externally driven damped nonlinear Schrödinger equation (NLSE). Examples include such diverse systems as Josephson junctions, charge-density-waves, quantum Hall ferromagnets and ferromagnets in microwave fields, RF-driven plasmas, shear flows in liquid crystals, and atmospheric and ocean waves; for a partial list see [67] and references [1-18] therein. The NLSE admits spatiotemporal sharply peaked solutions (e.g., dissipative solitons), but a central mystery remains: while it is understood that such solutions occur because of *phase locking*, no formal model is currently available to explain the underlying self-synchronization mechanism. In this paper, we introduce a reduced phase model which captures the fundamental connection between mode synchronization and pulse formation. While the results presented here are generic from the mathematical perspective, considering them within a specific physical system allows a more lucid presentation and interpretation of the results. Consequently, we consider the damped driven NLSE in the context of frequency combs based on dissipative optical cavities [1, 58, 89].

A high-Q (quality-factor) optical resonator made of Kerr-nonlinear material and pumped by a continuous wave (CW) laser forms a hyper-parametric oscillator based on nonlinear four-wave mixing (FWM) [53, 71], and can generate an optical frequency comb: an array of frequencies spaced by (an integer multiple of) the resonator free

[1] This chapter is based on results presented in [87].

spectral range (FSR). The generation of a frequency comb with equidistant teeth is, however, not enough; temporal pulse generation requires also the mutual phase locking (synchronized oscillation) of the frequency comb teeth. Unlike pulsed lasers, pulsation in dissipative optical resonators requires neither active nor passive mode locking elements (e.g. modulators or saturable absorbers) [1, 90]. Rather, pulsed states arise naturally from a simple damped driven NLSE, in this context commonly called the Lugiato-Lefever equation (LLE) [54, 57–61, 67]. Two categories of stable pulsed solutions have been identified for the LLE: stable modulation instability (MI, also called hyper-parametric oscillations or Turing rolls) and stable cavity solitons [77, 91]. Owing to their stability, these phase-locked combs have been used to demonstrate chip-scale low-phase-noise radio frequency sources [14] and high-speed coherent communication [50, 51].

Phase locking in optical microresonators has been studied in terms of the cascaded emergence of phase-locked triplets [65] and injection locking of overlapping comb bunches [64]. Additionally, few-mode models have explained the phase offset between the pumped mode and the rest of the comb teeth [85, 92]. More recently, Wen *et al.* [66] have emphasized the link between oscillator synchronization—most famously described by the Kuramoto model—and the onset of pulsing behavior. However, while stable ultrashort pulses have been demonstrated in a variety of platforms [30, 37, 53, 54], their underlying phase locking mechanism is still unknown. The reduced model introduced in this paper governs the nonlinear interactions responsible for the spontaneous creation of pulses in optical resonators. The modal interactions in the LLE are the result of the cubic (Kerr) nonlinearity and their specific form reflects conservation of energy and momentum. Consequently, the phase couplings in our model are *ternary* (i.e., they involve three-variable combinations) rather than binary, as in typical phase models [93]. Our model admits attracting solutions which correspond to stable cavity solitons and Turing rolls. We show that the stability of

steady-state LLE solutions in the strong pumping regime can be studied easily using this model. Moreover, our model sheds light on the role of MI and chaos in the generation and stability of Turing rolls and solitons.

3.2 Is there a self-synchronization process is action in optical microcombs?

Speaking of the modal phases is valid when the amplitudes have grown above the noise level. As we will explain in the remainder of this chapter, the transition of the system towards a phase-locked state takes place in 3 stages. First the comb teeth powers grow and, for a system with negligible third- and higher-order dispersion, a power spectrum symmetric around the pump is created. Then, the phases anti-symmetrize as a result of the strong interaction of the pump and comb teeth pairs symmetrically located around the pump, see Figs. 2(a, b) in [66]. Phase synchronization occurs during the final phase, which is described by the reduced model developed in this chapter. This phase locking model shows that for a single soliton or a Turing roll, the phase spectrum consists of phases lying on a straight line (modulo an offset with respect to the pumped mode phase [66, 92]). It should be born in mind that in the LLE there is a rich interplay between the comb teeth power and phase evolution through the Kerr nonlinearity. Solutions more complicated than a single soliton (i.e., those involving multiple isolated solitons) are also possible for the LLE and are routinely observed in numerical simulations as well as experiments. The power and phase spectra of these solutions have more features than described in the manuscript for a single soliton. However, these more complicated results and their spectra can easily be explained through the properties of the Fourier transform when the spectrum of a single soliton or Turing roll is known. For instance, for the case of two solitons separated by an angle θ_0 (such that they do not interact), the modulation of the power envelope and phase spectra are understood as a result of the superposition of the discrete-time

Fourier transforms of the pulse shapes, one shifted with respect to the other (e.g., $\psi(\theta)$ and $\psi(\theta - \theta_0)$, leading to a spectrum given by $\tilde{a}_\eta + \tilde{a}_\eta \exp(-\mathrm{i}\eta\theta_0)$). Note that because of the symmetry of a circular resonator, it is always possible to shift one of the pulses such that its peak is centered on the origin of the θ axis.

The objective of this chapter is to uncover the underlying synchronization mechanism leading to phase locking in the LLE, and to that end I use experimentally-motivated assumptions about the power spectrum to separate the amplitude dynamics from the phase dynamics. If indeed a phase locking mechanism exists in the LLE, when a phase-locked steady-state solution of the LLE, e.g. a sharp pulse, is used as initial condition (for the propagation with time of the waveform under the LLE) and its phase spectrum is randomized, one would expect the phase locking mechanism to recover the pulse phase after some time. However, one should remember that because of the interplay of the power and phase dynamics, it is possible to get more than one local peak after randomizing the phases and that would lead to a phase-locked solution with more than one peak, as shown in Fig. 3.2.1(a). To see the influence of separating power and phase dynamics in the LLE, it is possible to enforce the power spectrum of a single soliton solution of the LLE in every step of integration when propagating the solution in time under the LLE. Then, one can see that the system converges to the simpler phase-locked state of a single soliton, as seen in Fig. 3.2.1(b). The slope of the line of the phase profile, however, is absolutely immaterial, as will be argued through the stability analysis of the solutions in this chapter. This arbitrary slope depends on the initial random phase profile when the locking process kicks in and its arbitrary character is a result of the rotational symmetry of the resonator and, consequently, the LLE which describes comb generation in the symmetric structure. This symmetry is present in the reduced model as well. The slope can be removed simply by a change of origin of the azimuthal angle around the cavity (an added linear phase), which is again a straightforward consequence of the symmetry

of the system and the properties of Fourier transform. In Fig. 3.2.2, we have shown the phase profile of the recovered soliton of Fig. 3.2.1(b). Figure Fig. 3.2.2(a) shows the phase "wrapped" at jumps of π, Fig. 3.2.2(b) shows the phase after it has been unwrapped, and Fig. 3.2.2(c) depicts the unwrapped phase after the constant slope has been removed through the addition of a linear phase. This figure clearly shows that for a sharply peaked solution of the LLE comb teeth phases lie on a straight line (modulo the pumped mode phase offset noted earlier). For numerical simulations shown in Fig. 3.2.1(b) and Fig. 3.2.2, I have used an extreme phase randomization, i.e., random phases chosen from a uniform distribution over $(-\pi, \pi]$. If a normal distribution with smaller standard deviation, of for example $\pi/4$, is used instead, a single sharp pulse, rather than multiple pulses, is more likely to be recovered even without enforcing the single pulse power spectrum.

3.3 Reduction of the Lugiato-Lefever Equation

Creation of sharply peaked solutions in dissipative optical cavities relies on the establishment of a fine balance between nonlinearity, dispersion (or, in the case of spatial cavities, diffraction), parametric gain, and cavity loss [75]. The dynamics of this complex interaction is described by the LLE, which is a nonlinear partial differential equation with periodic boundary conditions for the intra-cavity field envelope in a slow and a fast time variable [59, 60] or, equivalently, in time and the azimuthal angle around the whispering-gallery-mode resonator [61]. The cubic nonlinear term in the LLE leads to a rich interplay between the power and phase dynamics of the comb teeth. To uncover the self-synchronization mechanism leading to phase locking in this equation, as will become clear in this section, we make experimentally-motivated assumptions on the power spectrum. This simplification allows us to separate the evolution of the power spectrum from that of the phase and arrive at a reduced model

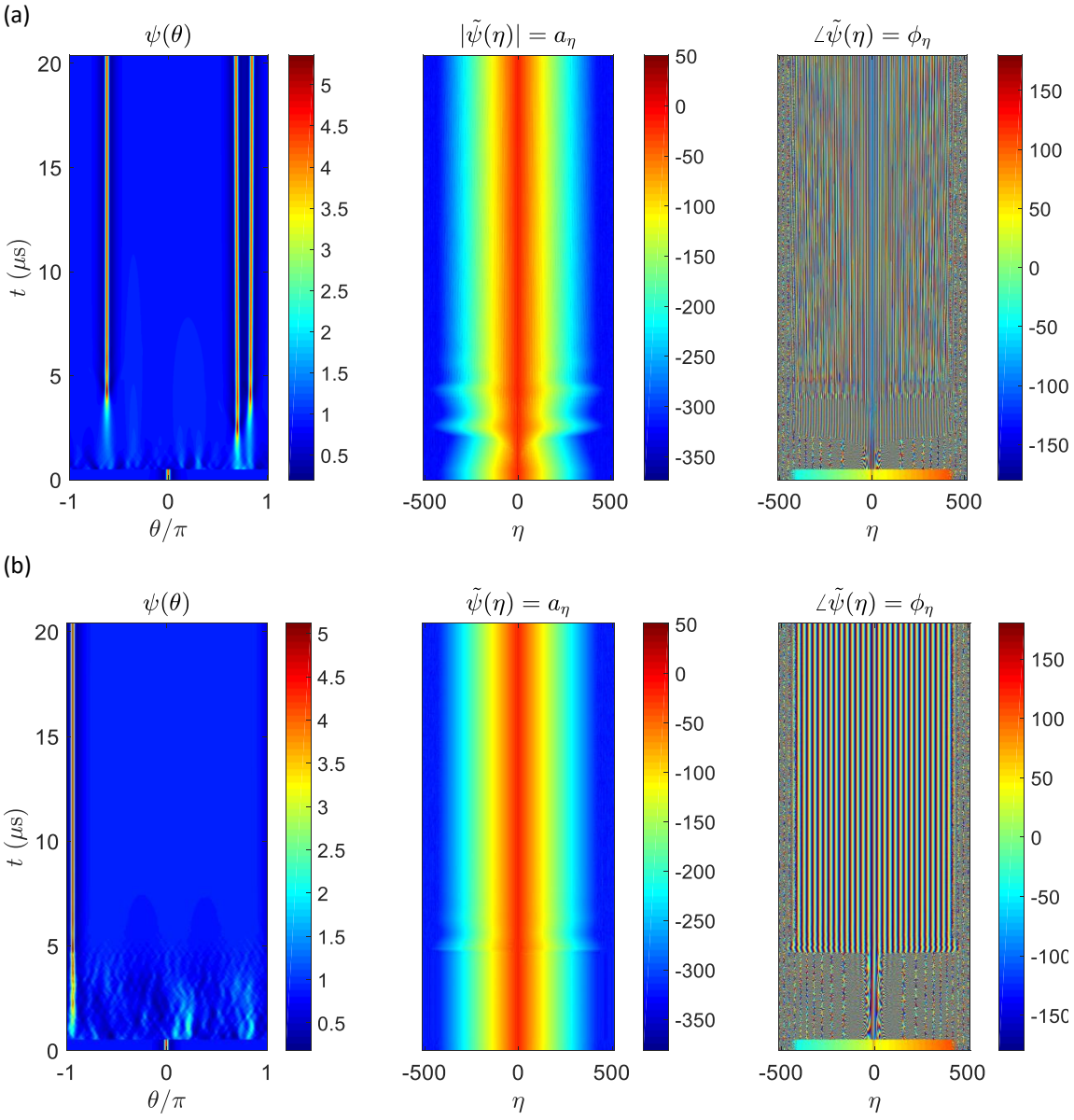

Fig. 3.2.1: Evolution of a soliton pulse under the Lugiato-Lefever equation after randomizing its phase spectrum profile. (a) The evolution of a soliton pulse power spectrum with randomized phase profile under the LLE. The phase of the soliton is randomized at $t = 0.5$ μs. (b) The evolution of a soliton spectrum with randomized phase profile under the LLE, when in every step of integration the power spectrum of the initial soliton is enforced. As in (a), the phase of the soliton is randomized at $t = 0.5$ μs. The left panel in both (a) and (b) is the intra-cavity field envelope, the middle panel is (the square root of) the power spectrum, and the right panel is the phase spectrum. The phase profile in the left panel in (b) is further studied in Fig. 3.2.2. The randomized phases in both cases (a) and (b) are chosen from a uniform distribution over $(-\pi, \pi]$.

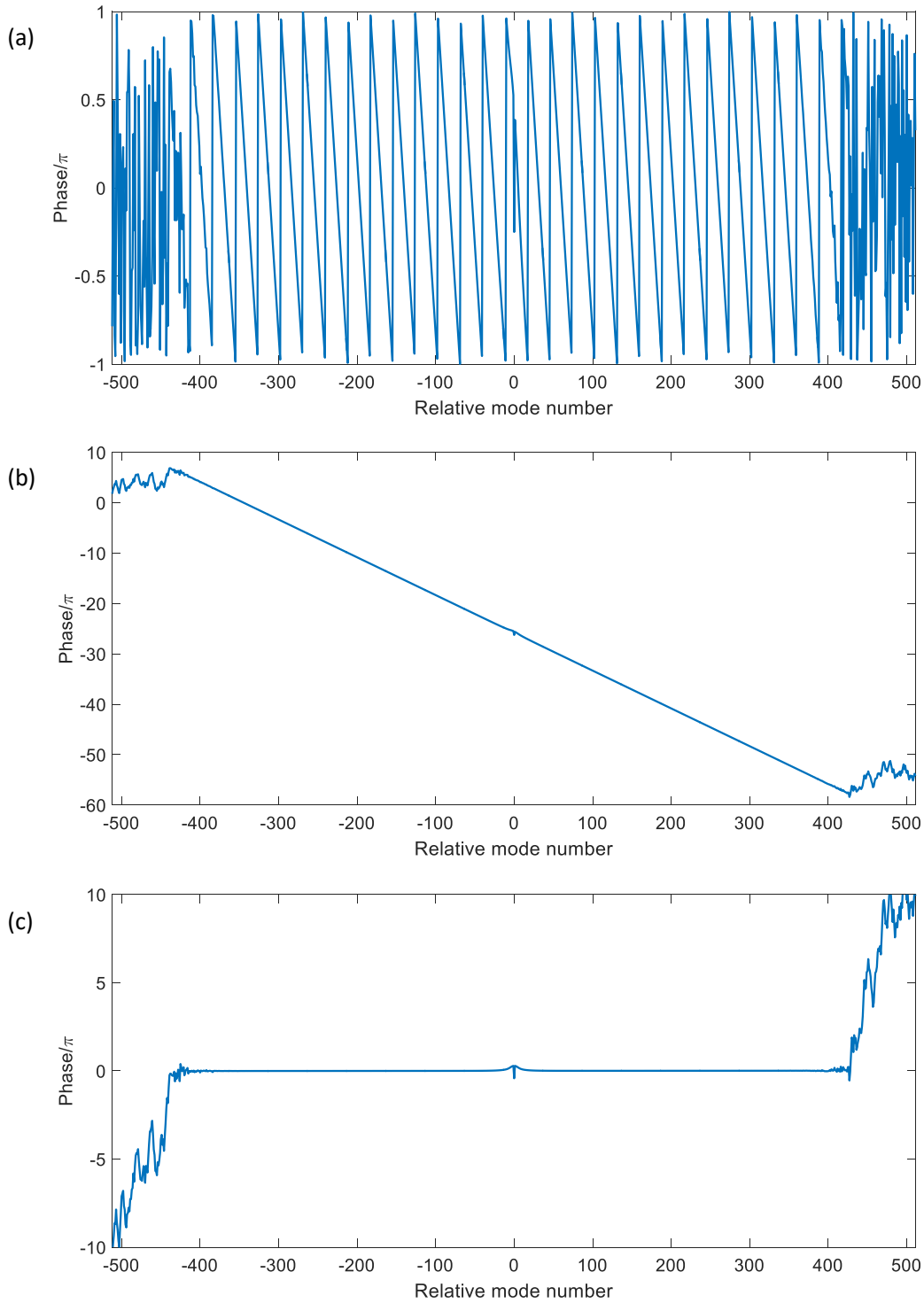

Fig. 3.2.2: Closer look at the phase spectrum profile of a soliton pulse. (a) The phase profile of the soliton pulse recovered in Fig. 3.2.1(b). The jumps arise from wrapping the phase at jumps of π. (b) The phase profile shown in (a) can be unwrapped. It is seen that the phases of the comb teeth lie on a straight line, except for the pumped mode phase which has some offset from the rest of the phases. (c) The unwrapped phase profile when the constant slope has been removed through the addition of a linear phase, equivalent to a change of the θ-axis origin.

(a phase model) which embodies the fundamental phase locking mechanism enabled by the nonlinearity in the LLE.

In normalized form, the LLE reads

$$\frac{\partial\psi}{\partial\tau} = -(1+\mathrm{i}\alpha)\psi - \mathrm{i}\frac{d_2}{2}\frac{\partial^2\psi}{\partial\theta^2} + \mathrm{i}|\psi|^2\psi + F, \tag{3.3.1}$$

where $\psi(\theta,\tau)$ and $F(\theta,\tau)$ are the field envelope and pump amplitude respectively, both normalized to the sideband generation threshold, α and d_2 are the pump-resonance detuning and second-order dispersion coefficient, each normalized to the half-linewidth of the pumped resonance, and τ is the time normalized to half of the cavity photon lifetime [61]. Discrete-time Fourier transform of Eq. (3.3.1) (with the azimuthal angle θ and comb mode number η as conjugate variables [79]), yields an equivalent set of coupled nonlinear ordinary differential equations (ODEs) [69],

$$\frac{\mathrm{d}\tilde{a}_\eta}{\mathrm{d}\tau} = -(1+\mathrm{i}\alpha - \mathrm{i}\frac{d_2}{2}\eta^2)\tilde{a}_\eta + \mathrm{i}\sum_{l,\,m,\,n}\tilde{a}_l\tilde{a}_m^*\tilde{a}_n\,\delta_{\eta_{lmn}\eta} + \tilde{F}_\eta, \tag{3.3.2}$$

for the temporal evolution of the complex comb teeth amplitudes $\tilde{a}_\eta$ (with magnitude $|\tilde{a}_\eta| = a_\eta$ and phase $\angle\tilde{a}_\eta = \phi_\eta$) which make up the spatiotemporal field envelope through $\psi(\theta,\tau) = \sum_{\eta=-N}^{N}\tilde{a}_\eta\exp(\mathrm{i}\eta\theta)$. In this picture, each comb mode is a nonlinear oscillator and one of the coupled ODEs follows the temporal evolution of its complex amplitude. In Eq. (3.3.2), δ_{pq} (for integers p and q) is the Kronecker delta, $\eta_{lmn} = l - m + n$, and l, m, and n are integers; modes are numbered relative to the pumped mode for which $\eta = 0$. We consider CW pumping where $\tilde{F}_\eta = \delta_{0\eta}F_\mathrm{P}\exp(\mathrm{i}\phi_\mathrm{P})$, F_P being proportional to the pump magnitude and ϕ_P representing its phase.

Experimentally, Turing rolls arise from the intra-cavity equilibrium field through modulation instability of vacuum fluctuations and correspond, in the frequency domain, to combs that usually have multiple-FSR spacing between their adjacent teeth. Solitons, on the other hand, are coherent combs with single-FSR spacing. Experimental and theoretical studies have suggested that solitons are not accessible from the CW intra-cavity field without seeding [73, 74], changing the pump frequency or

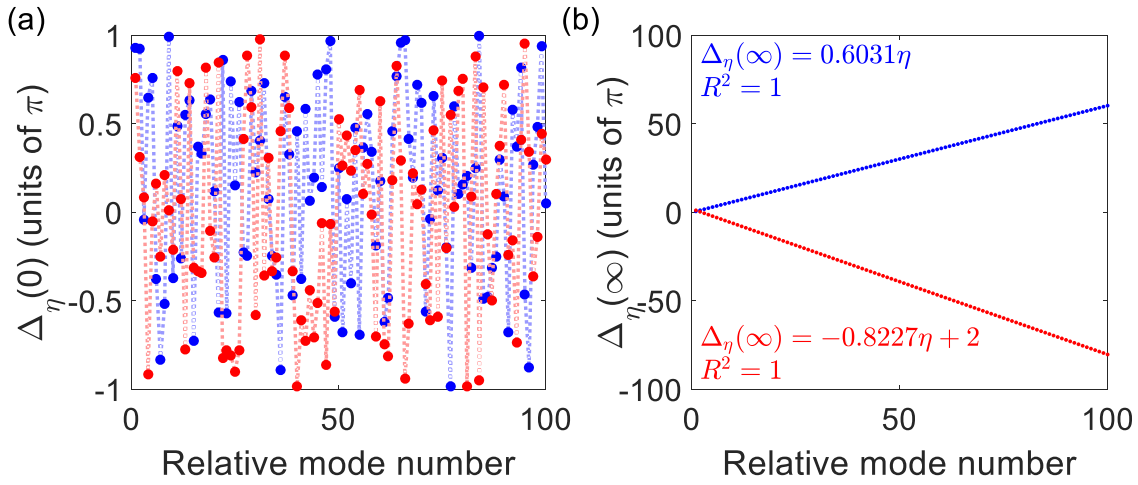

Fig. 3.3.1: Numerical solutions of Eq. (3.3.6). (a) Two examples of the phase differences (PDs) at the onset of integration (initial conditions). These initial PDs have uniform probability density over $(-\pi, \pi]$. (b) Steady-state PDs for the initial conditions shown in (a). It is seen that the final PDs lie on straight lines irrespective of the initial conditions, but different initial values lead to different slopes for these lines. The blue (red) line corresponds to the blue (red) initial values shown in (a). We verify the linearity of the final PDs through fitting a straight line to them (equations on the plot) and calculating the coefficient of determination (R-squared). $R^2 = 1$ shows that the PDs do indeed lie on straight lines.

power [54, 91, 94, 95], or a suitable input pulse [96]. In the model introduced here, we treat solitons and rolls in a unified manner. For solitons, $\eta \in \{0, \pm 1, \ldots, \pm N\}$ while for rolls $\eta \in \{0, \pm\mu, \pm 2\mu, \ldots, \pm N\mu\}$, where N is a positive integer and the integer $\mu \geq 1$ is the mode number at which MI gain peaks (the first pump sidebands are generated) [77, 81].

Experiments and numerical simulations suggest that for stable solutions, the power of the pumped mode is much larger than the other modes (the strong pumping regime) and that in the absence of third- and higher-order dispersion, the power spectrum of these solutions is symmetric with respect to the pumped mode [37, 54, 77] (see, e.g., the inset curves a_η^2 vs. mode number in Fig. 3.4.1). Therefore, we exploit the symmetry of the power spectrum, adopt a perturbative approach (with a_η for $\eta \neq 0$ as the small parameters), and retain terms with at least one contribution from the pumped mode a_0 in the triple summations in Eq. (3.3.2). Equations of motion for the magnitudes a_η and phases ϕ_η can readily be found by using $\tilde{a}_\eta = a_\eta \exp(\mathrm{i}\phi_\eta)$ in

the resulting truncated equations, dividing by $\exp(\mathrm{i}\phi_\eta)$, and separating the real and imaginary parts (see Section 3.8.1 for details). Our approach follows that of Ref. [66], with the generalization that here the comb teeth magnitudes are not required to be equal.

The magnitude and phase equations for the pumped mode include no linear contributions from $a_{\eta\neq 0}$ and read

$$\frac{\mathrm{d}}{\mathrm{d}\tau}\ln(a_0) = \frac{F_\mathrm{P}}{a_0}\cos(\phi_\mathrm{P}-\phi_0) - 1, \tag{3.3.3a}$$

$$\dot{\phi}_0 = \frac{F_\mathrm{P}}{a_0}\sin(\phi_\mathrm{P}-\phi_0) - \alpha + a_0^2. \tag{3.3.3b}$$

The solutions settle on a fast time scale to the equilibrium intra-cavity field $\psi_\mathrm{e} = a_0\exp(\mathrm{i}\phi_0)$ [85]; subsequently, a_0 and ϕ_0 can be treated as constants to first order in $a_{\eta\neq 0}$.

Equations of motion for the centered phase averages $\zeta_\eta = \bar{\phi}_\eta - \phi_0$, where the phase average $\bar{\phi}_\eta = (\phi_\eta + \phi_{-\eta})/2$ is centered to the pumped mode phase ϕ_0, can be found using the phase equations for $\phi_{-\eta}$, $\phi_{+\eta}$, and ϕ_0. This equation, to lowest non-zero order in $a_{\eta\neq 0}$, takes the form

$$\frac{\mathrm{d}}{\mathrm{d}\tau}\zeta_\eta = \frac{1}{2}d_2\eta^2 + a_0^2[1+\cos(2\zeta_\eta)] - \frac{F_\mathrm{P}}{a_0}\sin(\phi_\mathrm{P}-\phi_0), \tag{3.3.4}$$

and can be integrated directly to give

$$\tan\zeta_\eta = \sqrt{\left|\frac{C+2}{C}\right|}\tanh[\sqrt{|C(C+2)|}a_0^2(\tau-\tau_0)]. \tag{3.3.5}$$

Here $C = d_2\eta^2/2a_0^2 - F_\mathrm{P}\sin(\phi_\mathrm{P}-\phi_0)/a_0^3$, and τ_0 accounts for constants of integration (or initial conditions). Equation (3.3.5) holds when $|2a_0^2 - \alpha + d_2\eta^2/2| < a_0^2$, a condition that is automatically satisfied when MI gain exists (see Section 3.8.1). Because the hyperbolic function approaches unity as $\tau\to\infty$, $\bar{\phi}_\eta$ reaches the same constant irrespective of the initial conditions. Since $\bar{\phi}_\eta$ is fixed, each pair of phases $\phi_{\pm\eta}$ must take values symmetrically located relative to the constant average. We will

refer to this as phase "*anti-symmetrization*", following the terminology of [66]. Once established, phase anti-symmetrization means each centered phase average ζ_η can be treated as a constant to first order in $a_{\eta\neq 0}$.

The equations of motion for the phase differences (PDs) defined by $\Delta_\eta = (\phi_\eta - \phi_{-\eta})/2$,

$$\frac{\mathrm{d}\Delta_\eta}{\mathrm{d}\tau} = a_0 \sum\nolimits_l K(l,\eta)\sin(\Delta_l + \Delta_{\eta-l} - \Delta_\eta), \tag{3.3.6}$$

are found by combining the phase dynamics equations for each $\pm\eta$ mode pair (see Section 3.8.1). Here, $K(l,\eta) = a_\eta^{-1} a_l a_{\eta-l}\{2\sin(\zeta_\eta - \zeta_{\eta-l} + \zeta_l) + \sin(\zeta_\eta - \zeta_{\eta-l} - \zeta_l)\}$ is the coupling coefficient for the pump–non-degenerate interaction of comb teeth labeled 0, l, $\eta - l$, and η. Equation (3.3.6) shows that the particular value of the pumped mode power a_0^2 only amounts to a re-scaling of time. This set of equations is the model which governs the long time evolution of the system, and in particular whether or not it displays spatiotemporal pulse formation. On the one hand, it is a *phase model*, and in this sense is a member of a familiar family of models, like the Adler equation [86] or the Kuramoto model [97], used to study spontaneous synchronization. On the other hand, Eq.(3.3.6) is unfamiliar, involving ternary phase interactions rather than binary ones. In the remainder of this paper, we will study solutions of this reduced phase model, compare them with solutions of the LLE, and analyze their stability.

3.4 Reduced Equation Fixed Points

It can readily be verified, through direct substitution, that a family of fixed point solutions of Eq. (3.3.6) is $\Delta_\eta = s_0\eta + k\pi$, where s_0 is an arbitrary constant and k is an integer. These solutions imply that the phases have aligned: the slope of the line passing through the phases of any pair of comb teeth η and $-\eta$ will be the same and equal to s_0, i.e., $(\phi_\eta - \phi_{-\eta})/2\eta = s_0$.

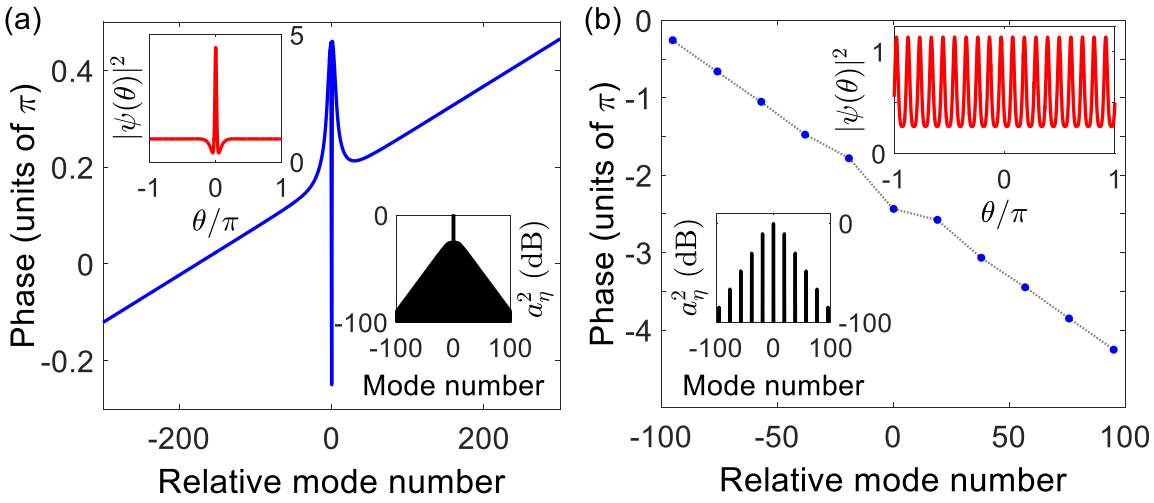

Fig. 3.4.1: Phase alignment in (a) solitons and (b) Turing rolls in the steady-state solutions of Eqs. (3.3.1) and (3.3.2). The inset curves in red (top corners) show the spatiotemporal waveforms and those in black (bottom corners) are the frequency spectra. For both solitons and rolls the phases lie on straights lines of arbitrary slope (see Fig. 3.3.1). Parameter values are (a) $\alpha = 2$, $d_2 = -0.0124$, $F = 1.41$, and (b) $\alpha = 0$, $d_2 = -0.0124$, $F = 1.63$. The phase profile has been unwrapped in (b).

Numerical integration of Eq. (3.3.6) confirms the existence of the family of solutions found analytically. Our numerous runs of numerical integration, for different comb spans (N from 3 to 1000) with random initial PDs taken from a uniform distribution over $(-\pi, \pi]$ always lead to PDs lying on straight lines. The slope of the line depends on the initial conditions. In Fig. 3.3.1, we show two examples (in blue and red) for a comb with 201 teeth and with two different sets of initial conditions. Figure 3.3.1(a) shows the initial conditions while Fig. 3.3.1(b) depicts the steady-state PDs at the end of the simulation time vs. mode number. The results shown in Fig. 3.3.1 are for a triangular power spectrum given by $a_\eta \propto \exp(-k_0|\eta|)$, with $k_0 = 0.05$. This profile assumes a linear decay (in logarithmic scale) of the comb teeth power spectrum [98] with slope $\propto -20k_0$ dB per increasing mode number by unity, (see, e.g., the insets a_η^2 vs. mode number in Fig. 3.4.1). We found that the model is robust and addition of static randomness of modest relative size to the power spectrum and coupling coefficients $K(l, \eta)$ will still lead to aligned PDs. Also, through numerical integration of Eq. (3.3.6), we found that phase alignment occurs

for a variety of power spectrum profiles so long as the powers of the sidebands are smaller than the pumped mode power. Additionally, we observe that specific features like cusp points or isolated sharp peaks in the power spectrum envelope lead to step-like signatures in the distribution of the steady-state PDs; this effect is a topic of ongoing investigations and will be reported elsewhere.

The phase alignment predicted by the reduced phase model of Eq. (3.3.6) is observed in the phase-locked solutions of the LLE. Figure 3.4.1 shows two examples, in solitons and Turing rolls, where Eq. (3.3.1) has been integrated numerically using the split-step Fourier transform method for a typical microresonator. In practice, the random initial phases arise from vacuum fluctuations that seed modulation instability or from the passage of the system through the chaotic state while changing the pump laser power or frequency. We note that the phase offset between the pumped mode and the rest of the phases emerges to counter dissipation [66, 92].

3.5 Stability of the Fixed Points

Next, we consider the linear stability of the solutions of Eq. (3.3.6). For simplicity, we take $k = 0$. (Stability analysis for $k \neq 0$ follows in a similar way.) We consider a frequency comb with $2N + 1$ phase-locked teeth and temporarily ignore the dependence of the comb teeth magnitudes on mode number, i.e., take $a_{\eta \neq 0} = a \ll a_0$. (The effect of the mode number dependence will be included shortly.) After phase locking, the centered phase averages ζ_η reach a steady-state value independent of mode number η (since the phases ϕ_η lie on a straight line). Therefore, the coupling coefficients are all equal, i.e., $K(l, \eta) = K > 0$. Setting $\Delta_\eta = s_0\eta + \epsilon_\eta$, we linearize Eq. (3.3.6) to get $\dot{\boldsymbol{\epsilon}} = \mathbf{J} \cdot \boldsymbol{\epsilon}$, where $\boldsymbol{\epsilon} = (\epsilon_1, \epsilon_2, \ldots, \epsilon_N)^{\mathrm{T}}$, and the Jacobian $\mathbf{J}$ and its eigenvalues can be expressed in closed form for any N (see Section 3.8.2). Except for one zero

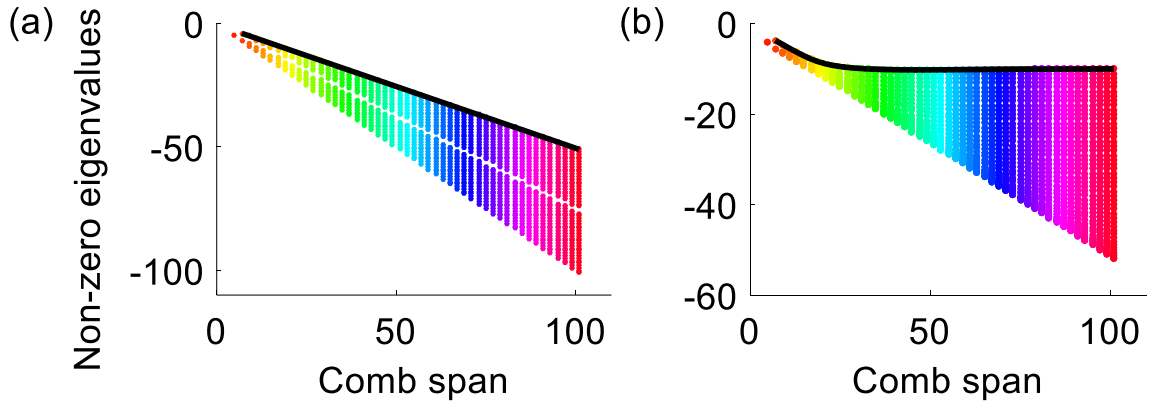

Fig. 3.5.1: Non-zero eigenvalues of the equilibrium (the Jacobian matrix $\mathbf{J}$) vs. comb span for Eq. (3.3.6) for (a) uniform and (b) mode-number–dependent comb teeth magnitude profile of $a_\eta \propto \exp(-k_0|\eta|)$, ($k_0 = 0.1$). The N distinct eigenvalues for each comb span are plotted with points of the same color excepting the negative eigenvalue of smallest magnitude, which is shown in black. The closest eigenvalues to zero for different spans form the black curves. Because these eigenvalues are dominant in determining stability, the black curves show that as the comb widens its stability improves for constant power spectrum, as seen in (a). For the realistic magnitude profile, on the other hand, the stability is not expected to improve, as is shown in (b). The stability of a steady-state solution of the LLE is, therefore, affected by its power spectrum profile. The effect of amplitudes can be taken into account through the coupling coefficients in Eq. (3.3.6).

eigenvalue, all of the eigenvalues are negative and real, indicating asymptotic stability of the synchronized state. The zero eigenvalue is forced by the rotational symmetry of the LLE. In other words, the choice of origin for the azimuthal angle θ is arbitrary and leads merely to an added linear phase. This confirms the physical intuition that the slope of the phase profile of a soliton or Turing roll, determined by random initial conditions, is indeed arbitrary. Figure 3.5.1(a) shows the non-zero eigenvalues of the equilibrium for increasing comb span for the case of uniform sideband power profile. It is seen that the eigenvalue closest to zero (black curve) grows more negative with increasing comb span. The stability of the fixed points for each comb span is determined by the negative eigenvalue of smallest size. Hence, for the case of constant comb amplitudes, a wider comb is expected to demonstrate superior stability.

The model introduced in Eq. (3.3.6) allows the comparison of the stability prop-

erties of frequency combs with different power spectra. Because the coupling coefficients $K(l,\eta)$ depend on the comb teeth magnitudes, the power spectrum profile of a steady-state solution is expected to influence its stabiity. To investigate the effect of a non-constant comb power spectrum, we use a triangular power spectrum given by $a_\eta \propto \exp(-k_0|\eta|)$. Though not analytically tractable, we find numerically that the eigenvalues of $\mathbf{J}$ all have negative real part (except for the single zero eigenvalue forced by symmetry). Figure 3.5.1(b) shows the eigenvalue spectrum vs. increasing comb span for the triangular power spectrum. Note that as the comb span increases, the smallest magnitude eigenvalue becomes bounded and almost independent of N (black curve in Fig. 3.5.1(b)). Therefore, the stability of the comb does not improve—nor does it degrade—with increasing comb span when the natural mode number dependence of the comb teeth magnitudes is taken into account. Pfeifle *et al.* [51] showed that in the presence of pump magnitude and frequency noise, solitons are less robust than Turing rolls in the same microresonator with comparable pump powers. Our results suggest that the superior stability of Turing rolls does not originate from their smaller number of comb teeth compared to solitons. Rather, it is linked to the presence of MI gain, which is responsible for the generation of Turing rolls from vacuum fluctuations. We note that Eq. (3.3.6) does not explicitly include the effect of MI gain; this influence is reflected through the coupling coefficients $K(l,\eta)$.

3.6 Discussion

The existence of a self-synchronization mechanism explains soliton generation by both through-chaos [54, 94, 99] and chaos-avoiding [95] trajectories in the power-detuning plane. In either case, the parameter sweep creates a comb with single-FSR spacing.

Sweeping through chaotic states provides a diverse pool of initial conditions which increases the odds of achieving phase-locked clusters (i.e., peaks) that subsequently grow into solitons; however, even without passing through chaos, the self-synchronization mechanism can generate solitons. It is worth noting that while we have focused on the phase-locked solutions of the LLE, this equation displays chaotic behavoir as well [70, 77]. Bifurcation to chaos in the reduced model of Eq. (3.3.6) can be understood through randomly oscillating coupling coefficients. While the model is robust and addition of static randomness of modest relative size to the coupling coefficients $K(l, \eta)$ will still lead to aligned PDs, our numerical simulations show that rapid random fluctuations of the comb teeth amplitudes (and therefore the coupling coefficients) hinder convergence of the phases toward a fixed point of the system. As a result, the phases will continue to wonder chaotically around without reaching a steady-state. Studying the behavior of this model in the presence of noise is an ongoing work and will be discussed elsewhere.

Phase measurements of stable optical frequency combs have shown that apart from combs with aligned phases (Fig. 3.4.1), phase spectra with π and $\pi/2$ jumps can also arise in microcombs [40]. We note that phase alignment governed by the reduced model is not contradictory to these phase jumps; combs with phase jumps have been constructed numerically as a sum of multiple solutions of the LLE (e.g., interleaved combs [40] or solitons on an equally-spaced grid around the resonator with one solition removed or slightly shifted away from its location on the equidistant grid points [100]) and their power spectra are more complicated than the smooth spectra of a Turing roll or soliton (as depicted in the insets in Fig. 3.4.1) considered in this work. It has been noted that avoided mode crossings [34] far from the pump are necessary for the experimental demonstration (through tuning the CW pump laser) and stabilization of such combs [100]. In Section 3.7, I provide a simple explanation of π jumps in the phase spectrum of optical frequency combs.

3.7 Explanation of jumps in frequency comb phase spectrum measurements

To explain the phase jumps which have been observed in optical frequency comb phase measurements, I will resort to a simple high school problem in vector algebra or Newtonian mechanics[2]. Consider the free-body diagram shown in Fig. (3.7.1), where N forces of equal magnitude $F_1, F_2, F_3, \cdots, F_N$ (black vectors) are applied to an object of mass m (blue box). Each of these force vectors makes an angle $2\pi/N$ with the previous one. As such, the force vectors make a closed convex polygon with N edges and add up to zero so that the net force on the box is zero,

$$\sum_{n=1}^{N} \vec{F}_n = 0.$$

Now imagine that one of these forces, say F_k is removed. What is the acceleration vector of the object in this new configuration of forces? The net force on the object has a magnitude equal to the removed force and is in the direction opposite to it, because

$$\sum_{\substack{n=1 \\ (n\neq k)}}^{N} \vec{F}_n = -\vec{F}_k + \sum_{n=1}^{N} \vec{F}_n = -\vec{F}_k.$$

Hence, the object will have an acceleration equal of $\vec{a} = -\vec{F}_k/m$. The relationship of this problem to phase jumps in OFC phase spectra will become clear momentarily.

Consider N solitons residing on an equidistant grid around the resonator circumference. Figure 3.7.2 shows an example for $N = 10$. Since the phase spectrum of each of the solitons is a simple straight line (ignoring the phase offset of the pumped mode, which is insignificant in this case), we can think of all of the comb teeth for a single soliton as one "object". Replace the forces $\vec{F}_n$ in the preceding discussion with

[2]I saw this problem first in first or second grade in high school when I was preparing for level I of the Iranian National Physics Olympiad for high school students.

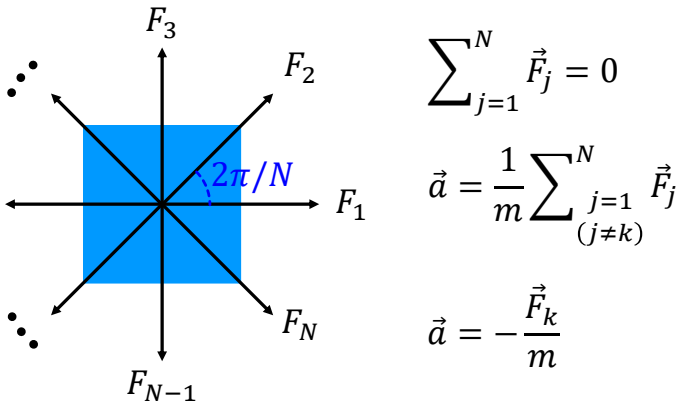

Fig. 3.7.1: Simple vector addition problem used to explain π phase jumps in optical frequency combs. Left: N forces of equal magnitude $F_1, F_2, F_3, \cdots, F_N$ (black vectors) are exerted on an object of mass m (blue box). Each of the force vectors makes an angle $2\pi/N$ with the previous one (the force vectors make a closed convex polygon with N edges). One of these forces, say F_k is removed. Find the acceleration vector of the object. Right: Solution to the problem. The net force on the object is equal to the removed force but in the direction opposite to it.

a soliton spectrum

$$\vec{F}_n \rightarrow \psi(\theta - \theta_n) = \sum_{\eta} \tilde{a}_\eta \exp[\mathrm{i}\eta(\theta - \theta_n)], \tag{3.7.1}$$

where

$$\theta_n = (n-1)\frac{2\pi}{N}.$$

The time dependence of the comb teeth complex amplitudes $\tilde{a}_\eta(\tau)$ can be ignored, as we are interested in steady-state solitons. The total field envelope is

$$\psi(\theta) = \sum_{n=1}^{N} \psi(\theta - \theta_n) = \sum_{\eta} \tilde{a}_\eta \sum_{n=1}^{N} \exp[\mathrm{i}\eta(\theta - \theta_n)]. \tag{3.7.2}$$

Recalling our auxiliary problem (Fig. 3.7.1), one notes that the second summation above,

$$\sum_{n=1}^{N} \mathrm{e}^{\mathrm{i}\eta(\theta - \theta_n)}$$

is zero for all values of the mode number η unless it is an integer multiple of N, i.e., $\eta = jN$ for an integer j. As a result, the frequency spectrum of a "complete" lattice of N solitons around a resonator consists of comb teeth separated by N FSR's.

Figures 3.7.2 (a) and (b) show an example. (The spectrum is the same as a Turing roll, however I had to drag the reader along to make the final step of the argument below more plausible.)

Now, if one of the solitons on the grid described above is removed, the overall field envelope is

$$\psi(\theta) = \sum_{\substack{n=1 \\ (n\neq k)}}^{N} \psi(\theta - \theta_n) = -\psi(\theta - \theta_k) + \sum_{n=1}^{N} \psi(\theta - \theta_n) = \mathrm{e}^{\mathrm{i}\pi}\psi(\theta - \theta_k) + \sum_{n=1}^{N} \psi(\theta - \theta_n). \tag{3.7.3}$$

The above expression describes a comb comprising of two parts: one is the Turing-like spectrum described earlier, and the other is a single soliton spectrum. The latter is out of phase by π with respect to the former. An example of this case can be seen in Figs. 3.7.2(c), (d) and (e). The spectrum of a single soliton is shown with a dashed black line in panel (c) in this figure.

It is worth noting that the "defective" lattice shown in Fig. 3.7.2(c, d) is not stable and the solitons will move with time till they adjust their mutual distances and make a complete lattice with $2\pi/(N-1)$ spacing around the resonator circumference, as depicted in Fig. 3.7.2(f). This position re-adjustment of solitons originates from a repulsive force between them and can be compensated by mode crossings, as noted at the end of the previous section. While soliton interaction has been extensively studied in fiber-based optical systems [101], it is still an open problem in microcombs. Part of the difficulty arises from the interaction of the sharp peaks (solitons) with the CW background.

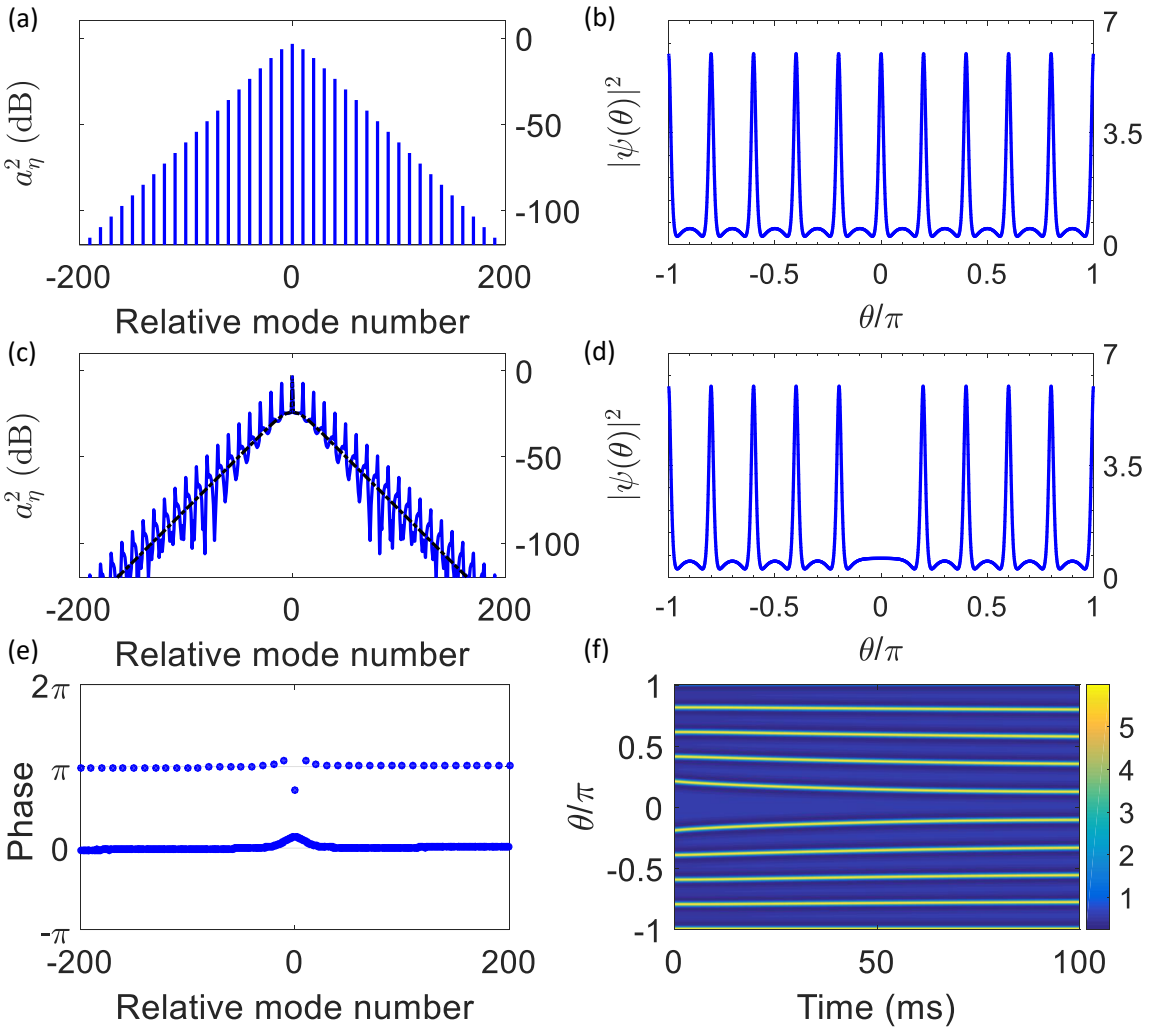

Fig. 3.7.2: Frequency combs with π phase jumps and soliton repulsion. (a, b) A "complete" lattice of dissipative cavity solitons positioned equidistantly around the the resonator circumference. The power spectrum (left) consists of comb teeth separated by the number of peaks (right) times FSR, same as the power spectrum of a Turing roll. (c, d) If one of the solitons is removed, the power spectrum will consist of that shown in (a) plus the power spectrum of a single soliton (dashed black curve). (e) Each comb teeth in the latter, however, has a phase difference equal to π from the comb teeth with multiple-FSR spacing; see Eq. (3.7.3). (f) The "defective" lattice shown in (d) is not stable; the solitons will move with time till they adjust their mutual distances and make yet another complete lattice with equal spacing around the resonator circumference.

3.8 Mathematical details of the derivation and stability of the reduced phase model

3.8.1 Derivations

To avoid distracting the reader with too much mathematical details, the presentation of the phase locking model in the foregoing sections of this chapter overlooked some of the less important derivations. This section details the derivations leading to the equations in Sec. (3.3).

The intra-cavity spatiotemporal field envelope $\psi(\theta,\tau)$ and the complex-valued comb teeth amplitudes $\tilde{a}_\eta$, $\eta \in \{0, \pm1, \pm2, \pm3, \dots\}$, are discrete-time Fourier transform pairs related through the following equations

$$\psi(\theta,\tau) = \sum_{\eta=-\infty}^{\infty} \tilde{a}_\eta(\tau)\, \mathrm{e}^{+\mathrm{i}\eta\theta}, \tag{3.8.1}$$

and

$$\tilde{a}_\eta(\tau) = \frac{1}{2\pi}\int_{-\pi}^{\pi} \mathrm{d}\theta\, \psi(\theta,\tau)\, \mathrm{e}^{-\mathrm{i}\eta\theta}. \tag{3.8.2}$$

The summation in Eq. (3.8.1) is truncated and ∞ is replaced by the positive integer N [79]. Using these equations and exploiting $\int_{-\pi}^{\pi} \mathrm{d}\theta\, \exp[\mathrm{i}(\eta-\eta')\theta] = 2\pi\delta_{\eta\eta'}$, it is straightforward to find the equivalent coupled nonlinear ordinary differential equations of Eq. (3.3.2) from the LLE. In the strong pumping regime and considering the symmetry of the power spectrum, and after using $\tilde{a}_\eta = a_\eta \exp(\mathrm{i}\phi_\eta)$ in the nonlinear ODEs, the equations for the magnitudes a_η and phases ϕ_η can be separated to yield

$$\begin{aligned}\frac{\mathrm{d}}{\mathrm{d}\tau}\ln(a_\eta) = -1 + \frac{a_{-\eta}}{a_\eta}a_0^2\sin(\phi_\eta+\phi_{-\eta}-2\phi_0) + \frac{F_\mathrm{P}}{a_\eta}\cos(\phi_\mathrm{P}-\phi_\eta)\delta_{0\eta} \\ - \frac{a_0}{a_\eta}\sum_l a_l\{2a_{\eta+l}\sin(\phi_0-\phi_l+\phi_{\eta+l}-\phi_\eta) + a_{\eta-l}\sin(\phi_l-\phi_0+\phi_{\eta-l}-\phi_\eta)\},\end{aligned} \tag{3.8.3}$$

$$\begin{aligned}\frac{\mathrm{d}}{\mathrm{d}\tau}\phi_\eta = 2a_0^2 - \alpha + \frac{1}{2}d_2\eta^2 + \frac{a_{-\eta}}{a_\eta}a_0^2\cos(2\phi_0-\phi_\eta-\phi_{-\eta}) + \frac{F_\mathrm{P}}{a_\eta}\sin(\phi_\mathrm{P}-\phi_\eta)\delta_{0\eta} \\ + \frac{a_0}{a_\eta}\sum_l a_l\{2a_{\eta+l}\cos(\phi_0-\phi_l+\phi_{\eta+l}-\phi_\eta) + a_{\eta-l}\cos(\phi_l-\phi_0+\phi_{\eta-l}-\phi_\eta)\}.\end{aligned} \tag{3.8.4}$$

Using Eq. (3.8.4), the equations of motion for the centered phase averages $\zeta_\eta = (\phi_\eta + \phi_{-\eta})/2 - \phi_0$ and phase differences $\Delta_\eta = (\phi_\eta - \phi_{-\eta})/2$ can be found,

$$\frac{\mathrm{d}}{\mathrm{d}\tau}\zeta_\eta = \frac{1}{2}d_2\eta^2 + a_0^2[1+\cos(2\zeta_\eta)] - \frac{F_\mathrm{P}}{a_\eta}\sin(\phi_\mathrm{P}-\phi_\eta)\delta_{0\eta} \tag{3.8.5}$$
$$+ \frac{a_0}{a_\eta}\sum_l a_l a_{\eta-l}\cos(\Delta_l+\Delta_{\eta-l}-\Delta_\eta)\{2\cos(\zeta_{\eta-l}-\zeta_\eta-\zeta_l)+\cos(\zeta_{\eta-l}-\zeta_\eta+\zeta_l)\},$$

$$\frac{\mathrm{d}}{\mathrm{d}\tau}\Delta_\eta = \frac{a_0}{a_\eta}\sum_l a_l a_{\eta-l}\{2\sin(\zeta_{\eta-l}-\zeta_\eta-\zeta_l)+\sin(\zeta_{\eta-l}-\zeta_\eta+\zeta_l)\}\sin(\Delta_l+\Delta_{\eta-l}-\Delta_\eta). \tag{3.8.6}$$

Equations (3.8.3, 3.8.4) for $\eta = 0$ lead to Eq. (3.3.3a, 3.3.3b) of the main text, and Eq. (3.8.6) is the same as Eq. (3.3.6) in the main text, where the coupling coefficient $K(l,\eta)$ was defined. We note that the normalized chromatic dispersion coefficient d_2 is defined by $d_2 = -2D_2/\Delta\omega_0$, where $\Delta\omega_0$ is the linewidth of the pumped mode and D_2 is the second-order dispersion parameter found from the Taylor expansion of the cavity modal frequencies ω_η in the mode number η at the pumped mode ω_0 through $\omega_\eta = \omega_0 + D_1\eta + \frac{1}{2!}D_2\eta^2 + \frac{1}{3!}D_3\eta^3 + \dots$. In the latter expression, D_1 is the resonator FSR (in rad/s) at the pumped mode.

To lowest non-zero order in $a_{\eta\neq 0}$, Eq. (3.8.5) becomes Eq. (3.3.4). This equation is separable, i.e.,

$$\int_{\zeta_\eta(\tau_0)}^{\zeta_\eta(\tau)} \frac{\mathrm{d}\zeta_\eta}{1+C(\eta)+\cos(2\zeta_\eta)} = a_0^2\int_{\tau_0}^{\tau}\mathrm{d}\tau',$$

and can be integrated directly to give

$$\frac{1}{\sqrt{C(C+2)}}\tan^{-1}\left[\sqrt{\frac{C}{C+2}}\tan(\zeta_\eta)\right]_{\zeta_\eta(\tau_0)}^{\zeta_\eta(\tau)} = a_0^2(\tau-\tau_0). \tag{3.8.7}$$

In these equations $C = d_2\eta^2/2a_0^2 - F_\mathrm{P}\sin(\phi_\mathrm{P}-\phi_0)/a_0^3$, and τ_0 accounts for constants of integration (or initial conditions). The latter equality can be written as

$$\tan[\zeta_\eta(\tau)] = \sqrt{\frac{C+2}{C}}\tan[\sqrt{C(C+2)}a_0^2(\tau-\tau_0')], \tag{3.8.8}$$

where τ_0' accounts for the constants of integration on both sides of Eq. (3.8.7). The parameter C appears in two combinations, $C/(C+2)$ and $C(C+2)$; if $-2 < C < 0$, then both expressions will be negative and the tangent on the right of Eq. (3.8.8) changes to a hyperbolic tangent. Therefore, one arrives at Eq. (3.3.5) in the main text.

It is straightforward to show that the gain of modulation instability (MI) for the LLE of Eq. (3.3.1) is given by [77, 81]

$$\Gamma = \mathrm{Re}\left\{-1 + \sqrt{a_0^4 - \left(\alpha - \frac{1}{2}d_2\eta^2 - 2a_0^2\right)^2}\right\},$$

where $\mathrm{Re}\{\cdot\}$ denotes real part. For this expression to be positive, the following inequality should hold

$$a_0^4 - 1 \geq \left(\alpha - \frac{1}{2}d_2\eta^2 - 2a_0^2\right)^2 \geq 0. \tag{3.8.9}$$

It can simply be shown that the condition $-2 < C < 0$ on C is equivalent to $a_0^2 \geq |\alpha - d_2\eta^2/2 - 2a_0^2|$, which is guaranteed to hold in the presence of MI gain, cf. Eq. (3.8.9).

3.8.2 Linear stability analysis

In this section, I review the stability analysis of the reduced phase model and introduce the generic form of the Jacobian matrix $\mathbf{J}$ and its eigenvalues for the case of uniform comb amplitudes. Previously, only the results of this analysis were presented.

Let's consider Eq. (3.3.6) in the main text for a comb with $2N+1$ phase-locked teeth. For all the indices appearing in this equation to be in the range $[-N, N]$, the summation should run from $-(N-\eta)$ to N, i.e.,

$$\frac{\mathrm{d}\Delta_\eta}{\mathrm{d}\tau} = a_0 \sum\nolimits_{l=-(N-\eta)}^{N} K(l,\eta)\sin(\Delta_l + \Delta_{\eta-l} - \Delta_\eta).$$

As explained in the main text, the coupling coefficients K will be the same for uniform comb magnitude spectrum (where $a_{\eta\neq 0} = a \ll a_0$). If each phase ϕ_η is perturbed from

its steady-state value by e_η, the phase difference $\Delta_\eta = s_0\eta$ will change to $s_0\eta + \epsilon_\eta$, where $\epsilon_\eta = (e_\eta - e_{-\eta})/2$. Plugging into the above equation (Eq. (3.3.6) of the main text) and linearizing in ϵ_η, we find the matrix equation $\dot{\boldsymbol{\epsilon}} = \mathbf{J}\cdot\boldsymbol{\epsilon}$, for the perturbation vector $\boldsymbol{\epsilon} = (\epsilon_1, \epsilon_2, \ldots, \epsilon_N)^{\mathrm{T}}$. For $a_{\eta\neq 0} = a \ll a_0$, the Jacobian $\mathbf{J}$ and its eigenvalues can be expressed in closed form for any integer N. For N an odd integer $\mathbf{J}$ equals

$$\begin{bmatrix}
-2N & 0 & \ldots & 0 & 0 & 0 & \ldots & 0 & 2 \\
0 & -2N+1 & \ldots & \vdots & \vdots & \vdots & \ldots & 2 & 2 \\
0 & 0 & \ldots & 0 & 0 & 0 & \ldots & 2 & 2 \\
0 & 0 & \ldots & -2N-1+\lfloor N/2\rfloor & 0 & 2 & \ldots & 2 & 2 \\
\vdots & \vdots & \ldots & 0 & -N+1-\lfloor N/2\rfloor & 2 & \ldots & \vdots & \vdots \\
0 & 0 & \ldots & 2 & 2 & -N+2-\lfloor N/2\rfloor & \ldots & 2 & 2 \\
0 & 0 & \ldots & 2 & 2 & 2 & \ldots & 2 & 2 \\
0 & 2 & \ldots & \vdots & \vdots & \vdots & \ldots & -N & 2 \\
2 & 2 & \ldots & 2 & 2 & 2 & \ldots & 2 & -N+1
\end{bmatrix},$$

and its eigenvalues are $0, -N-1, -N-2, \ldots, -N+1-\lfloor N/2\rfloor, -N-\lfloor N/2\rfloor, -2N-2+\lfloor N/2\rfloor, -2N-3+\lfloor N/2\rfloor, \ldots, -2N, -2N-1$ (where $\lfloor\cdot\rfloor$ is the floor function). For even N, the Jacobian takes the following form

$$\mathbf{J} = \begin{bmatrix}
-2N & 0 & \ldots & 0 & 0 & \ldots & 0 & 2 \\
0 & -2N+1 & \ldots & \vdots & \vdots & \ldots & 2 & 2 \\
0 & 0 & \ldots & 0 & 0 & \ldots & 2 & 2 \\
\vdots & \vdots & \ldots & -2N-1+N/2 & 2 & \ldots & \vdots & \vdots \\
0 & 0 & \ldots & 2 & -N+2-N/2 & \ldots & 2 & 2 \\
0 & 0 & \ldots & 2 & 2 & \ldots & 2 & 2 \\
0 & 2 & \ldots & \vdots & \vdots & \ldots & -N & 2 \\
2 & 2 & \ldots & 2 & 2 & \ldots & 2 & -N+1
\end{bmatrix}.$$

The eigenvalues of this matrix are $0, -N-1, -N-2, \ldots, -N+2-N/2, -N+1-N/2, -2N-2+N/2, -2N-3+N/2, \ldots, -2N, -2N-1$. It is noted that there will always be a zero eigenvalue enforced by symmetry, and all other eigenvalues are

negative. The negative eigenvalue of smallest size $(-N-1)$ determines the stability of the fixed points. These eigenvalues for different comb spans $(2N+1)$ are plotted in black in Fig. 3.5.1(a).

3.9 Summary and Outlook

In summary, we have introduced a model for phase locking and the emergence of coherent spatiotemporal patterns in the damped, driven NLSE. This novel model underscores the fundamental link between spatiotemporal pulse formation and mode synchronization, and embodies the conservation of energy and momentum through ternary phase couplings. We have found attracting solutions of the model corresponding to dissipative solitons and Turing rolls and studied their stability.

Although we have compared our results with micro-resonator-based optical frequency combs, they should apply to mode-locked laser systems as well. Gordon and Fisher's statistical mechanical theory describes the onset of laser pulsations as a first-order phase transition, treating the modes as the elementary degrees of freedom [102]. Their ordered collective state is analogous to our synchronized dynamical attractor. The same controlling nonlinearity appears in both Eq. (3.3.6) and the master equation for passive mode locking based on a saturable absorber [90], which approximates the absorber with a cubic nonlinearity. (Comparison of Eq. (16) in [90] with the LLE reveals their close similarity. In the LLE, there is an extra detuning term and the gain term is replaced by an external drive. See also Section 1.5.) We therefore expect the same dynamical mechanism to be responsible for the creation of sharp pulses in passively mode-locked lasers, despite different physical sources of optical gain (population inversion and stimulated emission versus parametric amplification). What matters is the fundamental link between spatiotemporal pulse formation and mode synchronization.

CHAPTER 4

SOLITON FORMATION THROUGH PARAMETRIC SEEDING

"Behind it all is surely an idea so simple, so beautiful, that when we grasp it - in a decade, a century, or a millennium - we will all say to each other, how could it have been otherwise? How could we have been so stupid?"

John Archibald Wheeler, "How Come the Quantum?" (1986)

In the foregoing chapters of this thesis, the standard Lugiato-Lefever equation was studied for the generated of phase-locked optical frequency combs, i.e., Turing patterns and solitons. While Turing patterns are more easily accessible and very stable for such applications as microwave generation and optical telecommunication, they are usually not very broadband. Solitons, on the other hand, have robust single-FSR spacing between their comb teeth, their line-to-line spectral power changes smoothly, and are more broadband [54, 103]. Single soliton generation, therefore, is highly desirable from a practical perspective. Although multiple groups now routinely make bright solitons in the lab through tuning the pump laser into resonance, the dependence of the laser pump frequency on time while tuning is still a matter of trial and error. Even after calibration of a sample resonator, single solitons are not generated consistently in successive runs of laser frequency sweep. In this chapter, a novel technique for deterministic soliton formation based on pump phase modulation with a modulation frequency equal to the resonator FSR is proposed and studied. It is shown that phase modulation has two effects. First, it modulates the intra-cavity CW background and generates soliton peaks. Second, it creates a force on the generated peaks which pushes them towards each other, leading to the

merging of the pulses and the generation of a single soliton. It is worth noting that very recently, the phase modulation technique has been implemented experimentally and it has been suggested that the dynamic range of the pump-resonance detuning and modulation depth can be increased by combining phase modulation with laser scan[1] [48].

4.1 Introduction

As noted in Section 2.2.2, the existence of stable localized sub-picosecond temporal pulses in the form of dissipative Kerr solitons was theoretically predicted and experimentally demonstrated [30, 37, 54, 57, 60, 61] using available theoretical models (the nonlinear coupled mode equations and the LLE). Transition from a comb with random phase spectrum to a sharply peaked narrow soliton with phase spectra discussed in Chapter 3, however, has proven to be a delicate task. For instance, the solitons demonstrated in [54] were observed while adiabatically tuning the pump laser into resonance. Further investigations have shown that abrupt changes in the detuning or the pump power could also direct the system towards solitonic attractors, and it has been suggested that the system should necessarily go through a chaotic state before achieving a soliton [94, 99]. To date, however, no systematic method has been proposed for the reliable deterministic generation of phase-locked microcombs. This shortcoming limits applications of temporal solitons outside the lab and signifies a challenge towards their chip-scale realization.

In this chapter, a seeding technique for phase-locked frequency comb generation is discussed. In particular, a scheme for soliton formation based on driving the resonator by a modulated CW laser pump is proposed. In essence, these schemes fall under the general heading of *parametric seeding* which has previously been studied in special

[1] This chapter is based on results presented in [74].

cases [104, 105]. Parametric seeding provides a means of controlling combs and pulses generated in WGM resonators through the introduction of some seed frequencies and manipulating their amplitudes or phases. I start from the coupled nonlinear equations of Eq. 3.3.2 and derive a variant of the LLE which governs frequency comb generation seeded by input modulation. Our numerical simulations of this equation suggest that pump phase modulation provides a deterministic path, without having to walk the system through a chaotic phase by a tailored pump wavelength sweeping ramp, towards soliton formation in WGM resonators. We also show that the modulation can be turned off adiabatically without affecting the generated solitons. Combined with optoelectronic modulators, modulated pump excitation introduces a viable approach towards making the advantages of temporal solitons available at small footprints.

It is worth noting that phase modulation has been used in the context of diffractive and fiber cavities to move pulses, form pulse arrays, and suppress the interaction of solitons in fibers [89, 106–109]. In such studies, a "holding" or "driving beam" is used to balance the cavity dissipation, and a pulsed laser is used to inject a pulse (e.g., a Gaussian pulse from a mode-locked laser) into the cavity. This pulse, upon propagation in the resonator, evolves into a soliton (see, e.g., [96, 106]). A phase modulated "addressing beam" is then used to move the soliton over the holding beam. A soliton in an array formed by phase modulation can be switched off independently using an input pulse with a properly chosen phase difference [106, 107]. We note that the phase-modulation–induced sidebands correspond to a modulation added to the CW background in the intra-cavity field, which can grow into a soliton when it is strong enough to overcome the resonator losses. Thus, with phase modulation, solitons can be formed without going through an unstable state [54, 94, 99] and without an injected pulse [96, 107–109] in a microresonator.

4.2 Seeding by pump phase modulation

In this section, the modified nonlinear coupled ODE's and the corresponding LLE for pump phase modulation are derived. Figure 4.2.1 shows the schematic of the structure under study, where an access waveguide is coupled to a microresonator. We consider exciting the resonator with a CW laser pump with an amplitude proportional to F_0 and with a frequency ω_{P} in the vicinity of a cavity resonance denoted by ω_{j_0}. The resonance frequencies of the resonator, assumed to be the different azimuthal orders of the same radial order mode, are centered with respect to this pumped resonance, i.e., each resonance frequency is written as $\omega_{j_0}+\omega_\eta$ while its mode number is written as $j_0+\eta$, where j_0, as in the previous chapters, is the mode number of the pumped resonance and is an integer. In this notation, $\eta=0$ and $\omega_0=0$ correspond to the pumped (or central) resonance frequency. The nonlinear coupled ODE's describing frequency comb generation, Eq. (2.2.2), can be written in a more generic way as

$$\begin{aligned}\frac{\mathrm{d}A_\eta}{\mathrm{d}t} &= -\frac{\Delta\omega_\eta}{2}A_\eta \\ &\quad - \mathrm{i}g_0\sum_{l,m,n} A_l A_m^* A_n \exp[\mathrm{i}(\omega_l-\omega_m+\omega_n-\omega_\eta)t]\delta_{\eta_{lmn}\eta} \\ &\quad + \frac{\Delta\omega_\eta}{2}\mathcal{F}_\eta, \end{aligned} \tag{4.2.1}$$

where $\eta_{lmn}=l-m+n$. In this equation, instead of assuming that pumping occurs only at one resonance frequency, a general pumping scheme is assumed, in which each resonance η can have its own pump $\mathcal{F}_\eta$. The phase of the input laser is modulated, either off-chip or on-chip, at a frequency ω_{M} and with a modulation depth δ_{M} before coupling into the resonator. The modulation leads to the generation of equidistant sidebands with frequency spacing ω_{M} around the pump [110]. These sidebands, using the notation adopted in Section 2.2.2, can be written as

$$\mathcal{F}_\eta = \mathcal{F}_0\,\mathrm{J}_\eta(\delta_{\mathrm{M}})\exp[\mathrm{i}(\sigma+\eta\omega_{\mathrm{M}}-\omega_\eta)t] \tag{4.2.2}$$

where $\sigma = \omega_{\rm P} - \omega_0$ is, as before, the frequency detuning between the pump and the resonance nearest to it (pumped resonance). The function $\mathrm{J}_\eta(\delta_{\rm M})$ is the Bessel function of the first kind and of order η and represents the amplitude of the η-th sideband of the pump generated through phase modulation. The exponent in Eq. (4.2.2) is the detuning between each modulation-induced sideband frequency $\omega_{\rm P} + \eta\omega_{\rm M}$ and its nearest cavity resonance. Plugging Eq. (4.2.2) into (4.2.1) and following the same procedure as that in Section 2.2.2, we find the equation governing the spatiotemporal evolution of the total field envelope (henceforth also referred to as the waveform), i.e.,

$$\begin{aligned}\frac{\partial A}{\partial t} = &\left(-\frac{\Delta\omega_0}{2} - \mathrm{i}g_0|A|^2 + \sum_{n=1}^{N\geq 2} \mathrm{i}^{n+1}\frac{D_n}{n!}\frac{\partial^n}{\partial\theta^n}\right)A \\ &+ \frac{\Delta\omega_0}{2}\mathcal{F}_0 \mathrm{e}^{\mathrm{i}\sigma t}\sum_\eta \mathrm{J}_\eta(\delta_{\rm M})\mathrm{e}^{\mathrm{i}\eta(\omega_{\rm M}t-\theta)}. \end{aligned} \tag{4.2.3}$$

In arriving at this equation, it has been assumed that the linewidth of all cavity resonances are the same; see Eq. (2.2.12). The last summation on the right-hand-side of Eq. (4.2.3) is recognized as the generating function for the Bessel functions of the first kind [111]. Using the Jacobi-Anger identity,

$$\exp(\mathrm{i}\delta_{\rm M}\sin\theta) = \sum_n \mathrm{J}_n(\delta_{\rm M})\exp(\mathrm{i}n\theta),$$

Eq. (4.2.3) can be cast in the form

$$\begin{aligned}\frac{\partial A}{\partial t} = &\left(-\frac{\Delta\omega_{j_0}}{2} - \mathrm{i}\sigma - \mathrm{i}g_0|A|^2 + (\omega_{\rm M} - D_1)\frac{\partial}{\partial\theta} + \sum_{n=2}^{N\geq 2}\mathrm{i}^{n+1}\frac{D_n}{n!}\frac{\partial^n}{\partial\theta^n}\right)A \\ &+ \frac{\Delta\omega_0}{2}\mathcal{F}_0\exp\left(-\mathrm{i}\delta_{\rm M}\sin\theta\right). \end{aligned} \tag{4.2.4}$$

It is emphasized that, similar to Section 2.2.2, to find this equation I have moved to a rotating reference frame (this time, one with angular velocity equal to the modulation frequency $\omega_{\rm M}$) through $\theta \to \theta + \omega_{\rm M}t$, and have also made the transformation $A \to A\exp(-\mathrm{i}\sigma t)$.

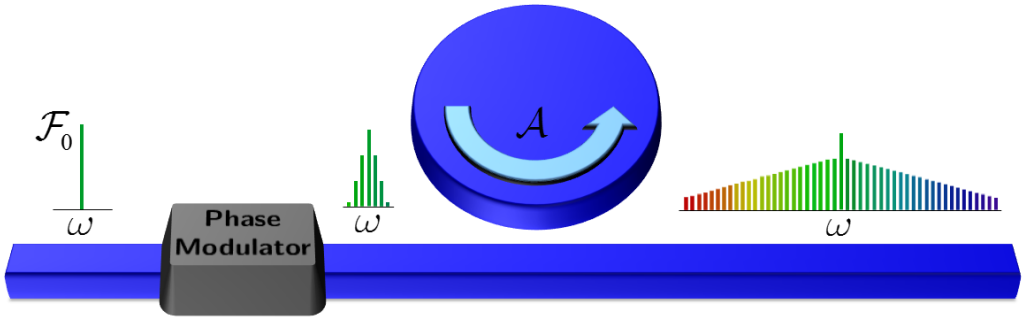

Fig. 4.2.1: Schematic of a resonator driven by a phase-modualted laser pump. A waveguide is side-coupled to a resonator. The phase of the input laser is modulated before it couples into the resonator. The modulation leads to the generation of sidebands which seed the comb generation process. The equipment for stabilizing the pump-resonance detuning is not shown here.

Equation (4.2.4) can be normalized, in the same manner described in Section 2.2.3, to give

$$\frac{\partial\psi}{\partial\tau} = \left[-1 - \mathrm{i}\alpha + \mathrm{i}|\psi|^2 + \left(d_1 - \frac{2\omega_\mathrm{M}}{\Delta\omega_0}\right)\frac{\partial}{\partial\theta} - \sum_{n=2}^{N\geq 2}(-\mathrm{i})^{n+1}\frac{d_n}{n!}\frac{\partial^n}{\partial\theta^n}\right]\psi + F_0\exp[\mathrm{i}\delta_\mathrm{M}\sin(\theta)]. \tag{4.2.5}$$

Here, $\Delta\omega_0 = \omega_{\eta_0}/Q_\mathrm{L}$ is the mode linewidth of the pumped resonance, Q_L being the loaded quality factor at this frequency. All normalized dispersion parameters d_j with $j \geq 3$ will be neglected in the remainder of this chapter, but could be included in the formalism in a straightforward way [94].

As seen in Eq. (4.2.5), the effect of phase modulation at the input port manifests itself as a spatially varying excitation and a first-order spatial derivative of the total field envelope with the modulation frequency as its coefficient. If the input is modulated at $\omega_\mathrm{M} = D_1$, the first-order spatial derivative vanishes and the waveform evolution will be governed by a variant of the "standard" LLE of Eq. (2.2.17) whose derive term is a function of the spatial coordinate. Due to its practical significance, I will mainly focus on this case. Numerical simulations suggest that results presented here hold also for asynchronous pumping if $(\omega_\mathrm{M} - D_1) \ll 1$.

4.3 Soliton formation and manipulation

The split-step Fourier algorithm [112] has been used for our numerical simulations of Eq. (4.2.5). The simulations have been performed for a calcium fluoride (CaF_2) resonator of radius $R = 2.5$ mm which has previously been used in both experimental and theoretical investigations [53, 69]. For this resonator, the linear and nonlinear refractive indices are $n_0 = 1.43$, and $n_2 = 3.2\times10^{-20}$ m^2/W respectively, and effective nonlinear mode volume $V_0 = 6.6 \times 10^{-12}$ m^3. The dispersion coefficients for this resonator are $D_1 = 2\pi \times (13.35$ GHz) and $D_2 = 2\pi \times (400$ Hz). The free-space wavelength of the central resonance is $\lambda_0 = 1560.5$ nm with a corresponding mode number $\eta_0 = 14350$. The loaded quality factor of the cavity at is $Q_{\rm L} = 3 \times 10^9$ with a modal bandwidth of $\Delta\omega_0 = 2\pi \times (64$ kHz).

While the generation of Turing rolls is possible starting from a cold cavity, in a regime of parameters where solitonic fixed points exist, starting from a cold cavity will not necessarily lead to the generation of a soliton, and a particular initial condition (e.g., in the form of a weak pulse) is required [77, 94]. This initial condition can be supplied by sweeping the pump-resonance detuning or changing the input power thereby walking the system through a chaotic state (as in [54, 94, 99]), which can be viewed as providing a pool of different initial conditions. The need for a suitable initial condition poses an obstacle to the realization of stand-alone microresonator-based ultra-short pulse sources. We show here that parametric seeding via the modulation of the input pump phase relaxes this constraint.

Figure 4.3.1 illustrates the generation of a soliton starting from a cold cavity when the pump phase is modulated at a depth corresponding to the transfer of 12% of the pump power to the primary sidebands ($\delta_{\rm M} = 0.75$). As seen in the left panel in Fig. 4.3.1(a), a stable sharply peaked soliton is generated at $\theta = \pi/2$. The spectrum of the pulse is smooth and broadband (Fig. 4.3.1(a), middle panel) and the time

evolution of the phases of the comb lines (right panel) clearly illustrates phase locking, i.e., the establishment of a fixed relationship between the phases of different comb lines, after the soliton is formed. The waveform and frequency spectrum of this pulse (Figs. 4.3.1(b,c), respectively) are essentially identical to those of a soliton generated from a Gaussian pulse as the initial condition. This suggests that parametric seeding by input phase modulation has walked the system towards the same fixed point as that achieved by a particular initial condition. In Fig. 4.3.1(d), a closer look is cast upon the spectra of the pulses generated in the two scenarios in the vicinity of the pumped resonance. The spectrum of the soliton produced by phase modulation (blue curve) and that of the soliton evolved from a suitable non-constant initial condition (red spikes) differ only in the few modal fields close to the pump (taller central spike) and are identical otherwise. The difference between the total field envelopes is much harder to see, such that if we overlay the corresponding curves on top of each other in one figure, they are indistinguishable to the eye.

Results presented in Fig. 4.3.1 assume that the resonator has zero energy at the onset of the input phase modulation. In an experimental setup, however, the precise synchrony of the pump turn-on time and that of the phase modulator might be difficult. To account for this effect, we have shown in Fig. 4.3.2(a) the evolution of the intra-cavity field when the phase modulation is applied to a resonator initially at equilibrium. As seen in the left panel of Fig. 4.3.2(a), in this case a number of pulses are generated in the resonator. The initial number of pulses depends on the total energy inside the resonator when the modulation is turned on [77, 113]. In the presence of pump phase modulation, each pulse is forced to move towards $\theta = \pi/2$ and merge with the other pulses. The pulse generated at $\theta = -\pi/2$ appears first to be stable but that too starts to move towards $\theta = \pi/2$ after $t = 2$ms. All of the pulses eventually merge, leaving one stable pulse whose waveform and spectrum are the same as those depicted, respectively, in Figs. 4.3.1(b) and (c). These observations

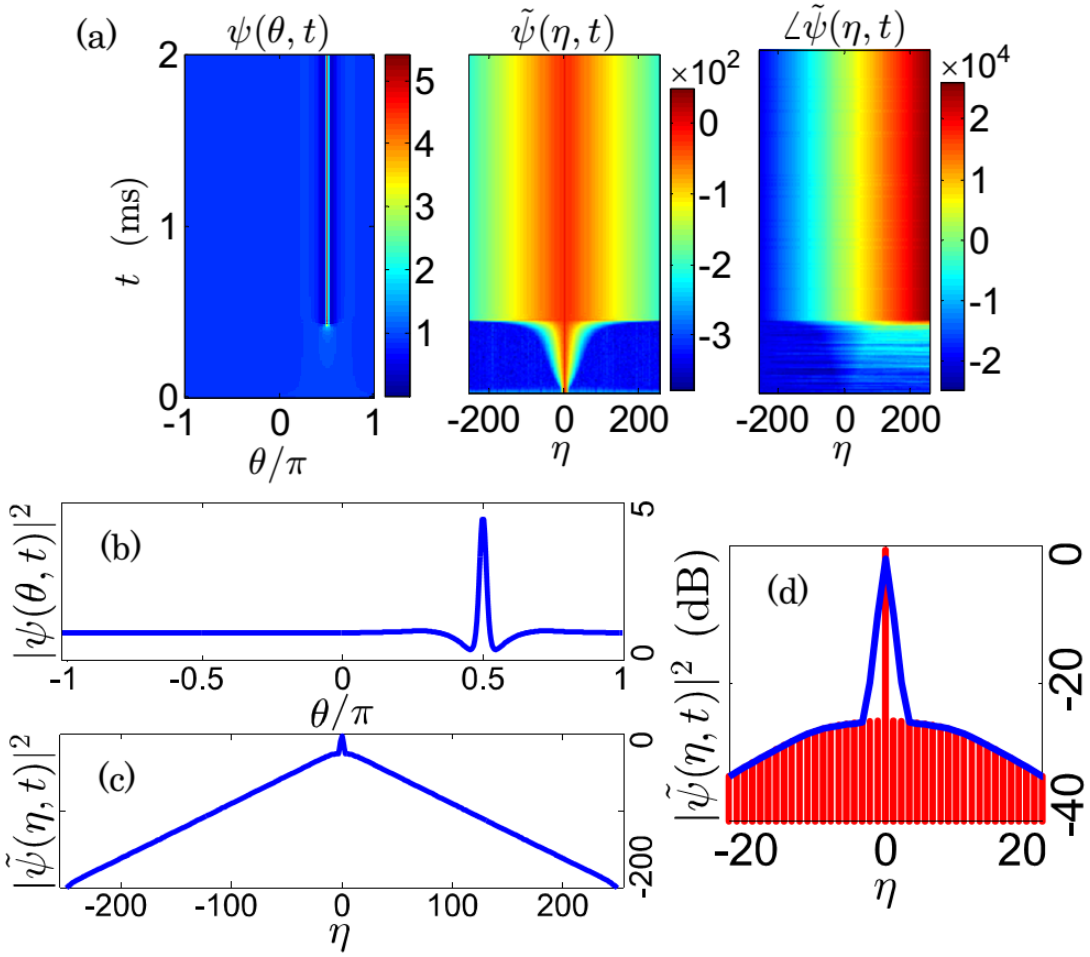

Fig. 4.3.1: Evidence of soliton formation in optical in a microresonator pumped by a phase-modulated CW laser through the nuumerical integration of Eq. (4.2.5) using the split-step Fourier transform method. (a) The temporal evolution of the waveform (ψ, left), spectrum ($|\tilde{\psi}| = a_\eta$, middle), and phase ($\angle\tilde{\psi} = \phi_\eta$, right) of the intra-cavity field starting from zero initial conditions and with input phase modulation. The phase has been unwrapped. ($\alpha = 2, F_0 = 1.4103, \delta_\mathrm{M} = 0.75$) (b) The generated pulse corresponding to $t = 2$ ms in (a). (c) The spectrum (in dB) of the pulse corresponding to $t = 2$ ms in (a). (d) Comparison of the spectrum near the pump for the generated soliton in (a) (blue curve) and a soliton evolved from a weak Gaussian pulse, $\psi(\theta, 0) = 0.4 + 0.2\exp[\theta^2/(2 \times 0.1^2)]$ as the initial condition (red spikes).

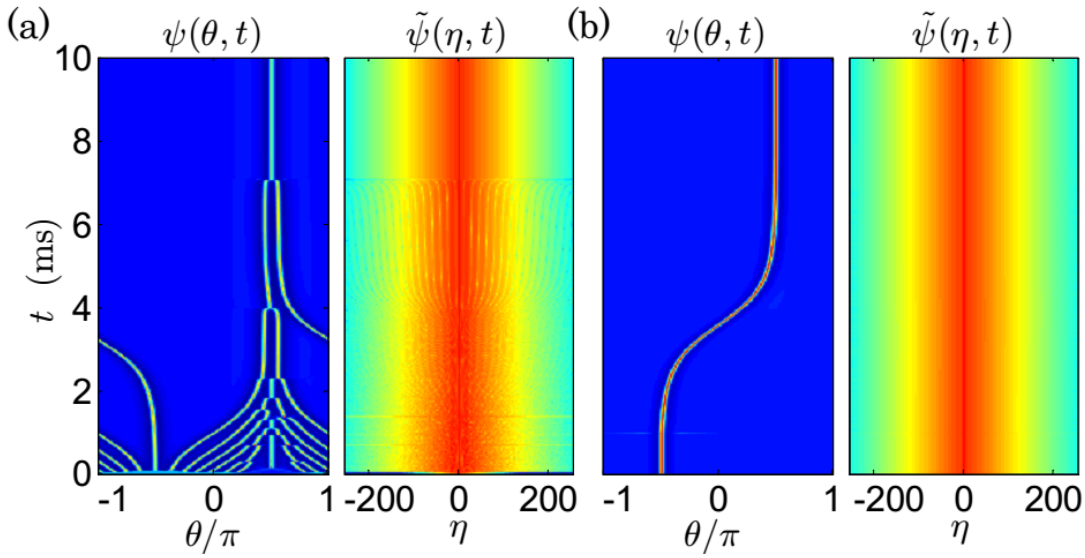

Fig. 4.3.2: Soliton merging under the influence of a phase-modulated pump. (a) Temporal evolution of the waveform (left) and spectrum (right) of the field envelope starting from $|\psi(\theta,0)|^2 = 0.9$ and with pump phase modulation. All parameters are the same as those in Fig. 4.3.1(a). (b) Same as (a) but starting with a weak Gaussian pulse $\psi(\theta,0) = 0.2 + \exp[-(\theta - 0.49\pi)^2/(2\times 0.1^2)]$ and no modulation. The modulation is turned on at $t = 1$ms. The vertical axis is time, as that in (a). ($\alpha = 2, F_0 = 1.3722, \delta_{\rm M} = 0.75$).

suggest that $\theta = \pm\pi/2$ are fixed points; $\theta = \pi/2$ is stable while $\theta = -\pi/2$ is unstable.

4.4 Discussion

4.4.1 Cavity field momentum

The behavior observed in Figs. 4.3.1 and 4.3.2 can be understood by considering the intra-cavity field momentum [114] defined by

$$P = \frac{1}{2}\int_{-\pi}^{\pi} \mathrm{d}\theta\, \psi^* \hat{\mathrm{p}}_\theta\, \psi + \text{c.c.}, \tag{4.4.1}$$

where $\hat{\mathrm{p}}_\theta = \langle\theta|\,\hat{\mathrm{p}} = -\mathrm{i}\partial/\partial\theta$ is the momentum operator ($\hat{\mathrm{p}}$) in the coordinate space, and the superscript "*" and "c.c." denote complex conjugate. Using this definition together with Eq. 4.2.5, the equation for the momentum time rate of change is found

to be

$$\dot{P} = -P + \int_{-\pi}^{\pi} \mathrm{d}\theta\, \psi^* \hat{\mathrm{p}}_\theta\, F + \mathrm{c.c.}, \tag{4.4.2}$$

where $F(\theta, \tau) = F_0 \exp[\mathrm{i}\, \delta_\mathrm{M}\, \sin(\theta)]$ for pump phase modulation. The first term on the right-hand side of Eq. (4.4.2) appears due to damping while the second term originates from the pump phase modulation. The momentum is a decaying exponential function of time in the absence of phase modulation but will be driven by the second term with modulation. Owing to the periodic boundary conditions of Eq. (4.2.5) and the even symmetry of $F(\theta, \tau)$ around $\theta = \pm\pi/2$, a localized pulse solution of this equation is an even function of θ around $\theta = \pm\pi/2$. The integral on the right-hand side of Eq. (4.4.2) is therefore zero for a soliton centered at $\theta = \pm\pi/2$, because the integrand is an odd function of θ around either point (ψ is even and $\partial_\theta F$ is odd). It is, however, positive for any pulse $\psi(\theta, \tau)$ centered at $\theta = \theta_0 \in (-\pi/2, \pi/2)$ and is negative for one localized around a point outside of this region in the resonator. Therefore, small perturbations can destabilize a pulse centered at $\theta = -\pi/2$ and move it away from this point; any pulse inside the resonator will be dragged towards $\theta = \pi/2$. In other words, $\theta = \pi/2$ is stable while $\theta = -\pi/2$ is unstable. To further test this explanation, we show in Fig. 4.3.2(b) an example where the initial condition in the absence of phase modulation is a weak Gaussian pulse centered at a point slightly to the right of $\theta = -\pi/2$. This pulse evolves rapidly into a soliton. The modulation is turned on at $t = 1$ms which results in the deflection of the soliton towards $\theta = \pi/2$. The soliton propagates without deviating to either side after reaching this point. The preceding discussion also shows that solitons generated through input phase modulation tend to be more robust than solitons in the absence of this type of seeding, because any perturbation in the position of the pulse will be opposed and suppressed by the modulated pump. We note that a non-zero phase ϕ for the modulator (i.e., $F(\theta, \tau) = F_0 \exp[\mathrm{i}\delta_\mathrm{M}\, \sin(\theta - \phi)]$) will shift the equilibria and consequently the pulse position and can be used for *advancing* or *delaying* the pulses

collected at the output port.

4.4.2 Removing the pump modulation

We indicated earlier that the modulation of the pump phase can lead the system towards the same fixed points available in the absence of the modulation and through a suitable input (Fig. 4.3.1(d)). It is therefore reasonable to expect that the generated solitons will be sustained if the modulation is turned off adiabatically. This is seen in Fig. 4.4.1(a) where a soliton is initially formed by pump phase modulation starting from a cold cavity. From $t_0 = 1$ ms, we slowly reduce the modulation depth to zero. The soliton which was originally formed by phase modulation is sustained after the modulation is removed. For the purpose of comparison, we show in Fig. 4.4.1(c) the effect of the abrupt removal of the modulation at $t_0 = 2$ ms. It is as if a shock is inflicted on the system which leads to the generation of four other pulses. As time passes, the extra pulses on each side of the original soliton move slightly away from each other and stabilize by $t_0 = 4$ ms. As seen in Fig. 4.4.1(d), the final spectrum in this case does no longer consist of a comb with smooth envelope and small line-to-line amplitude variations. Note that in Fig. 4.4.1 the origin of θ has been shifted to $\theta = -\pi/2$ for better visualization. From the perspective of nonlinear dynamics, the vanishing of the parameter δ_{M} alters the topography of the equilibria in the system described by Eq. 4.2.5. Intuitively, two scenarios are possible when a fixed point of interest remains an attractor after the change is applied. If the change is applied gradually, the state of the system remains in the basin of attraction of the fixed point (Fig. 4.4.1(b)). If, however, the change is abrupt, it may place the system in the basin of attraction of a different fixed point and, therefore, the final state of the system will be different (Fig. 4.4.1(d)). Figure 4.4.2 illustrates a simple mechanical analogue where a point mass (e.g., a small ball) is originally at the bottom of a potential well

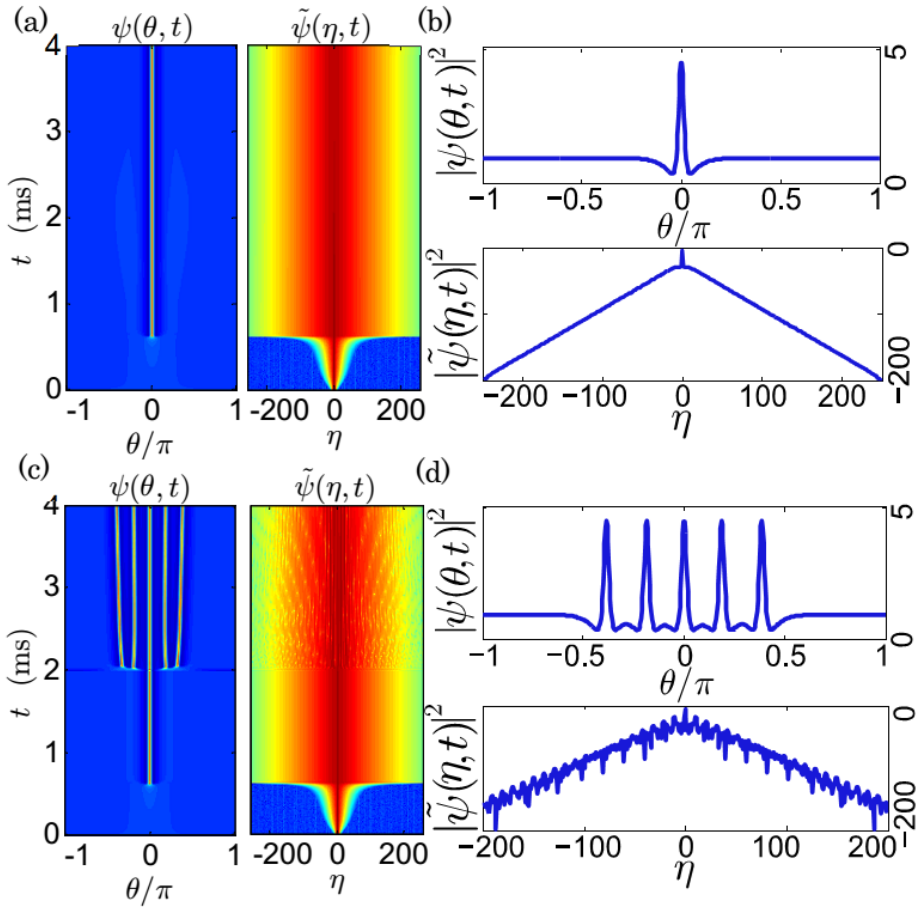

Fig. 4.4.1: Comparison of the adiabatic and abrupt removal of the input phase modulation. (a) The time evolution of the field envelope (left) and spectrum (right) when the modulation is adiabatically turned off: $\delta_{\rm M}(t > t_0) = 0.65\exp[-(t-t_0)^2/(2\sigma_{\rm M}^2)]$, $t_0 = 1$ ms, $\sigma_{\rm M} = 0.6$ ms. (b) Final waveform (top) and spectrum (in dB, bottom) in (a). (c) Same as (a), but for abrupt modulation removal at $t_0 = 2$ ms. (d) Final waveform (top) and spectrum (in dB, bottom) in (c). The field envelope has been shifted for better visualization. (Colorbar scales are the same as those in Fig. 4.3.1.)

(a valley). If the potential field is altered, two different scenarios corresponding to the cases of adiabatic and abrupt modulation removal are possible based on the pace of the change applied. This intuitive result has been verified rigorously and it has been shown that when a system starts sufficiently close to a stable equilibrium or limit cycle, it will follow this attractor when the parameter ($\delta_{\rm M}$ in our problem) is varied adiabatically [115]. We note that abrupt removal of the modulation does not necessarily lead to losing the single soliton. In particular, our numerical simulations

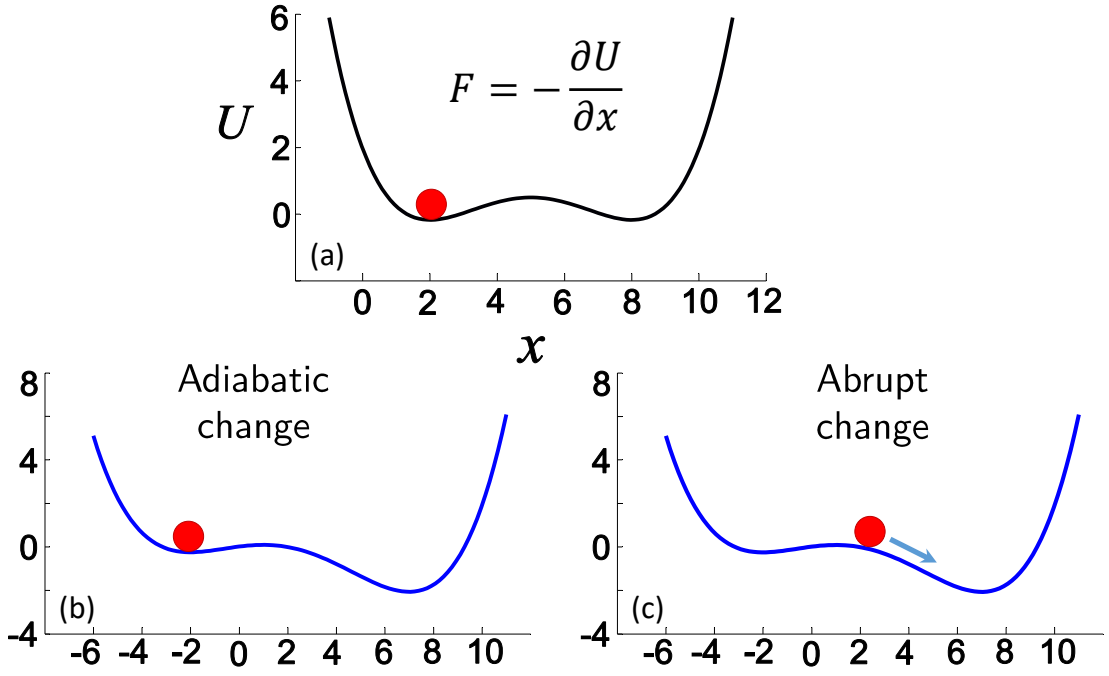

Fig. 4.4.2: Mechanical analogue for the adiabatic and abrupt removal of the phase modulation. (a) A point mass (e.g., a ball) is at rest at a locally stable equilibrium point (e.g., at the bottom of a valley). Imagine that the potential field $U(x)$ is changed, where x is the spatial coordinate. (b) If the potential field is changed adiabatically, the point mass will remain in the basin of attraction of the original fixed point (close to the bottom of the original valley where it lay at first) for the duration of the change. (c) If, however, the field is changed abruptly, the object may suddenly find itself in the basin of attraction of another fixed point (the valley on the right) and therefore fall under the dragging force of the potential to a different state. Note the original position of the point mass at $x = 2$.

show that for smaller pump amplitudes, (e.g., $F_0 = 1.3722$) the modulation could safely vanish abruptly.

4.4.3 Thermal resonance drift

We note that in practice, the laser pump frequency needs to be locked to the pumped resonance of the optical microresonator because the resonance will drift as a result of the large intra-cavity field intensities [54, 116]. This resonance drift results from the thermo-refractive and thermo-elastic effects as well as the intensity-dependent

refractive index (Kerr effect), each occurring on a different timescale. Since the solitons are generated when the pump is effectively red-detuned with respect to the pumped cavity resonance ($\sigma < 0$), thermal locking of the resonance to the laser will not be effective for material platforms where the combination of the Kerr, thermo-refractive, and thermo-elastic effects tends to red-shift the resonances. In such cases, other techniques for locking the laser to the resonance should be used [117, 118].

In Ref. [54], the self-stability of solitons in the presence of thermal effects and when the pump-resonance detuning is changed through a tailored pump wavelength ramp has been described. With the pump frequency kept constant and its phase modulated, the stability mechanism of the solitons after a number of them are generated, as in Fig. 4.3.2(a), and while they are coalescing is expected to be similar to that described in [54]: the fraction of the pump light which is traveling with the weak CW background of the intra-cavity field will effectively be red-detuned with respect to the resonance, while the fraction of the pump traveling with the soliton will effectively be blue-detuned. Since thermal effects happen on timescales much smaller than the cavity round-trip time, they depend on, and respond to, the average intra-cavity power. In microresonators, hence, the detuning-dependent change of the average intra-cavity power is dominated by the effectively blue-detuned soliton component (as opposed to the effectively red-detuned weaker background) of the intra-cavity field. As such, the resonator is expected to behave as being effectively blue-detuned and therefore self-stable during the merging of the pulses under phase modulation.

4.5 Summary and outlook

In summary, in this chapter a method for deterministic soliton formation in optical microresonators has been proposed based on phase modulation of the laser pump. Using a variant of the LLE, we showed, both numerically and analytically, that parametric

seeding by pump phase modulation allows us to create and manipulate solitons in a microresonator using a single driving laser. This technique also leads to enhanced soliton stability. We also showed that after solitons are generated, the seeding agent can be removed without affecting the generated solitons. Our findings support parametric seeding as a powerful means of control over frequency comb generation in optical resonators and help pave the path towards chip-scale ultra-short pulse sources.

Extensions of this method include using multiple laser pumps and controlling their individual frequency and power. However, one should bear in mind that such a scheme, has technical challenges. For instance, broadband microcomb generation requires that the different lasers be coherent. The frequencies of the different lasers, therefore, should carefully be controlled. Dual-pump excitation of frequency combs have been reported theoretically and experimentally [119, 120]. However, broadband microcombs with single-FSR spacing generated through bichromatic excitation have not been demonstrated yet.

CHAPTER 5

HIGH-ORDER DISPERSION OPTICAL FREQUENCY COMBS IN CRYSTALLINE RESONATORS FOR OPTICAL CLOCK APPLICATIONS

"It is an old story in physics that higher resolving power leads to new effects."

Edward M. Purcell, Nobel Lecture (1952)

In this chapter, I present an investigation of the effect of high-order dispersion on Kerr frequency comb generation in optical microresonators characterized by anomalous and normal group velocity dispersion (GVD) in realistic spheroidal crystalline calcium fluoride and magnesium fluoride resonators. These resonators hold record quality factors of up to 10^{11} and are currently being used in commercial resonator-based frequency comb products[1]. Numerical simulations indicate that all orders of GVD should be taken into account to obtain the correct envelope shape of the generated Kerr frequency comb. Practically, this means that in theoretical studies of frequency combs dispersion coefficients should be added one by one till one notices no significant change in the power spectrum of stable frequency combs (nonlinear system attractors). High-order GVD affects the 3-dB comb bandwidth, nonlinear conversion efficiency, and frequency recoil of the comb spectrum (i.e., spectral shift due to the generation of dispersive waves), as well as pulse peak power and the power dependence of the pulse timing. Additionally, high-order dispersion terms affect the spectral position of a dispersive wave generated in a microresonator. The results of this study emphasize the influence of the pump power on the dispersive wave emission frequency as well as the repetition rate of the generated frequency

[1]See, e.g., the website of OEwaves, Inc. at `http://www.oewaves.com`.

comb. The latter has significant practical ramifications, for instance for the use of resonator-based frequency combs in optical clocks. Competition between the generation of two different pulses corresponding to nearly the same spectral envelope is observed in the presence of quadratic and quartic GVD. One of these pulses takes a hyperbolic-secant soliton shape, while the other resembles a Gaussian pulse superimposed on a modulated pedestal. The appearance and stability of the latter pulse depends on the numerical integration technique utilized. In the final section, I present results of crystalline resonator dispersion engineering for the generation of record broadband near infra-red (NIR) microcombs for optical clock applications. These microcombs can be stabilized using Rubidium atoms and utilized for precise timekeeping[2].

5.1 Introduction

As noted earlier, temporal solitons can be stably generated in optical microresonators pumped with a continuous wave laser due to the balance between Kerr nonlinearity and anomalous GVD. The existence of high-order dispersion terms (i.e., third and higher-order dispersion) affects pulse dynamics and the frequency spectrum [121, 122]. For instance, it has been shown that third-order dispersion helps to stabilize frequency combs [123], and that fourth-order (quartic) dispersion affects the comb bandwidth [124]. The comb spectrum becomes asymmetric and the soliton can emit a dispersive wave (DW) when perturbed by the high-order dispersion of a proper type, in a process which is an optical analogue of Cherenkov radiation [55, 125]. Dispersive wave emission has been experimentally shown to broaden the comb spectral

[2]This chapter is partially based on results presented in [35].

bandwidth to two-thirds of an octave. Such a broad frequency comb can be self-referenced and used in frequency metrology, as discussed in Section 1.4. The 3-dB comb bandwidth, which is related to the temporal pulse width, is also affected by the dispersive wave [99].

In this chapter, I study several effects associated with Kerr frequency comb generation in microresonators characterized by complex chromatic dispersion. Using examples of spheroidal crystalline calcium fluoride (CaF_2) and magnesium fluoride (MgF_2) resonators, I study the shapes of the frequency comb envelope and the associated optical pulses for different dispersion parameters. The simulations show that a truncation of the dispersion sequence would lead to drastic modifications of the comb parameters. It also affects the existence range of the frequency comb. This result points to the necessity of considering all orders of dispersion (till further dispersion coefficients no longer affect the comb spectrum significantly) to obtain a meaningful result in the simulations.

Additionally, I study the influence of cubic and quartic GVD terms on the properties of a frequency comb in the case of anomalous second-order GVD. While a normal quartic (fourth-order) GVD term initiates and governs the generation of dispersive waves in the resonator, anomalous quartic GVD shifts the dispersive wave frequency away from the carrier and, eventually, suppresses its generation, in accordance with earlier predictions made for optical fiber systems [126].

I consider, moreover, the power dependence of the DW spectral position and highlight the effect of high-order GVD and DW generation on comb repetition rate. It is shown that there are cases in realistic microresonator systems where the odd GVD terms dominate over the even terms. This happens, for instance, in an MgF_2 whispering gallery mode resonator in the vicinity of the zero-GVD point. It is found that phase-locked frequency comb generation is feasible in this case. The pulse shape, however, is neither of sech nor Gaussian type. DW generation is also observed at a

spectral position predicted by the phase-matching condition including residual dispersion as well as comb power.

At the end of the discussion on higher-order dispersion, I report an example of the competition between anomalous quadratic and quartic GVD terms observed in resonators with negligible cubic GVD. This competition results in the generation of frequency combs with nearly identical power spectra but with two different optical pulse shapes. One of the pulses is a sech-shaped soliton, while the other is a Gaussian-shaped pulse, similar to those previously observed in photonic crystal waveguides with pure quartic GVD [127]. Interestingly, the presence of the Gaussian-shaped pulse is predicted by the numerical model based on coupled wave ordinary differential equations; see Section 2.2.2. The solution of the Lugiato-Lefever equation (LLE) based on the split-step Fourier transform method, however, predicts that the non-soliton pulse is unstable. Understanding the reason for this inconsistency merits further study, but could be attributed to periodic boundary conditions. These conditions are automatically satisfied when fast Fourier transform (FFT) is used for implementing the linear half-step in the split-step integration of the LLE, but are less obvious in the case of the model described by a set of coupled ordinary differential equations.

I conclude this chapter by presenting results on crystalline resonator dispersion engineering for the generation of near infra-red (NIR) microcombs. These microcombs can be stabilized using Rubidium atoms and utilized in an optical clock. The utilized resonators have free-spectral ranges of approximately 20 GHz so that their FSR can be resolved using commercially available photodetectors. NIR microcombs are important in particular because to date no material platform supporting high-Q resonators with proper dispersion for broadband microcomb generation in this wavelength range has been identified.

5.2 High-order GVD in dispersion engineered optical resonators

To show the importance of including higher-order dispersion terms in theoretical studies of microcombs and in design and dispersion engineering of optical resonators, I use dispersion parameters for a realistic crystalline CaF_2 resonator in the near-infrared (NIR) regime pumped at 760 nm. The importance of this part of the frequency spectrum will be discussed in Section 5.7. This crystalline resonator has a radius of 1 mm ($D_1 = 2\pi \times 33.42$ GHz). Its modal effective mode area can be approximated as an ellipse with semi-major and semi-minor axes $a_1 = 5\,\mu$m and $a_2 = 1.25\,\mu$m. Dispersion in this resonator can be engineered through changing the chamfer angles, see Fig.1.8.1(d). Other dispersion coefficients for this resonator at the pumping wavelength of $\lambda_P = 760$ nm are $D_2 = -33206$ rad/s, $D_3 = -163.05$ rad/s, $D_4 = 21.8758$ rad/s, $D_5 = 0.3547$ rad/s, and $D_6 = -0.0106$ rad/s, with the second-order GVD (D_2) depicted in Fig. 5.2.2(a) and the residual (or integrated dispersion) curve shown in Fig. 5.2.1(b). The dispersion curves are made from numerical resonance frequency vs. mode number data found using COMSOL. (See Section 1.11.) As seen in these figures, the zero GVD point is around 770 nm. It is worth noting that the sharp change in D_2 is caused by mode interactions (avoided mode crossings) in the resonator [128].

In Figs. 5.2.2, 5.2.3, 5.2.4, 5.2.5, and 5.2.6, the different dispersion coefficients are added one by one, starting from the second-order GVD (D_2). It is seen that since the comb is pumped at 760 nm in the normal dispersion regime, if higher-order dispersion terms could be ignored, it will be a dark soliton, Fig. 5.2.2. Addition of the third-order dispersion term breaks the symmetry of the parabolic residual dispersion ($D_{\text{int}} = D_2\eta^2/2$), and shifts the comb spectrum slightly towards higher frequencies, Fig. 5.2.3. Interestingly, while the resonator is pumped in the normal dispersion regime at 760 nm, as noted in Fig. 5.2.1, and the zero GVD point is

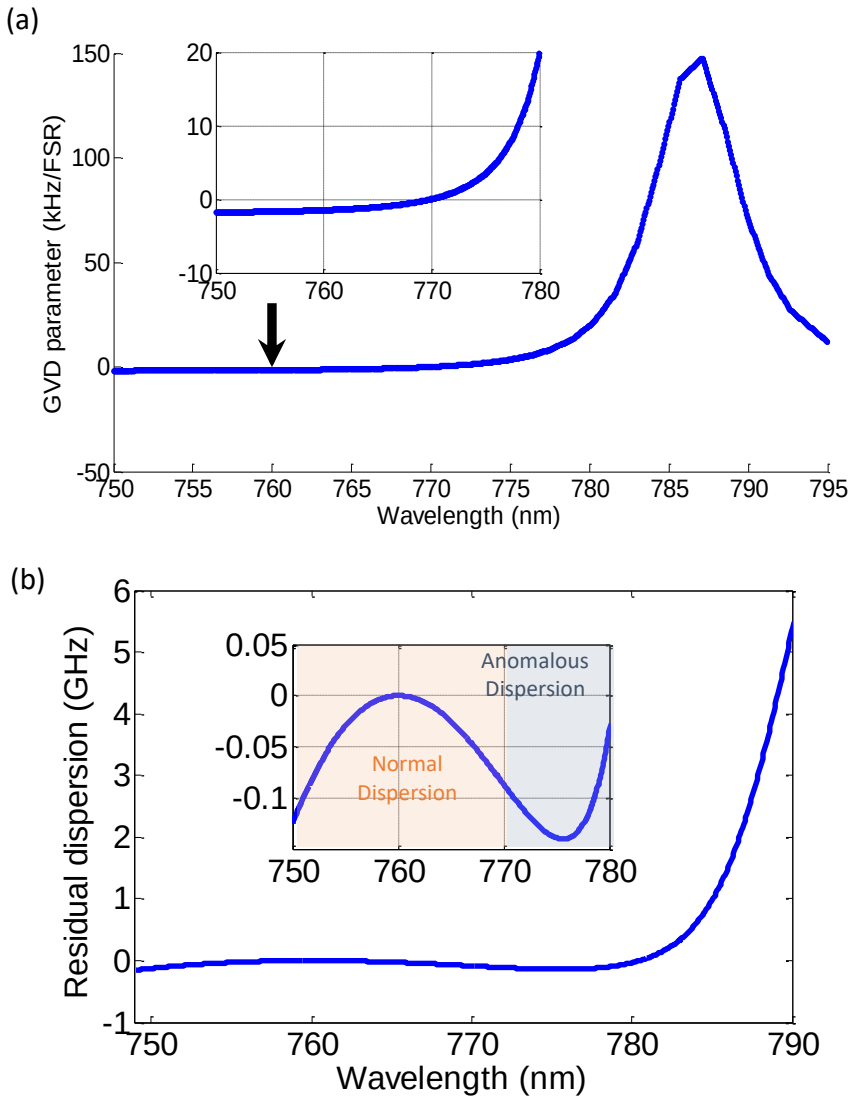

Fig. 5.2.1: Second-order dispersion (D_2) (a) and residual (or integrated) dispersion curve (b) for a realistic crystalline CaF_2 resonator in the near-IR regime. This crystalline resonator has a radius of 1 mm ($D_1 = 2\pi \times 33.42$ GHz). Its modal effective mode area can be approximated as an ellipse with semi-major and semi-minor axes $a_1 = 5\,\mu$m and $a_2 = 1.25\,\mu$m. Dispersion in this resonator can be engineered through changing the chamfer angles, see Fig.1.8.1(d). Other dispersion coefficients for this resonator at 760 nm are $D_2 = -33206$ rad/s, $D_3 = -163.05$ rad/s, $D_4 = 21.8758$ rad/s, $D_5 = 0.3547$ rad/s, and $D_6 = -0.0106$ rad/s. It is seen that the zero GVD point for this resonator is around 770 nm. The black arrow in panel (a) points at the pump wavelength.

nearly 10 nm away from the pump, the generated microcomb changes from a dark soliton to a bright soliton with the inclusion of D_4, cf. Figs. 5.2.2 and 5.2.3. This is due to the comparably large fourth-order dispersion coefficient. When D_5 is also taken into account, compared to Fig.5.2.4, a dispersive wave which is red-shifted with respect to the pump appears in the comb power spectrum. When all dispersion coefficients from D_2 through D_6 are considered, a frequency comb with particular features appears. The pulse shape resembles more a dark soliton (Fig.5.2.2) than a bright pulse (Fig.5.2.4). This is due to the negative sign of D_6, which is the same as that of d_2 and enhances the influence of pumping in the normal dispersion regime. A strong dispersive wave appears at around 738 nm. The spectral position of this DW will be discussed in Sections 5.3 and 5.4. I verify the stability of the generated microcomb shown in Figs. 5.2.6 and 5.2.7, by looking at the spectrograms shown in Fig. 5.2.8. It is seen that the pulse stably propagates with time and preserves it shape and coherence.

The reader may ask, when should the process of adding higher-order dispersion terms in the integration of the LLE stop? One should add higher-order dispersion terms till they notice that the power spectrum of the comb does not change significantly. Alternatively, all dispersion terms required for a very close curve fitting match to the numerically calculated (or measured) residual dispersion curve need to be considered.

The discussion and example of this section demonstrate that for successful dispersion engineering for practical applications, all higher-order dispersion terms need to be taken into account and merely minimizing the second-order GVD is not sufficient.

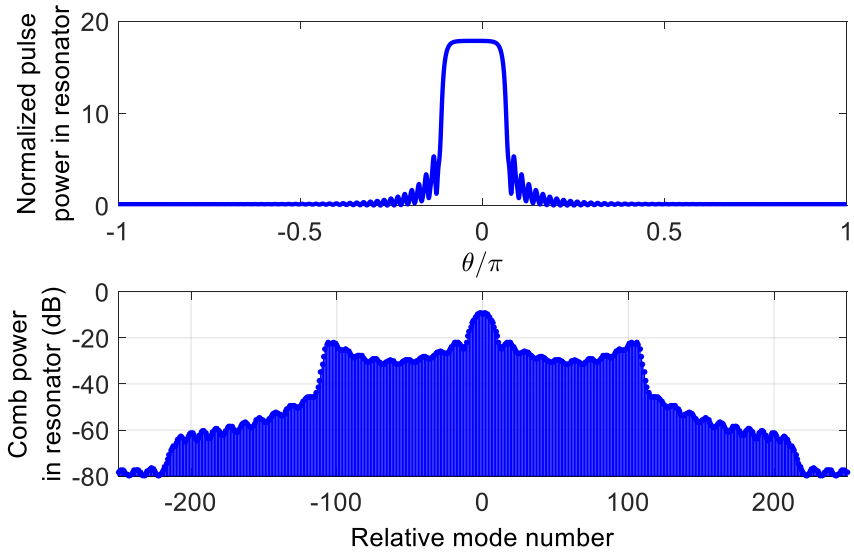

Fig. 5.2.2: Microcomb generated when only the second-order dispersion coefficient D_2 is considered. Since the resonator is pumped in the normal dispersion regime at 760 nm, the generated comb is a dark soliton. Pump power is 90 mW and its detuning from the nearest resonance is 16.7×HWHM. Upper panel is the pulse shape while the lower panel depicts the comb power spectrum.

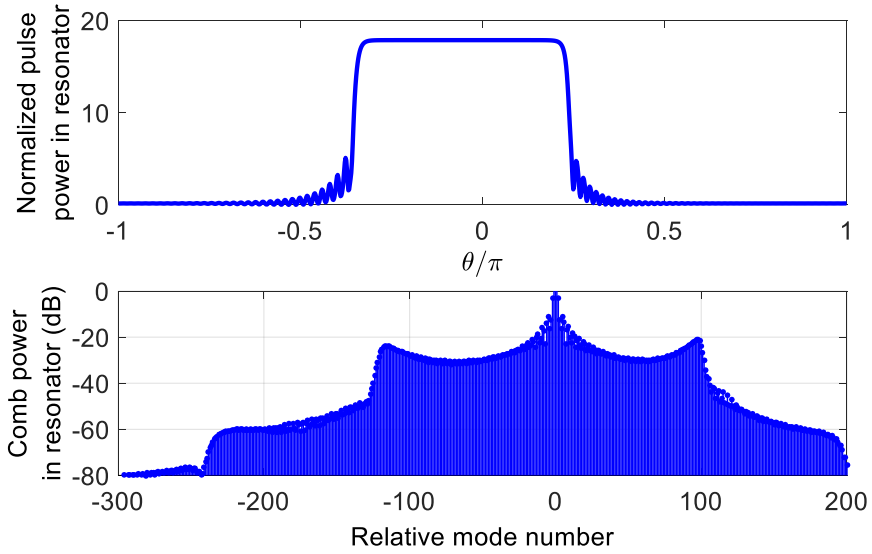

Fig. 5.2.3: Microcomb generated when the second- and third-order dispersion coefficient D_2 and d_3 are considered. Note that compared with Fig.5.2.2, the comb spectrum is slightly shifted due to the asymmetry introduced by D_3, yet the comb still corresponds to a dark soliton. Upper panel is the pulse shape while the lower panel depicts the comb power spectrum.

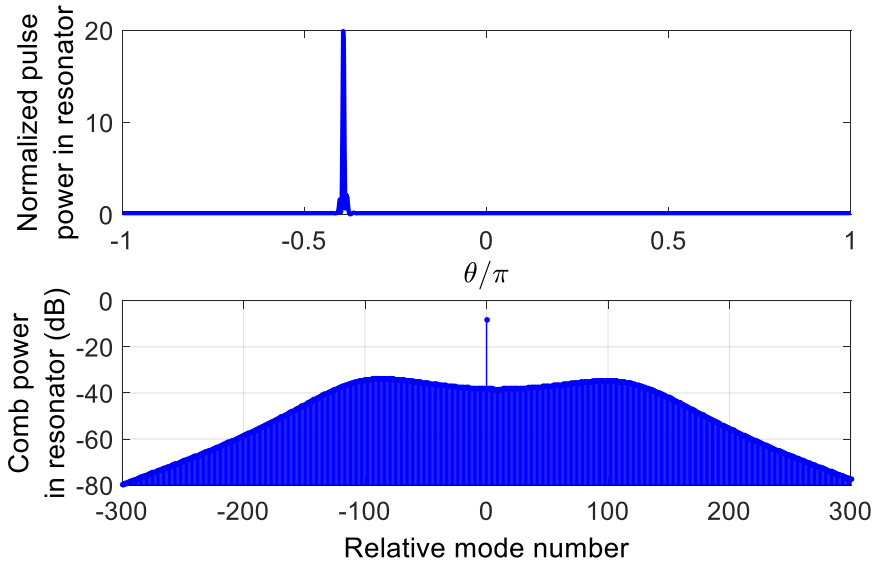

Fig. 5.2.4: Microcomb generated when the second-, third-, and fourth-order dispersion coefficients, D_2, D_3, and D_4 are considered. It is interesting that while the resonator is pumped in the normal dispersion regime at 760 nm, as noted in Fig. 5.2.1, and the zero GVD point is nearly 10 nm away from the pump, the generated microcomb changes from a dark soliton to a bright soliton with the inclusion of D_4. Compare Figs. 5.2.2 and 5.2.3. Upper panel is the pulse shape while the lower panel depicts the comb power spectrum.

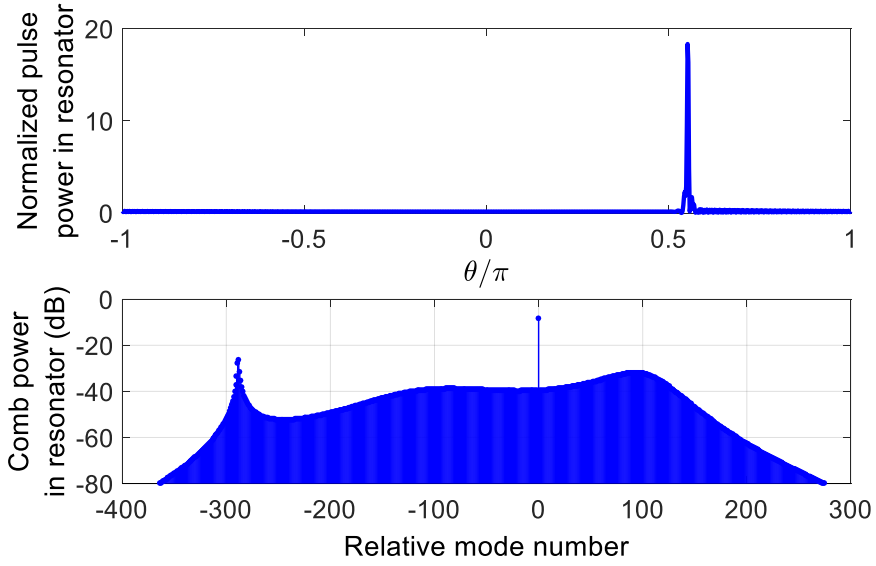

Fig. 5.2.5: Microcomb generated when the second-, third-, fourth-, and fifth-order dispersion coefficients, D_2, D_3, D_4, and D_5 are considered. Compared to Fig.5.2.4, a dispersive wave red-shifted with respect to the pump has appeared with the inclusion of D_5. Upper panel is the pulse shape while the lower panel depicts the comb power spectrum.

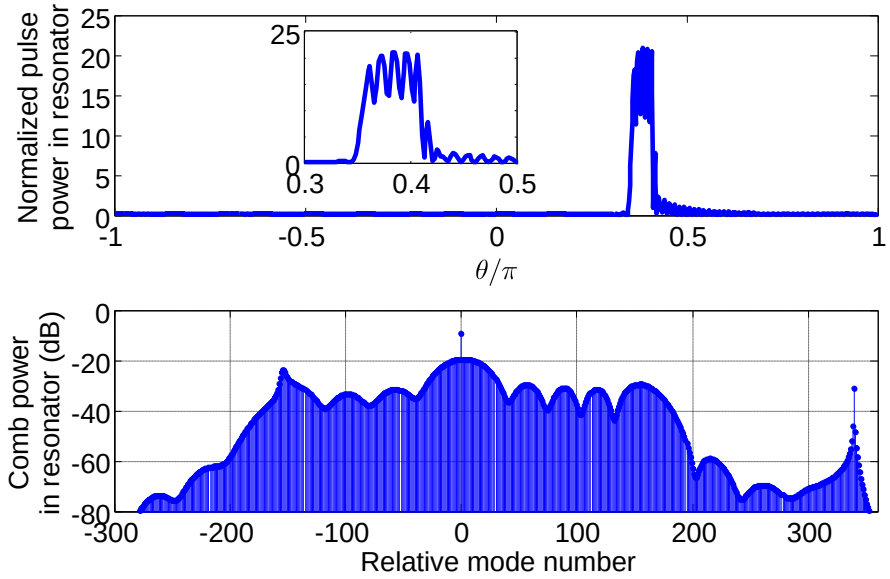

Fig. 5.2.6: Microcomb generated when all dispersion coefficients, D_2 through D_6 are considered. Higher-order dispersion terms do not change power spectrum of the comb significantly, and can therefore be dropped for this pumping power and frequency. Upper panel is the pulse shape while the lower panel depicts the comb power spectrum. The inset in the upper panel casts a closer look at the pulse shape. The pulse shape resembles more a dark soliton (Fig.5.2.2) than a bright pulse (Fig.5.2.4). This is due to the negative sign of D_6.

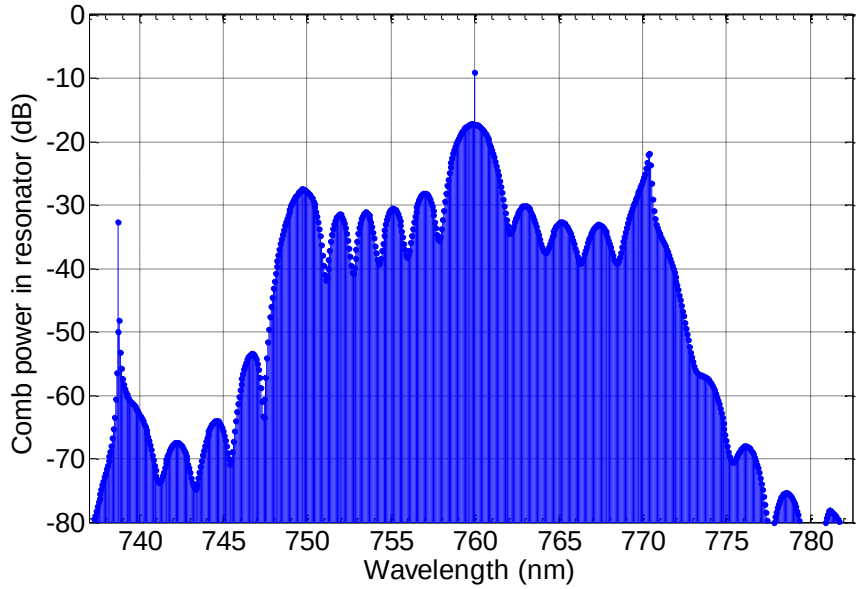

Fig. 5.2.7: The power specturm of the microcomb shown in Fig. 5.2.6 vs. wavelength, which shows a broadband NIR comb spanning more than 40 nm.

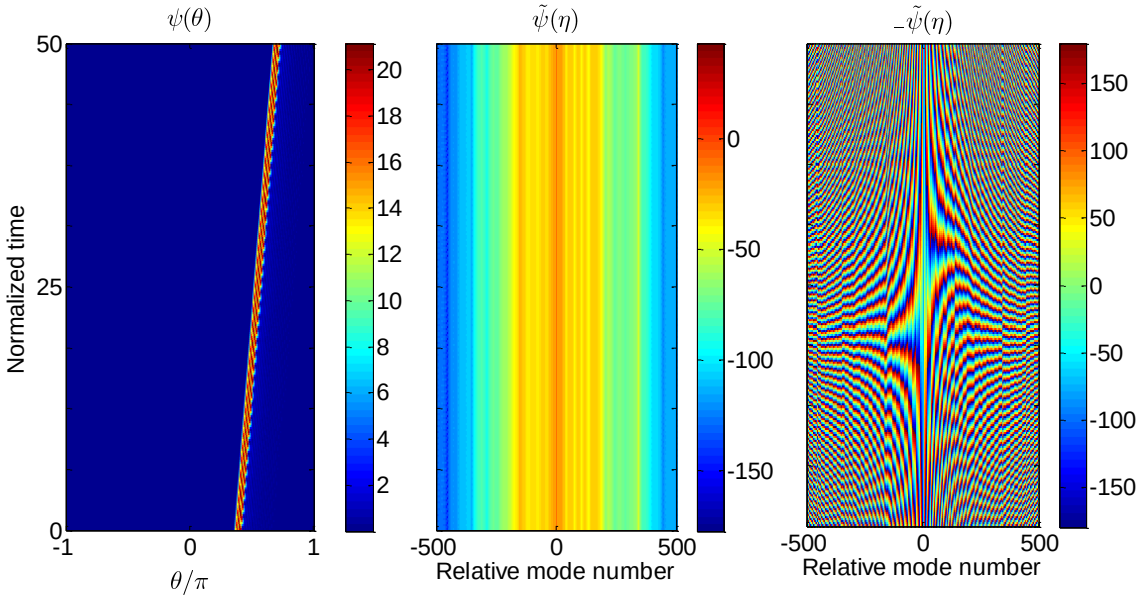

Fig. 5.2.8: The generated microcomb shown in Figs. 5.2.6 and 5.2.7 is stable as shown here, where it propagates stably over 50 normalized times, equal to 100 cavity photon lifetimes. The left panel is the intra-cavity pulse, the middle panel is the power spectrum vs. mode number, and the right panel is its phase spectrum vs. mode number. The vertical axis in all panels is time.

5.3 Dispersive waves and phase-matching condition

As emphasized in the previous sections, the presence of high-order GVD results in modifications of the Kerr comb spectrum. One of the possible modifications is the appearance of a "dispersive wave". The wave corresponds to a jump in the power and phase of the Kerr frequency comb power spectrum and represents a convenient feature for visualization of the impact of high-order dispersion. It is possible to obtain an analytical formula describing the frequency of a dispersive wave generated in a microresonator due to the presence of high-order GVD. To that end, let's recall that the dissipative Kerr microcomb soliton (LLE solution in the absence of higher-order GVD) is given approximately by [54, 103]

$$\psi(\theta) = A_{\mathrm{CW}} + A_{\mathrm{S}} \mathrm{e}^{\mathrm{i}\phi_{\mathrm{S}}} \mathrm{sech}(\sqrt{\Delta\omega_0 P_{\mathrm{S}}/4D_2}\theta). \tag{5.3.1}$$

In this expression, A_{CW} is the CW background, A_{S} is the soliton maximum amplitude, $P_{\mathrm{S}} = A_{\mathrm{S}}^2$ is the soliton peak power, and ϕ_{S} is the soliton phase. It can easily be seen from the LLE, and comparing with optical fibers (see, e.g., Chapter 12 in [68]), that a wave characterized by the comb tooth label (mode number) j_{DW} can be phase-matched with the above soliton if its mode number satisfies

$$\sum_{n=1}^{N} \frac{D_n}{n!}(j_{\mathrm{DW}} - j_0)^n + g_0 P_{\mathrm{S}} = 0. \tag{5.3.2}$$

where g_0 is the nonlinear FWM gain introduced in the derivation of the LLE in Section 2.2.2. This expression is the phase matching condition for dispersive wave emission, which is similar to that used in optical fibers [68]. It includes the phase contributed by the Kerr effect as well. This effect can usually be neglected in fiber cavities, but is pronounced in microresonators due to large field enhancement inside the cavity. The spectral position of a dispersive wave can be calculated by this phase matching condition.

It is obvious that the above phase matching condition cannot be satisfied if $D_2 > 0$ (anomalous dispersion) and dispersion beyond the second-order is negligible. If D_3 is negative, however, a wave can be phase matched with the soliton propagating in the resonator and a DW peak will appear in the spectrum. Figure5.3.1 shows an example comb generated with realistic dispersion coefficients for a crystalline CaF_2 resonator where a strong dispersive wave is generated a few hundred FSR's away from the pump. For this example, $D_2 = 2\pi \times (870.67)$ rad/s and $D_3 = 2\pi \times (-6.59)$ rad/s. The foregoing discussion also justifies the DW seen around 738 nm in Fig. 5.2.7. It is worth noting that dispersive wave emission in microcombs and optical fiber solitons is the optical analogue of "Cherenkov radiation" [129].

The analysis presented in this section is intuitive and borrows insight from soliton formation in the presence of higher-order dispersion in optical fibers. This insight is important particularly in appreciating the influence of higher-order dispersion and pump power on the change of pulse repetition rate, as will be explored in the next

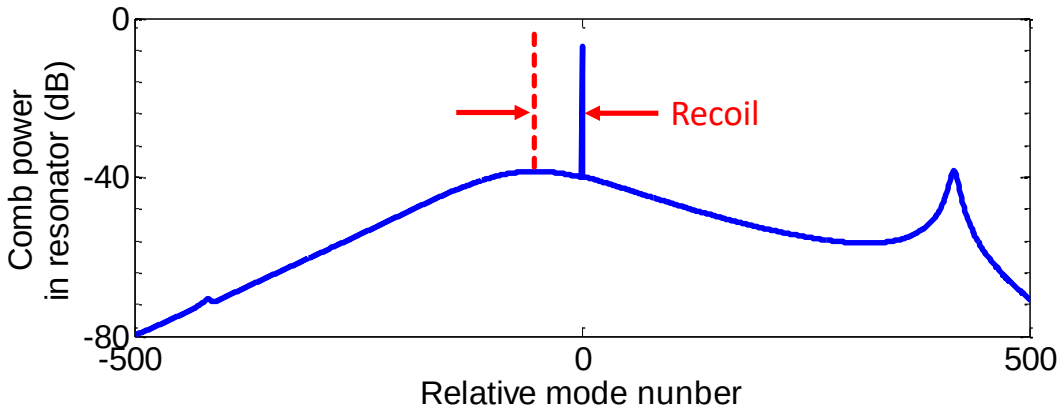

Fig. 5.3.1: Higher-order dispersion can lead to dispersive wave emission in optical frequency combs. The power spectrum of a microcomb generated with realistic dispersion coefficients for a crystalline CaF_2 resonator is shown, where a strong dispersive wave is generated a few hundred FSR's away from the pump. For this resonator, $D_2 = 2\pi \times (870.67)$ rad/s and $D_3 = 2\pi \times (-6.59)$ rad/s.

section. Nonetheless, more rigorous mathematical approaches could be taken for finding the spectral position of the emitted dispersive wave; see, e.g., [122].

5.4 Change of repetition rate due to higher-order dispersion

The repetition rate of an ideal Kerr frequency comb (with second-order GVD only) does not depend on the pump power. However, this is no longer the case in the presence of high-order GVD, because the third and higher-order dispersion terms result in the transfer of pump fluctuation to the repeti-tion rate [130]. This effect could be understood based on dispersive waves. The dispersive wave is one of the possible consequences of high-order GVD and it is a coherent part of the frequency comb whose spectral position depends on the pump power. The dispersive wave radiation is accompanied by the spectral shift of the peak of the comb spectrum envelope (i.e., soliton recoil; see Fig. 5.3.1 and the discussion below in terms of the soliton momentum) and will hence affect the comb repetition rate. Consequently, the pump fluctuations will be transferred to the comb repetition rate through the

dispersive wave. On one hand, the DW allows the comb repetition rate to be tuned by changing the optical power. On the other hand, it destabilizes the frequency comb if the pump is unstable. This property plays an important role in several practical applications of Kerr frequency combs, most notably in optical clocks.

The shift of the soliton power spectrum peak from the pump is referred to as "soliton recoil", Fig. 5.3.1. This effect can be understood using the soliton momentum defined in Section 4.4.1. Using Eq. (4.4.2) for a CW pump, the following equation of motion can be found for the momentum P

$$\dot{P} = -2P, \tag{5.4.1}$$

which has a simple decaying exponential solution $P(\tau) = P_0 \exp(-2\tau)$, for some constant P_0, and its steady-state solution is

$$P(\tau \to \infty) = 0. \tag{5.4.2}$$

(Even for a seeded comb, if steady-state is achieved, the drive term in Eq. (4.4.2) will disappear and the above equation of motion will prevail. It is worth noting that in the absence of loss in the NLSE, momentum will be conserved. Please note that the effect of Raman scattering was not included in the derivation of the above equation of motion for the soliton momentum.) Using the definition of P, Eq. (4.4.1), and expanding the waveform $\psi(\theta)$ in modal amplitudes $\tilde{a}_\eta$ (as in Chapter 3),

$$\psi(\theta, \tau) = \sum_{\eta=-\infty}^{\infty} \tilde{a}_\eta(\tau) \exp(\mathrm{i}\eta\theta),$$

momentum can be written in terms of the relative mode number and the complex modal amplitudes, i.e.,

$$P = 2\pi \sum_{\eta} \eta |\tilde{a}_\eta|^2. \tag{5.4.3}$$

Equation (5.4.3) shows that momentum plays the role of the "center of mass" (CM) for the power spectrum. This notion is explained in Fig. 5.4.1. Let's recall that the

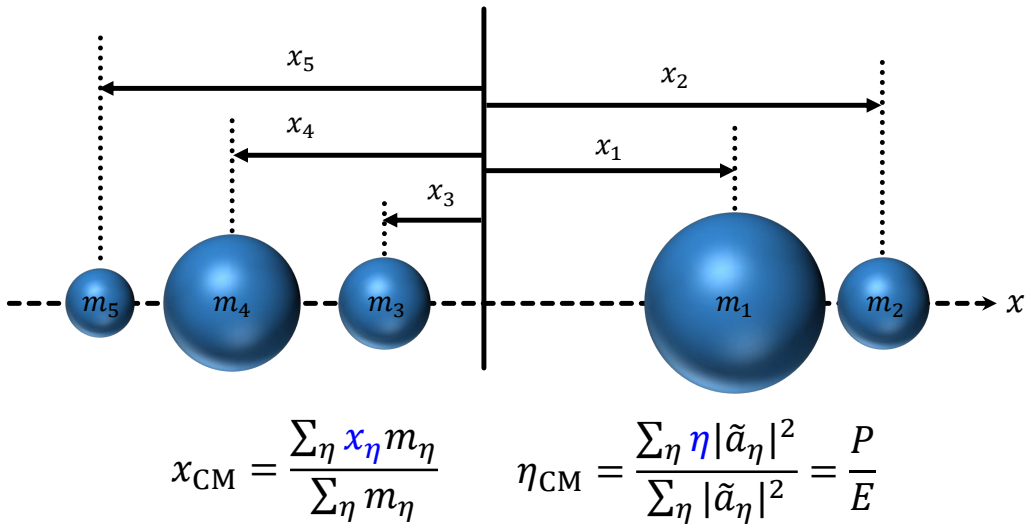

Fig. 5.4.1: Pulse momentum as center of mass for an optical frequency comb. This figure reviews how the center of mass (CM) of a group of point masses is found. If the distance from the center of spatial coordinate to the position of each point mass (x_η) is replaced by the relative mode number (η) and its mass (m_η) is replaced by the power in the corresponding comb tooth ($|\tilde{a}_\eta|^2$), one realizes that the definition of CM turns into the ratio of momentum and energy for a frequency comb. Therefore, pulse momentum plays the role of CM for the frequency comb when viewed in the frequency domain.

energy of the waveform $\psi(\theta, \tau)$ is found from

$$\int_{-\pi}^{\pi} \mathrm{d}\theta \, |\psi(\theta, \tau)|^2 = 2\pi \sum_{\eta=-\infty}^{\infty} |\tilde{a}_\eta(\tau)|^2.$$

Also, the CM for a group of point particles with masses m_η and located at positions x_η with respect to the origin of a given coordinate system is found from

$$x_{\mathrm{CM}} = \frac{\sum_\eta x_\eta m_\eta}{\sum_\eta m_\eta},$$

where η is an integer labeling the point masses. If the distance from the center of the spatial coordinate to the position of each point mass (x_η) is replaced by the relative mode number (η) and its mass (m_η) is replaced by the power in the corresponding comb tooth ($|\tilde{a}_\eta|^2$), one realizes that the definition of CM turns into the ratio of momentum and energy for a frequency comb. Therefore, pulse momentum plays the role of CM for the frequency comb when viewed in the frequency domain.

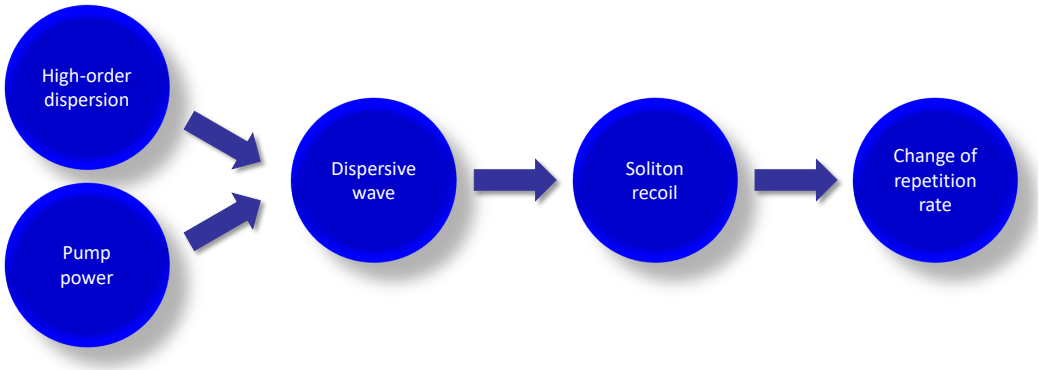

Fig. 5.4.2: The relationship between pump power fluctuations and the change of pulse repetition rate in optical microresonators. High-order dispersion and pump power affect dispersive wave emission in microcombs. Generation of dispersive wave leads to soliton recoil, and hence change of the repetition rate of the microresonator-based pulse. As such, pump power affects the repetition rate and pump power fluctuations lead to instability of the pulse repetition rate.

Referring to Eq. (5.4.2), one notes that as a result of dissipation (loss) the momentum of a stable pulse at steady state is zero. Consequently, if a dispersive wave is emitted to one side of the pump, the power spectrum will shift to the opposite direction to compensate the added weight of the DW and keep the momentum (frequency comb center of mass) intact (at zero). This explanation justifies soliton recoil or the shift of the soliton power spectrum peak in Fig. 5.3.1. As noted earlier, this shift corresponds to the change of repetition rate. Essentially, the repetition rate will change from $D_1/2\pi$ at the position of the pump to the FSR at the new spectral position of the power spectrum peak.

The repetition rate of an ideal Kerr frequency comb (with second-order GVD only) does not depend on the pump power. However, this is no longer the case in the presence of high-order GVD, because the third and higher-order dispersion terms result in the transfer of pump fluctuation to the repetition rate [130]. This effect could be understood based on dispersive waves. The dispersive wave is one of the possible consequences of high-order GVD and it is a coherent part of the frequency comb whose spectral position depends on the pump power, see Section 5.3. Emission

of a dispersive wave, as explained in this section, is accompanied by soliton recoil and will hence affect the comb repetition rate. Consequently, the pump fluctuation will be transferred to the comb repetition rate through the dispersive wave, see Fig. 5.4.2. On one hand, the dispersive wave allows the comb repetition rate to be tuned by changing the optical power. On the other hand, it destabilizes the frequency comb if the pump is unstable. This property can be important for several practical applications of Kerr frequency combs such as optical clocks.

5.5 Dominant third-order dispersion

We have so far seen examples of the generation of dispersive waves far from the pump frequency. It is also interesting to consider the generation of dispersive waves in the vicinity of the zero GVD point. In this case, the dispersive wave is expected to appear near the pump frequency because DW is usually emitted from the anomalous into the normal dispersion regime. This case can be practically realized in an MgF_2 WGM resonator having an FSR of approximately 104 GHz and pumped at around 1550 nm.

Figure 5.5.1(a) illustrates the second-order GVD for an MgF_2 spheroidal microresonator, and Figs. 5.5.1(b) and (c) show the residual dispersion for this resonator when it is pumped at 1558.5 nm and 1553.5 nm, respectively; the pumping wavelengths are indicated by the two arrows in panel (a). While the third-order GVD is dominant for both pumping wavelengths, its effect is more pronounced closer to the zero GVD point (1553.5 nm). The presence of higher-order GVD terms leads to crossing the zero residual dispersion level at a point separated from the pumping wavelength when pumping at 1558.5 nm. Nonetheless, signatures of dispersive waves are present in combs generated in both cases (Figs. 5.5.2 and 5.5.3).

While the zero crossing occurs close to the 19th comb side-band in Fig. 5.5.1(b), its corresponding dispersive wave appears around the 40th sideband (Figs. 5.5.2(c,

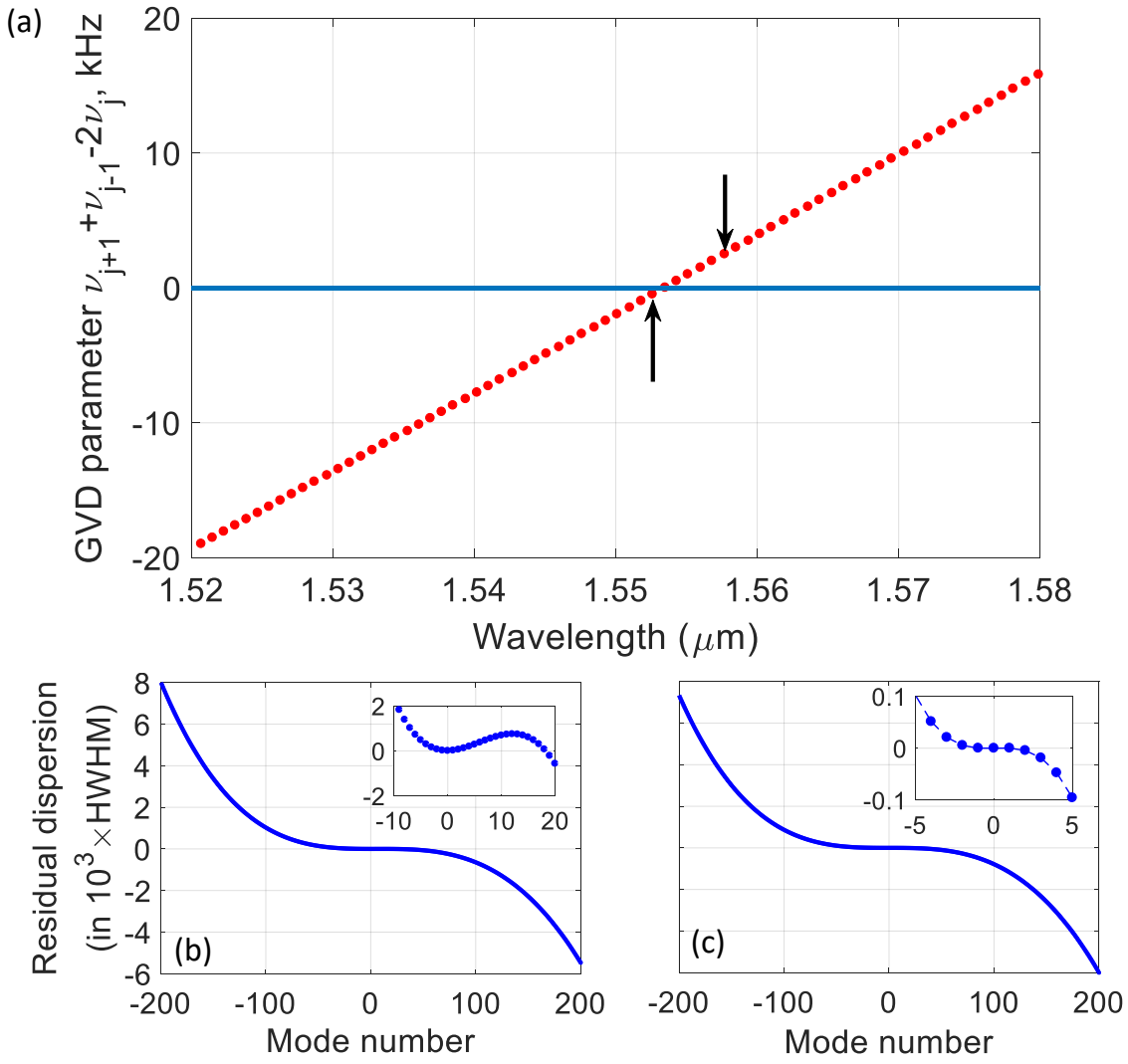

Fig. 5.5.1: Dispersion parameters for a magnesium fluoride crystalline resonator and the residual dispersion for two pumping points at 1553.5 nm and 1558.5 nm. These points are indicated by the two arrows. (a) Second-order GVD, D_2, of an MgF_2 spheroidal microresonator with FSR equal to 104 GHz. (b) and (c) depict the residual dispersion for the points shown by the arrows in panel (a) (1558.5 nm and 1553.5 nm, respectively). Third-order GVD is dominant in both cases. In the case shown in panel (c), the second-order GVD approaches zero such that there is no zero crossing for the residual dispersion except for the one at the pump position.

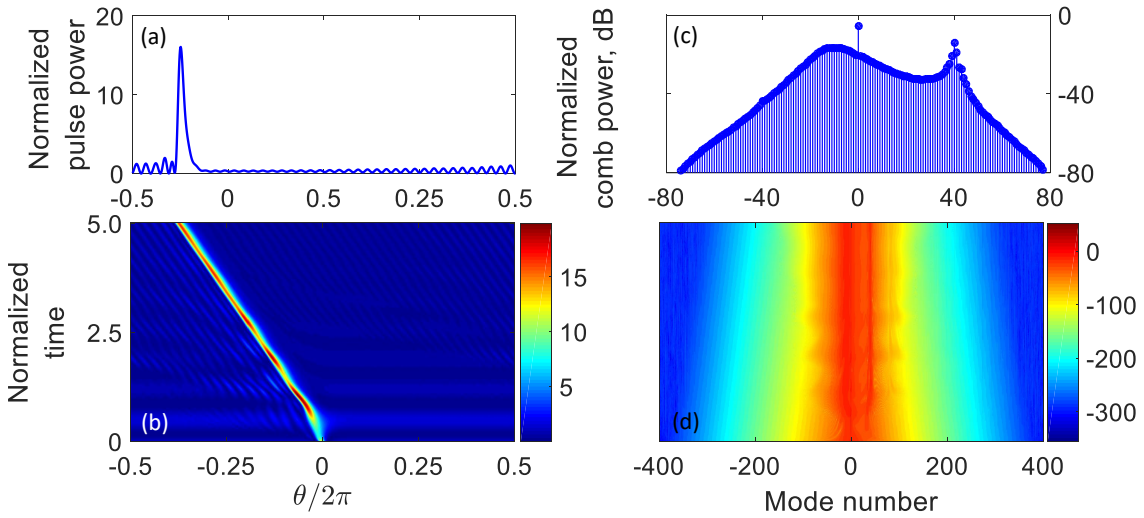

Fig. 5.5.2: Numerical simulations based on the LLE, performed for the residual dispersion curve shown in Fig. 5.5.1(b). (a, b) Intracavity pulse power and (c, d) comb power spectrum. As in the previous chapters, time is normalized to twice the cavity photon lifetime at the pumped resonance. Panels (a) and (c) correspond to the end of the simulation time in panels (b) and (d), respectively. The difference between the dispersive wave spectral position and the zero crossing in Fig. 5.5.1 is due to the influence of the pump and soliton power on j_{DW}; see Eq. (5.3.2). Parameters used in the numerical simulation are $d_2 = 2.98 \times 10^{-2}$, $d_3 = -5.00 \times 10^{-3}$, $d_4 = 1.02 \times 10^{-5}$, $d_5 = -3.01 \times 10^{-8}$, $F = 30$, and $\alpha = -19$. Normalized parameters are defined similar to previous chapters. See Section 2.2.3.

d)). This difference is attributed to the influence of the pump and soliton power on the spectral position of the dispersive wave discussed in the previous section (see Eq.(5.3.2), where addition of the soliton peak power shifts the residual dispersion curve up and hence moves the zero crossing further away from the pump). It is worth noting that even though there is no zero crossing (besides that at the pump position) for the comb pumped at 1553.5 nm (see the inset of Fig. 5.5.1(c)), a dispersive wave is still generated (as shown in Fig. 5.5.3). This observation, again, refers to the significant of the solitoin power term in the DW phase matching condition of Eq. (5.3.2).

I verify the dominance of the third-order GVD for the microcomb shown in Fig. 5.5.3 by changing the sign of all of the dispersion coefficients when integrating the LLE and observing that a similar pulse shape and comb power spectrum mirrored

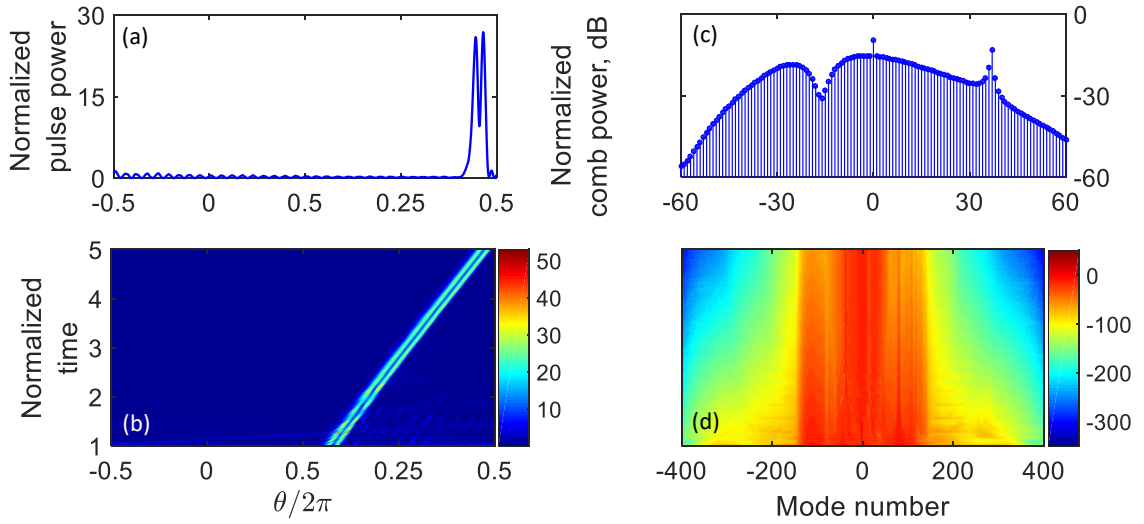

Fig. 5.5.3: Numerical simulations using the LLE, performed for the residual dispersion curve shown in Fig. 5.5.1(c). (a, b) Intracavity pulse power and (c, d) comb power spectrum. Note the dispersive wave emission even though there is no zero crossing on the residual dispersion curve of Fig. 5.5.1(c) besides that at the pump position. Phase matching is facilitated by the phase shift caused by soliton peak power; Eq. (5.3.2). Parameters used in the numerical simulation are $d_2 = -1 \times 10^{-4}$, $d_3 = -4.93 \times 10^{-3}$, $d_4 = 1.01 \times 10^{-5}$, $d_5 = -2.95 \times 10^{-8}$, $F = 40$, and $\alpha = -17$.

with respect to the vertical axes are still generated. In both examples shown in this section, soliton recoil leads to a shift of spectral peak with respect to the pump.

5.6 Effect of anomalous quartic dispersion

5.6.1 Microcombs in the presence of quadratic and quartic dispersion

Without careful dispersion engineering, purely quartic GVD is not normally seen in microresonators and in practice, a mixture of quadratic and quartic GVDs is more likely to be the case. In this section, I compare microcombs in the cases of resonators with pure quadratic, pure quartic, and mixed quadratic-quartic GVDs. Figure 5.6.1 illustrates three example microcombs and it is seen that a stable phase-locked comb is observable in all cases. Achieving steady state is confirmed by monitoring each pulse and noting that it preserves its shape while propagating for multiple cavity

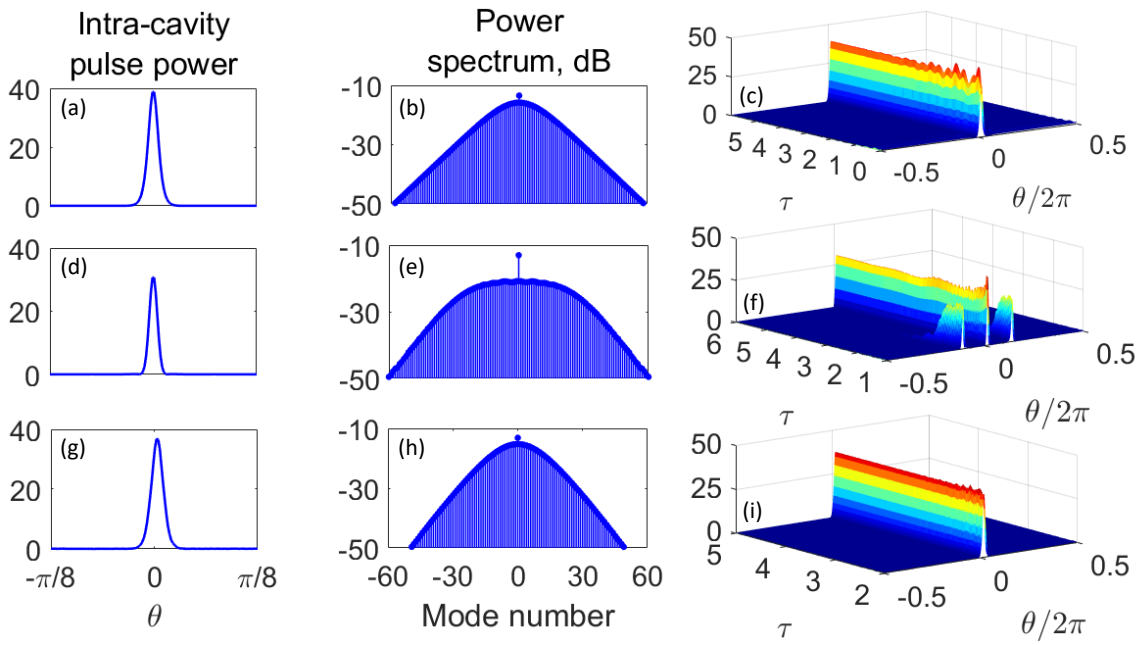

Fig. 5.6.1: Pulse shape (left column), comb spectrum (middle column), and oscillation settling (right panel) for the cases of pure quadratic (a-c), pure quartic (d-f), and mixed quadratic-quartic GVD (g-i). The pulse shapes are given over a quarter of the cavity round-trip time to better show the changes in the pulse duration and peak. The pulse in (a-c) is generated from an initial Gaussian pulse shape of comparable peak power as the final pulse, while the pulses in (d-f) and (g-i) are generated by high-intensity pulses as initial conditions. In (f) and (i) the oscillations of the large initial pulse over the first few normalized time units are not shown for improved visualization. The parameter values used are (a) $d_2 = 0.1$, $d_3 = 0$, $d_4 = 0$; (b) $d_2 = 0$, $d_3 = 0$, $d_4 = 2.98 \times 10^{-4}$; (c) $d_2 = 0.1$, $d_3 = 0$, $d_4 = 2.98 \times 10^{-4}$. For all three cases $F = 20$ and $\alpha = -19$.

ring-down times without oscillations in its width or peak power, as emphazied by Figs. 5.6.1(c), (f), (i). The total run-time was 20 cavity ring-down times (40 cavity photon lifetimes). It has been verified that a pure quartic anomalous GVD in an optical fiber system supports stable pulses of Gaussian shape [127]. The same pulse shape can be observed in microresonator with dominant quartic GVD, as noted in Fig. 5.6.1(b).

5.6.2 Simultaneous attractors in the presence of anomalous quadratic and quartic dispersion

I conclude this section by reporting a curious observation of simultaneous attractors in the presence of both quadratic and quartic GVDs (red curve in Fig. 5.6.2)[3]. Using hard excitation in the form of random initial conditions with power in the pumped mode and its immediate neighboring sidebands, it is observed that the solution of the coupled nonlinear Kerr-comb ODEs sometimes converges to the conventional solitonic comb (sech-like shape, Fig. 5.6.3(c)), and sometimes to another phase-locked frequency comb of Gaussian pulse shape (Fig. 5.6.3(a)). As shown in Fig. 5.6.3(b), the instantaneous phase of the Gaussian pulse varies significantly over its envelope. These two solutions have nearly the same comb spectrum envelopes, as shown in Fig. 5.6.4(a), where the comb spectra for these two pulses are overlaid on top of each other. To better demonstrate the difference between their pulse shapes, Fig. 5.6.4(b) shows pulse shapes in logarithmic scale, as well as Gaussian (for the red curve) and hyperbolic secant (for the blue curve) fits to the pulse peaks centered on zero. Looking at how the system approaches steady state, as an indicator, the temporal evolution of the first sideband for each of the two comb solutions (labeled a_1 in Fig. 5.6.5) is monitored. It is seen that the each comb sideband evolves with time and approaches its own attractor. The integration of the coupled wave ODE's shows that this solution is stable. The Gaussian solution is observed consistently in multiple independent rounds of solving the coupled wave equations with different hard excitation realizations.

In solving the LLE using the split-step Fourier transform method, it is observed that the Gaussian solution does not propagate long and is not stable. The reason is debatable but could be attributed to the implementation of the periodic bouandary conditions (PBC's). PBC's are automatically implemented when the fast Fourier

[3]The research described in this section was performed in collaboration with Dr. Andrey Matsko from OEwaves Inc.

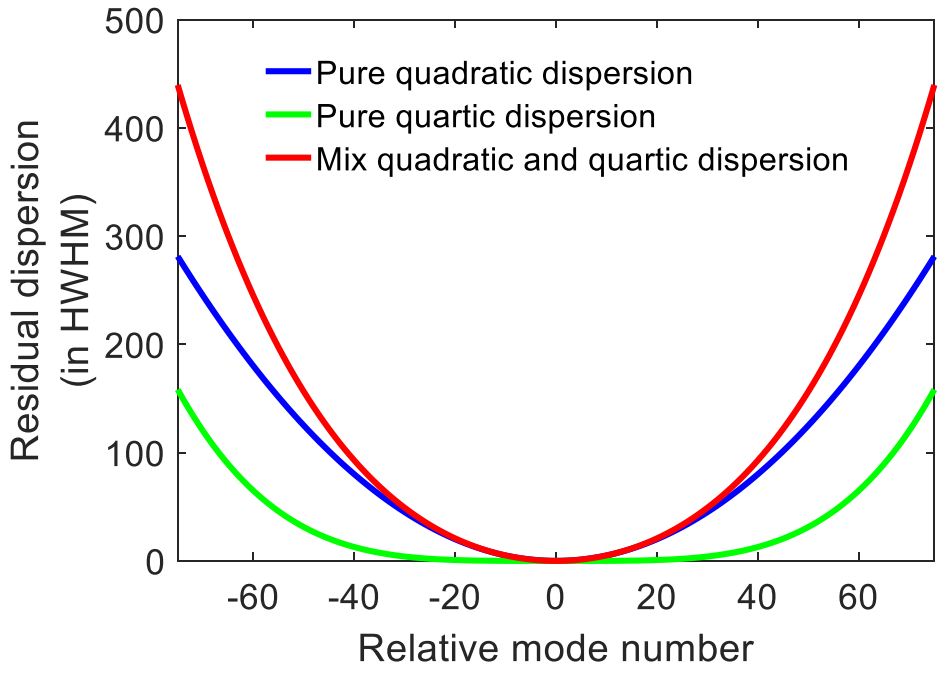

Fig. 5.6.2: Residual dispersion in units of the pumped mode half-width at half-maximum (HWHM). Three cases of pure second-order GVD, pure fourth-order GVD, and both second- and fourth-order GVD (with $D_3 = 0$) are depicted. The latter leads for a competition of two pulse types discussed in this section.

transform (FFT) is used in the linear half-step of the split-step technique for the evaluation of dispersion terms [131]. To investigate this effect, we consider an example in Fig. 5.6.6. In this figure, I show a smooth function sech(θ) and its first, second, and third derivatives found two ways: once from analytical expressions, Fig. 5.6.6(a), and once by FFT, Fig. 5.6.6(b). This function is smooth and has smooth finite-valued analytical derivatives. However, the derivatives found using FFT are ragged close to the edges. The raggedness is small for the first derivative but becomes very large for the third derivative. The reason is the lack of smoothness at the edges for the function and the jump at those edges in its first derivative. In Fig. 5.6.7, I also show the difference between the two sets of derivatives (in logarithmic scale) which clearly depicts enhanced error for higher-order derivatives.

The numerical error emphasized by Fig. 5.6.6 should not be confused with error

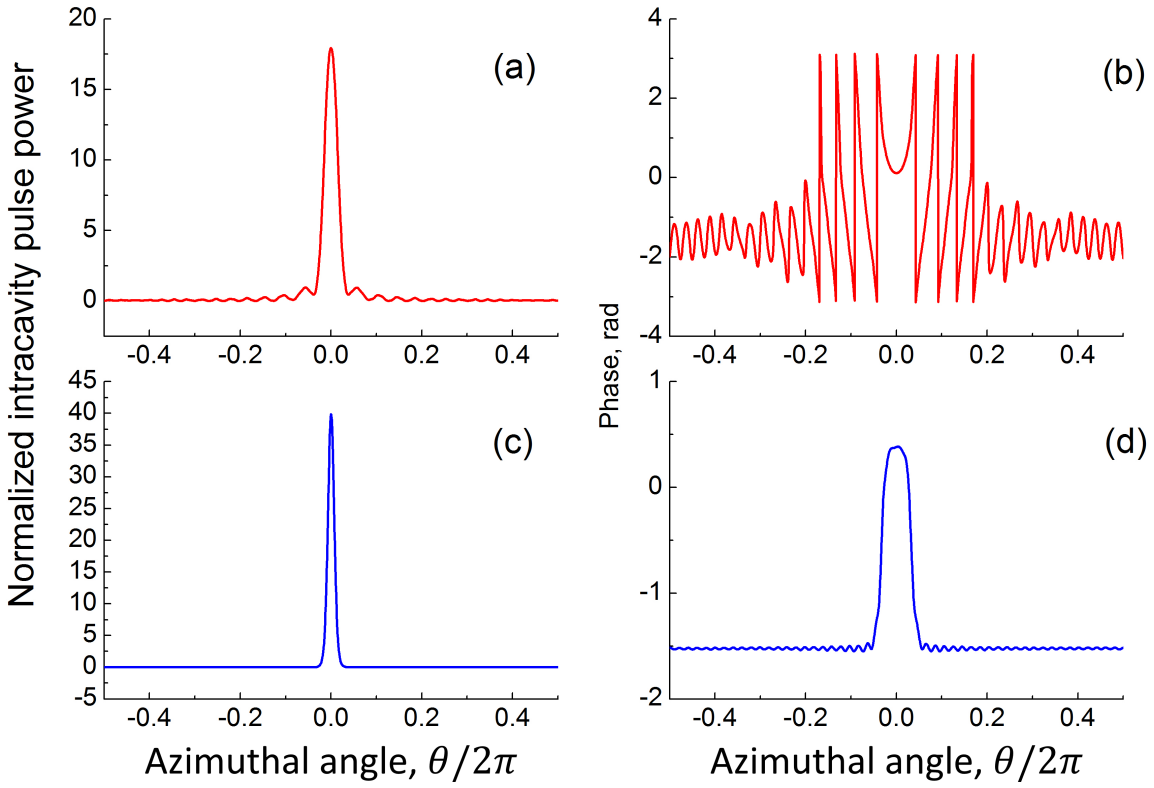

Fig. 5.6.3: Two competing pulses observed in the presence of both anomalous quadratic and quartic GVD. One of these pulses has a Gaussian shape (a) while the other is sech-like (solitonic). The instantaneous phases of these two pulses are very different, as shown in (b) and (d). Their power spectrum envelopes are, however, almost identical (Fig. 5.6.3(a)). System parameters are $d_2 = -0.1$, $d_3 = 0$, $d_4 = -1.2 \times 10^{-4}$, $F = 10$, $\alpha = -20.7$.

introduced from splitting the integration step into separate propagation under the linear and nonlinear operators (as detailed in Sec. 2.4 of [68]). In our split-step integration of the LLE we have reduced the integration step (in the slow time for the two-time-scale formulation or the evolution time in the time-azimuthal angle formulation) in a range from 0.02 to 10^{-6} (one millionth) of the normalized time. Yet, the Gaussian-shaped pulse has not survived. The error caused by FFT creeps in as reduced smoothness of the derivatives and becomes more deleterious for higher-order derivatives.

A question may naturally arise here: will increasing the number of point along the horizontal axis (and the number of points used in the calculation of the FFT)

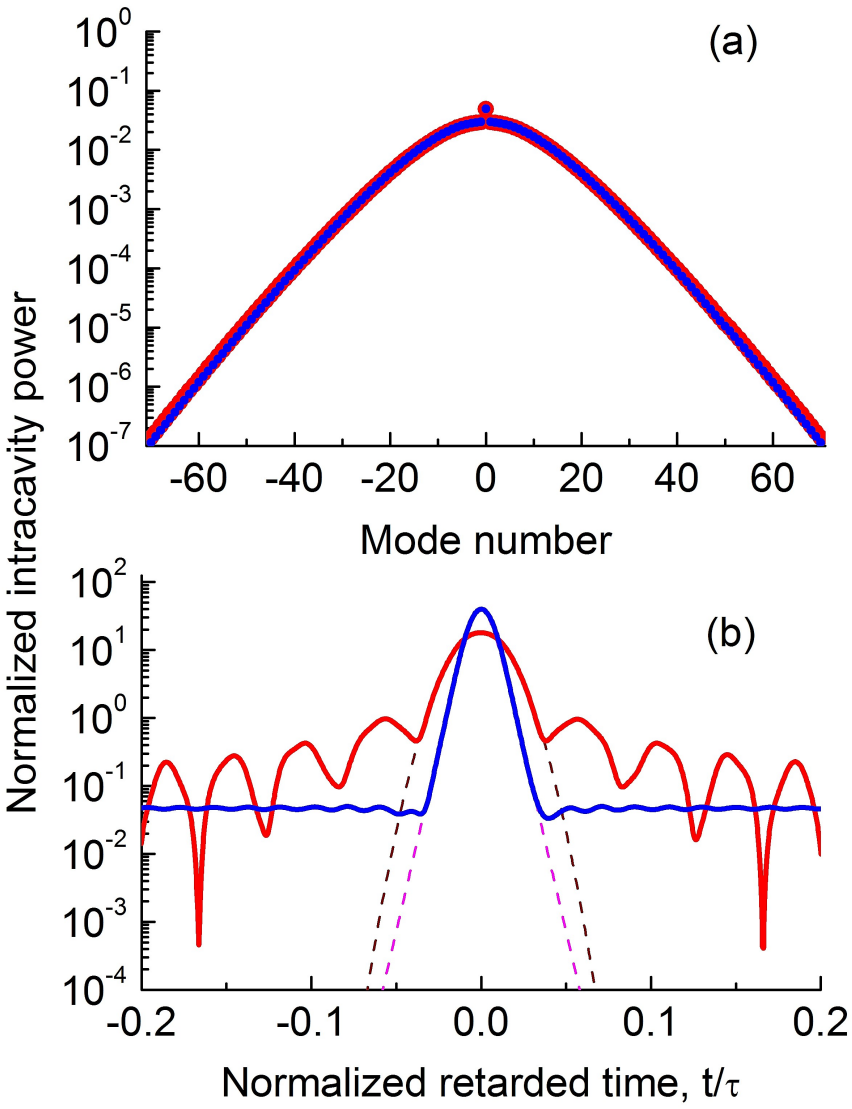

Fig. 5.6.4: Two competing phase-locked combs observed in the case of the presence of both quadratic and quartic GVDs for the residual dispersion curve shown in Fig. 5.6.2 (red curve). (a) Two mode-locked frequency combs can be excited in the resonator. These two comb spectra are overlaid, and are seen to be almost identical. (b) Two different pulses, one Gaussian (red) and the other sech-like (blue), can be generated for the comb power spectrum of (a).

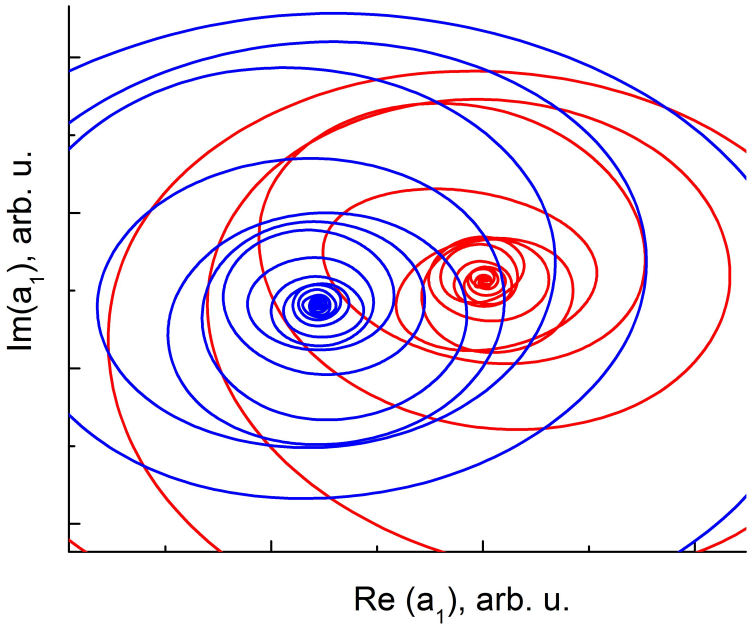

Fig. 5.6.5: There are two stable attractors for the combs shown in Fig. 5.6.4, as traced here by looking at the immediate sideband of the pumped mode. The system reaches the steady state within several ring-down times for both pulses.

lead to the reduction of the error close to the boundaries? In Fig. 5.6.8, the number of points along the horizontal axis θ and the number of points in evaluating FFT has increased from 2^{10} (top row) to 2^{14} (bottom row). Please note that this eight-fold increase has not led to reduction of error.

While the foregoing argument suggests that the origin of the discrepancy (Gaussian solution propagating stably in the coupled-wave equation but not in the split-step Fourier transform integration of the LLE) could lie in the fact that periodic boundary conditions may not properly be implemented in the coupled mode equations. On the other hand, the coupled-wave equations are written based on frequency domain variables and the periodic boundary conditions are not relevant for these variables (complex-valued comb teeth amplitudes). In fact, while it is known that spectral methods (such as the FFT) are suited for smooth functions [131], it has been noted that even when periodic boundary conditions are enforced, different implementations

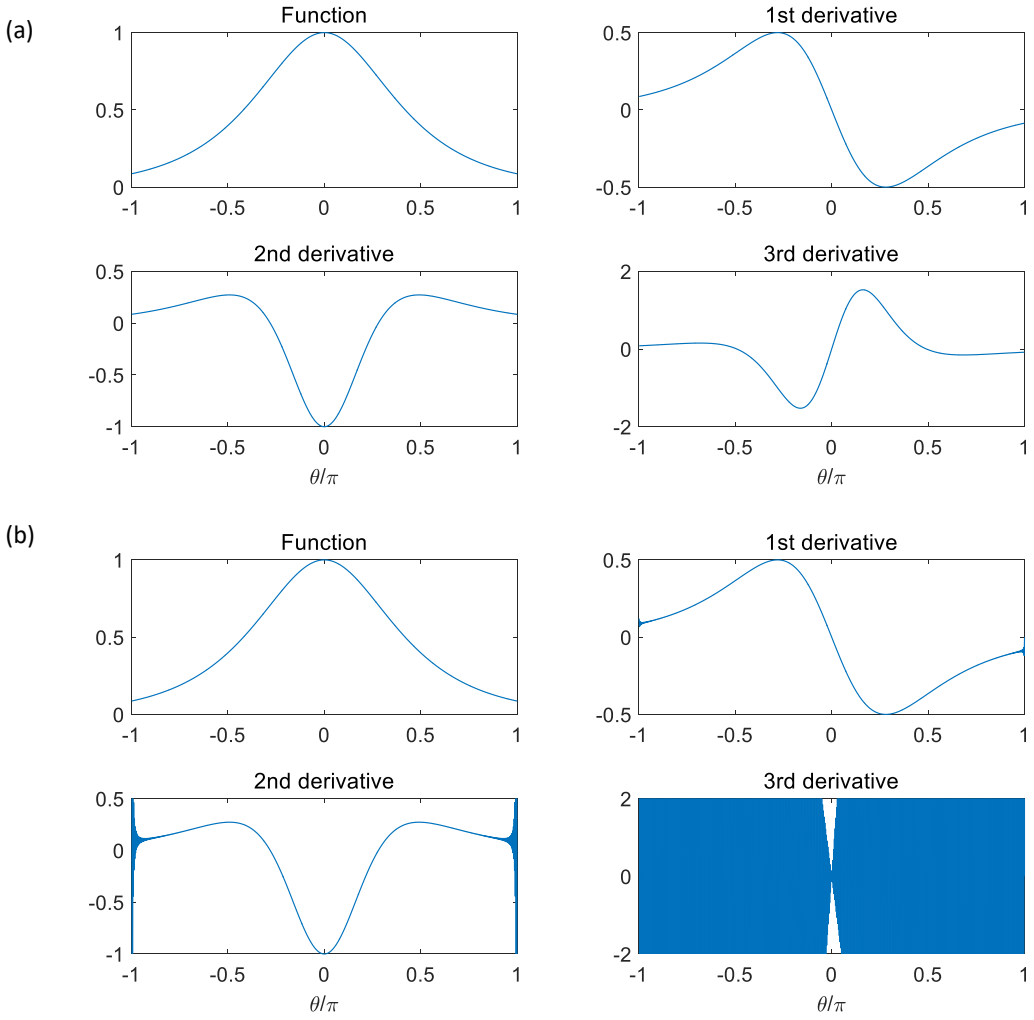

Fig. 5.6.6: Derivatives of a smooth function, sech(·), calculated numerically using FFT, which shows the influence of periodic boundary conditions in this spectral method. Here, the smooth function sech(θ) and its first, second, and third derivatives found two ways: (a) from analytical expressions, and (b) using FFT. This function is smooth and has smooth finite-valued analytical derivatives. Yet, the derivatives found using FFT are ragged, more pronouncedly close to the edges. The raggedness is small for the first derivative but becomes very large for the third derivative. The observed error originates from the fact that the function used in this example is not smooth at the edges of the horizontal axis or, equivalently, is not periodic in θ.

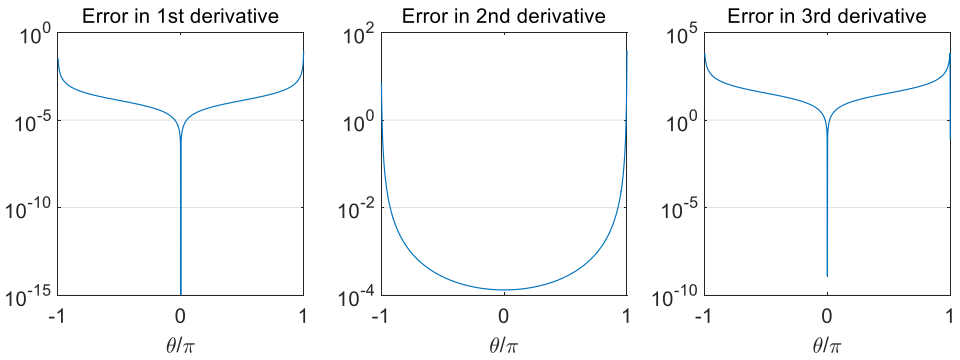

Fig. 5.6.7: The numerical error defined as the absolute value of the difference between the analytical derivatives and the derivatives found using FFT. See Fig. 5.6.6.

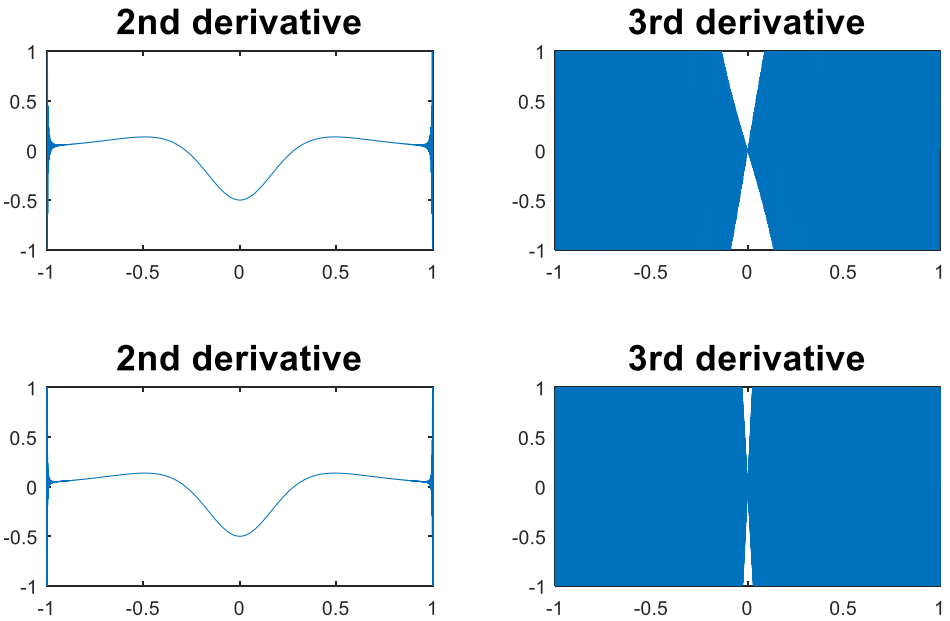

Fig. 5.6.8: Effect of increasing the number of points on the numerical error caused by FFT. Here, the number of points along the horizontal axis θ and the number of points in evaluating FFT has been increased from 1024 (top row) to 16384 (bottom row). It is seen that this sixteen-fold increase does not lead to reduction of error.

of the linear half-step (e.g., based on finite difference discretization and FFT) demonstrate different instabilities [132, 133]. While I have presented a tentative explanation in this sections, identifying the root of this discrepancy is worth further investigation.

5.7 Broadband NIR combs in CaF_2 for optical clock applications

In this final section of this chapter, I present near-IR (NIR) microcombs based on dispersion engineered crystalline CaF_2 microresonators[4]. These combs are primarily intended for use in optical atomic clocks [134, 135]. Two lasers will be locked to the D_1 and D_2[5] transitions of rubidium, ^{87}Rb, using the Pound-Drever-Hall (PDH) technique [118]. These two lasers are then used to stabilize the microcomb by locking two comb lines to them. When the comb is stabilized, it can be used for frequency and time measurement.

Generation of optical frequency combs in the visible and NIR range of the electromagnetic frequency spectrum is particularly challenging. The reason is that the generation of stable broadband combs corresponding to bright solitons requires anomalous dispersion while all material platforms currently in use for comb generation have large normal dispersion in this regime. Different approaches have been tried to achieve anomalous dispersion at short wavelengths close to the visible, for instance, through waveguide cross-section optimization, covering the resonator with a proper cladding layer, use of layered waveguides, and coupled resonators [44, 136–143]. These techniques suffer from some limitations, e.g., fail at shorter wavelengths where normal GVD is large, cannot provide broadband anomalous dispersion, or introduce large

[4]The modal resonance frequencies used in the calculation of dispersion parameters in this section were provided by Dr. Anatoliy Savchenkov from OEwaves Inc.

[5]D_1 and D_2 in this context should not be confused with the resonator FSR and second-order dispersion coefficient.

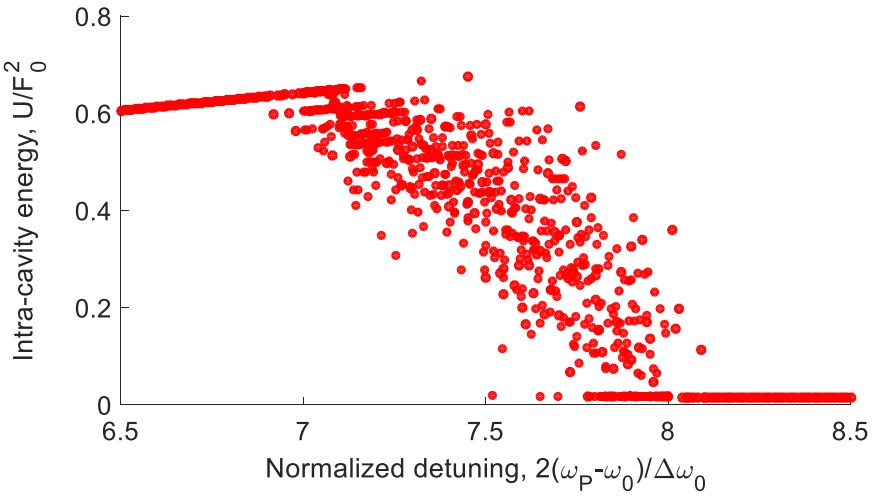

Fig. 5.7.1: Total comb power vs. pump-resonance detuning for a CaF_2 resonator with normal dispersion pumped at 795 nm. The dynamic range of the pump laser frequency is close to one half-width at half-maximum of the resonator linewidth, between 7 and 8 normalized detuning values. The upper branch corresponds to the larger of two bistable constant intra-cavity power levels while the lower branch is the smaller of these values. Between these two values, different dark solitons with different comb power levels are possible.

propagation losses. Additionally, the techniques based on coupled resonators are difficult to implement in crystalline resonators. Crystalline resonators are currently the major resonator types in use in commercial products.

It is worth noting that conversion efficiency (the ratio of the pump power converted to comb sideband frequencies) is higher in the normal dispersion optical frequency combs compared with those generated in the anomalous dispersion regime [141]. However, the dynamic range for the pump laser frequency is much smaller in normal dispersion compared to anomalous. For example, for a resonator with $Q_L = 10^8$, $d_2 = 0.1392$ ($D = -83.429$ ps/(nm km), bulk CaF_2 pumped at 795 nm) and with $F = 3.47$ (20 mW of input power), the detuning range over which dark solitons can be stably generated is about one half-width at half-maximum of the resonator linewidth, as seen in Fig. 5.7.1. This small dynamic range makes experimental demonstrations challenging. In comparison, pump laser dynamic range is tens of HWHM values in

the anomalous dispersion regime [143]. As a result, for practical purposes it is necessary to engineer resonator geometry to achieve anomalous dispersion in the visible and NIR wavelength range.

With the optical atomic clock application in mind, the resonator dispersion and microcomb parameters (pump-resonance detuning, pump power, and coupling Q) have been optimized under the following practical constraints:

- The comb should cover the two rubidium transitions at 780 nm and 795 nm. This coverage will allow locking two comb lines to two external lasers which are, in turn, locked to the rubidium atom. Comb sideband power can usually be measured reliably if it is above -80 dB.

- Pump laser should be at one of the above two wavelengths. This is particularly advantageous because comb power is usually largest close to the pump.

- The laser pump power should not exceed 40 mW. This requirement is based on the experimental setup which dictates the amount of power which could be coupled into the resonator.

- Comb FSR should not exceed 25 GHz, so that two adjacent comb teeth can be demodulated on a photodetector.

Different resonator geometries and sizes with different pump parameters have been investigated. The comb is pumped at 780 nm, but pumping at 795 nm is also possible as it meets the above criteria. One example of the different generated combs with one of the resonator dispersion parameters studied is shown in Fig. 5.7.2. For this resonator, $Q_{\mathrm{L}} = 10^8$. The upper panel (a) depicts the residual dispersion while the lower panel (b) shows different stable comb power spectra for various choices of pump-resonance detuning and pump power.

The example shown in Fig. 5.7.2 highlights the difficulty of achieving a broadband comb covering 780 nm and 790 nm with power levels which could be measured using available equipment. Below, I summarize parameters for the optimized CaF_2

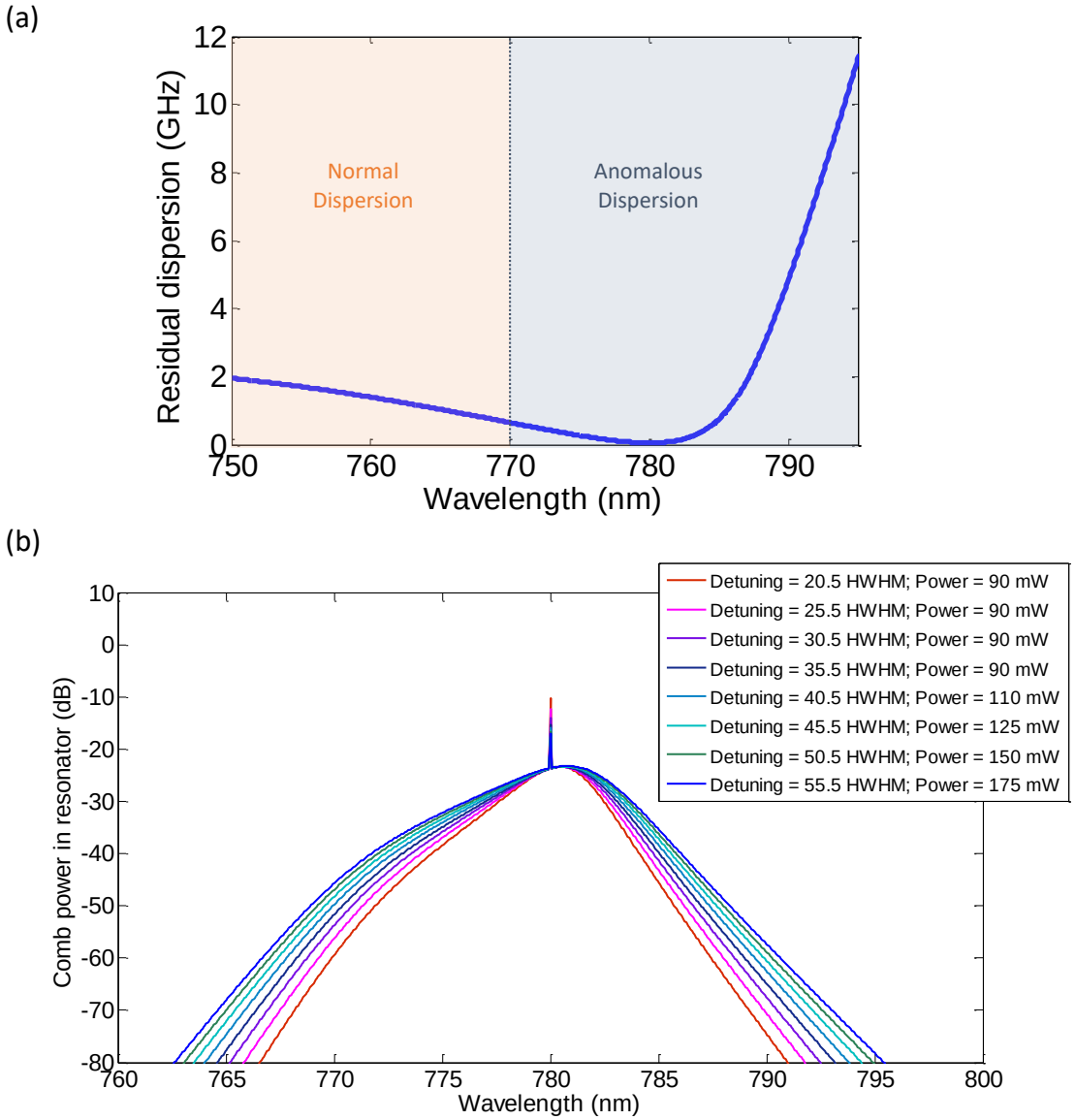

Fig. 5.7.2: Comb generation using a CaF_2 resonator for use in a rubidium-based atomic optical clock. The loaded quality factor is 10^8. (a) Residual (or integrated) dispersion for pumping at $\lambda_P = 780$ nm. (b) Comb power spectra for different pump parameters. This example highlights the difficulty of achieving a broadband comb covering 780 nm and 790 nm with power levels which could be measured using available equipment.

resonator and pump which can fulfill the requirements mentioned above.

Pump power: 15 mW

Detuning: 6×HWHM

$Q_{\mathrm{L}} = 1 \times 10^8$ or $\Delta\omega_{j_0} = 2 \times \mathrm{HWHM} = 3.84$ MHz

Resonator diameter: 3.15 mm

$Q_{\mathrm{i}} = 1 \times 10^{10}$

$D_2 = 2\pi \times (870.67)$ rad/sec

$D_3 = 2\pi \times (-6.59)$ rad/sec

$D_4 = 2\pi \times (-0.0275)$ rad/sec

$D_5 = 2\pi \times (3.25 \times 10^{-5})$ rad/sec

$D_6 = 2\pi \times (1.45 \times 10^{-7})$ rad/sec

The residual dispersion and second-order GVD of this winning resonator are shown in Fig. 5.7.3. The pumping wavelength of 780 is close to the zero GVD point and as a result a dispersive wave is expected to be emitted in the generated micrcomb spectrum. The intra-cavity pulse and its power spectrum are shown in Fig. 5.7.3, where the expected DW emission is observed as well. In the inset of panel (a) in this figure, I show the pulse shape which consists of a sharp pulse atop a modulated background, a signature of a comb with a dispersive wave. Figure 5.7.5 depicts the power spectrum as a function of wavelength, which confirms that the generated microcomb covers the spectrum from 780 nm to 795 nm with detectable power level. The stability of the comb is confirmed through propagating it over many ring-down times, as seen in Fig. 5.7.6.

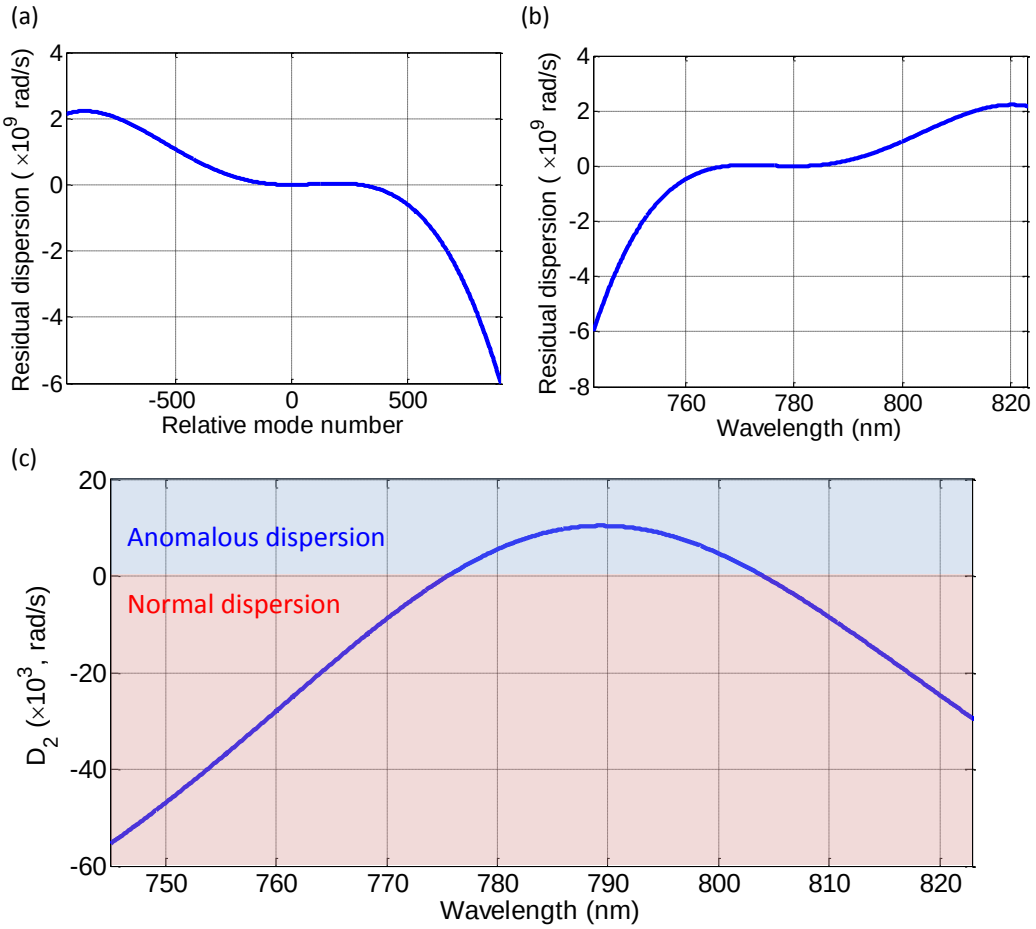

Fig. 5.7.3: Residual (or integrated) dispersion curve vs. relative mode number (a) and wavelength (b), as well as second-order dispersion (D_2) (c) for a realistic crystalline CaF_2 resonator in the near-IR regime designed for use in an atomic optical clock. This crystalline resonator has a diameter of 3.15 mm.

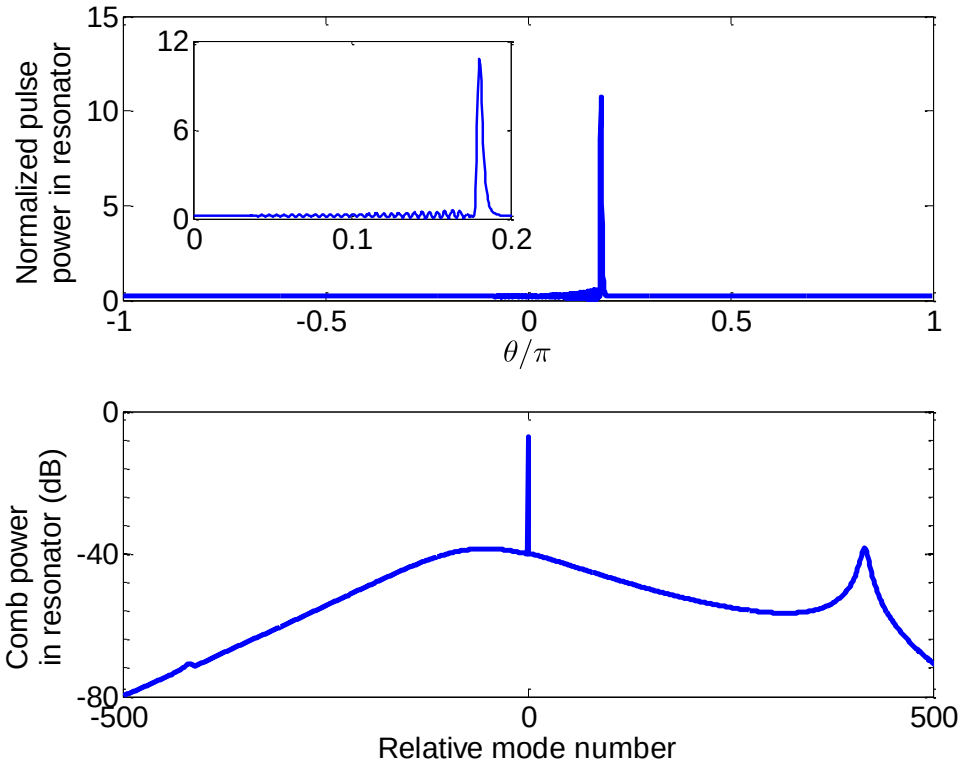

Fig. 5.7.4: The microcomb generated with the resonator described in Fig. 5.7.3. The utilized pump power is 15 mW and the pump-resonance detuning is 6×HWHM. The upper panel is the intra-cavity pulse and the lower panel shows the comb power spectrum

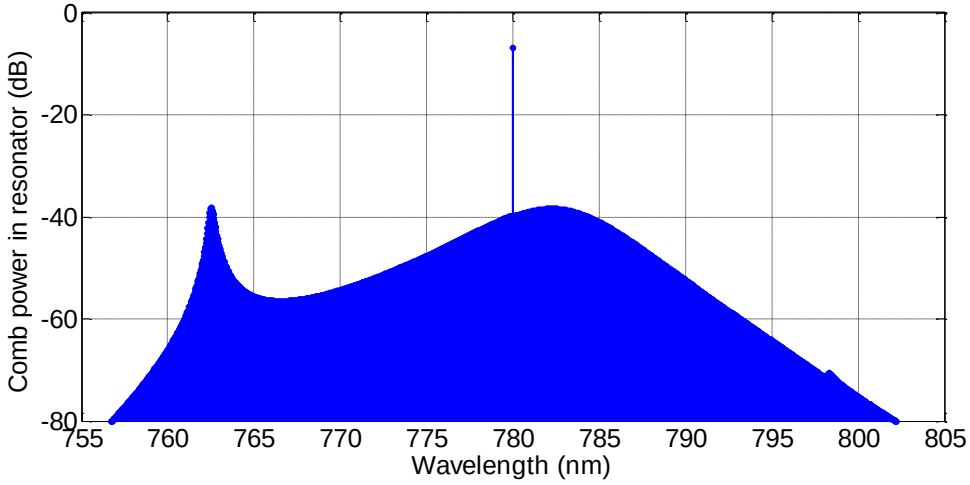

Fig. 5.7.5: Power spectrum vs. wavelength for the comb shown in Fig. 5.7.4. The generated microcomb has a span of more than 40 nm and covers 795 nm with detectable power.

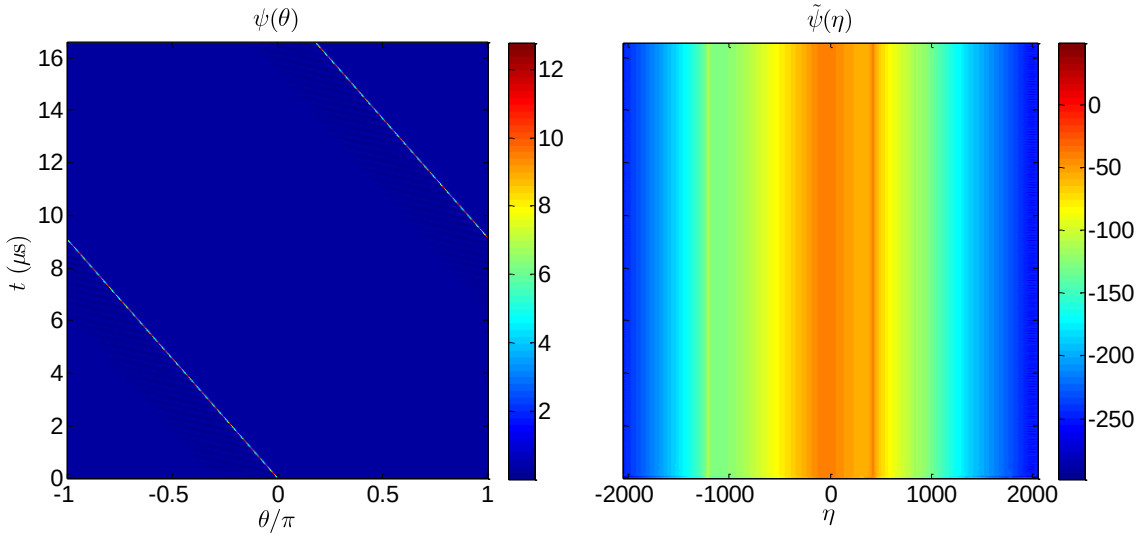

Fig. 5.7.6: The generated comb is stable as evidenced by the spectrograms shown here. The left panel shows the intra-cavity pulse while the right panel is the power spectrum.

CHAPTER 6
THESIS CONTRIBUTIONS

Below, I summarize the contributions of this thesis.

Chapters 2 and 3

A novel reduced model explaining phase-locking and synchronization phenomena in optical frequency combs generated in Kerr-nonlinear resonators is developed. It is applicable to hyperparametric oscillations (Turing patterns) seeded by vacuum fluctuations through modulational instability and to dispersive Kerr solitons. As saturable absorbers can be approximated with cubic (Kerr) nonlinearity, this model applies also to mode-locked lasers with saturable absorber. The propose phase locking model is the first to link optical pulse formation in a nonlinear process subject to the conservation of energy and momentum to synchronization phenomena. Stability of frequency combs is analyzed through the introduced model and the influence of power specturm on comb stablity is highlighted. Based on the understanding gained by this model, a simple and intuitive explanation of phase steps observed in recent microcomb measurements [40] is presented.

Chapter 4

An innovative technique for deterministic single soliton generation in microresonator-based optical frequency combs is introduced and analyzed. It is shown that this technique enhances pulse stability and can be used for manipulation of pulse arrival time at the output port. The theoretical framework presented in this chapter has explained some experiments in fiber cavities which preceded this work [109] and has recently been successfully implemented in crystalline MgF_2 resonators [48].

Chapter 5

A detailed study of the influence of higher-order group velocity dispersion (GVD)

in microcombs has been presented. The influence of higher-order dispersion in transferring the pump power and frequency noise to the microcomb repetition rate is explained. It is shown that resonators with quartic GVD support Gaussian pulses. Finally, record broadband near-infra-red (NIR) optical frequency combs based on realistic crystalline calcium fluoride (CaF_2) resonators and experimentally feasible pump parameters are presented. Such broadband microcombs are particularly designed for application in rubidium-based atomic optical clocks.

REFERENCES

[1] T. J. Kippenberg, R. Holzwarth, and S. Diddams, "Microresonator-based optical frequency combs," *Science*, vol. 332, no. 6029, pp. 555–559, 2011.

[2] N. R. Newbury, "Searching for applications with a fine-tooth comb," *Nat. Photon.*, vol. 5, no. 4, pp. 186–188, 2011.

[3] A. V. Oppenheim, A. S. Willsky, and S. H. Nawab, *Signals and systems*. Prentice-Hall Englewood Cliffs, NJ.

[4] S. T. Cundiff, "Phase stabilization of ultrashort optical pulses," *Journal of Physics D: Applied Physics*, vol. 35, no. 8, p. R43, 2002.

[5] T. Udem, R. Holzwarth, and T. W. Hänsch, "Optical frequency metrology," *Nature*, vol. 416, no. 6877, pp. 233–237, 2002.

[6] S. T. Cundiff and J. Ye, "Colloquium: Femtosecond optical frequency combs," *Rev. Mod. Phys.*, vol. 75, no. 1, p. 325, 2003.

[7] T. W. Hänsch, "Nobel lecture: passion for precision," *Rev. Mod. Phys*, vol. 78, no. 4, pp. 1297–1309, 2006.

[8] M. Niering, R. Holzwarth, J. Reichert, P. Pokasov, T. Udem, M. Weitz, T. Hänsch, P. Lemonde, G. Santarelli, M. Abgrall, *et al.*, "Measurement of the hydrogen 1 s-2 s transition frequency by phase coherent comparison with a microwave cesium fountain clock," *Phys. Rev. Lett.*, vol. 84, no. 24, p. 5496, 2000.

[9] S. Diddams, T. Udem, J. Bergquist, E. Curtis, R. Drullinger, L. Hollberg, W. Itano, W. Lee, C. Oates, K. Vogel, *et al.*, "An optical clock based on a single trapped 199hg+ ion," *Science*, vol. 293, no. 5531, pp. 825–828, 2001.

[10] P. A. Franken, A. E. Hill, C. W. Peters, and G. Weinreich, "Generation of optical harmonics," *Phys. Rev. Lett.*, vol. 7, no. 4, p. 118, 1961.

[11] P. N. Butcher and D. Cotter, *The elements of nonlinear optics*. Cambridge University Press, 1991.

[12] P. D. Drummond and M. Hillery, *The quantum theory of nonlinear optics*. Cambridge University Press, 2014.

[13] K. J. Vahala, "Optical microcavities," *Nature*, vol. 424, no. 6950, pp. 839–846, 2003.

[14] W. Liang, D. Eliyahu, V. Ilchenko, A. Savchenkov, A. Matsko, D. Seidel, and L. Maleki, "High spectral purity kerr frequency comb radio frequency photonic oscillator," *Nat. Commun.*, vol. 6, 2015.

[15] S. Hendrickson, A. Foster, R. Camacho, and B. Clader, "Integrated nonlinear photonics: emerging applications and ongoing challenges [invited]," *Journal of the Optical Society of America B Optical Physics*, vol. 31, p. 3193, 2014.

[16] J. L. O'Brien, A. Furusawa, and J. Vučković, "Photonic quantum technologies," *Nat. Photon.*, vol. 3, no. 12, pp. 687–695, 2009.

[17] T. J. Kippenberg and K. J. Vahala, "Cavity optomechanics: back-action at the mesoscale," *science*, vol. 321, no. 5893, pp. 1172–1176, 2008.

[18] K. Nozaki, T. Tanabe, A. Shinya, S. Matsuo, T. Sato, H. Taniyama, and M. Notomi, "Sub-femtojoule all-optical switching using a photonic-crystal nanocavity," *Nat. Photon.*, vol. 4, no. 7, pp. 477–483, 2010.
[19] V. R. Almeida, C. A. Barrios, R. R. Panepucci, M. Lipson, M. A. Foster, D. G. Ouzounov, and A. L. Gaeta, "All-optical switching on a silicon chip," *Opt. Lett.*, vol. 29, no. 24, pp. 2867–2869, 2004.
[20] J. Huang and P. Kumar, "Observation of quantum frequency conversion," *Phys. Rev. Lett.*, vol. 68, no. 14, p. 2153, 1992.
[21] M. G. Raymer and K. Srinivasan, "Manipulating the color and shape of single photons," *Physics Today*, vol. 65, no. 11, pp. 32–37, 2012.
[22] R. W. Boyd, *Nonlinear Optics*. Academic Press, 2008.
[23] F. Vollmer and S. Arnold, "Whispering-gallery-mode biosensing: label-free detection down to single molecules," *Nat. Methods*, vol. 5, no. 7, pp. 591–596, 2008.
[24] V. Vassiliev, V. Velichansky, V. Ilchenko, M. Gorodetsky, L. Hollberg, and A. Yarovitsky, "Narrow-line-width diode laser with a high-q microsphere resonator," *Optics Communications*, vol. 158, no. 1, pp. 305–312, 1998.
[25] S. Spillane, T. Kippenberg, and K. Vahala, "Ultralow-threshold raman laser using a spherical dielectric microcavity," *Nature*, vol. 415, no. 6872, pp. 621–623, 2002.
[26] A. Savchenkov, A. Matsko, and L. Maleki, "On frequency combs in monolithic resonators," *Nanophotonics*, vol. 5, no. 2, pp. 363–391, 2016.
[27] Y. K. Chembo, "Kerr optical frequency combs: theory, applications and perspectives," *Nanophotonics, accepted for publication*, 2015.
[28] T. J. A. Kippenberg, *Nonlinear optics in ultra-high-Q whispering-gallery optical microcavities*. PhD thesis, California Institute of Technology, 2004.
[29] L.-S. Collot, V. Lefevre-Seguin, M. Brune, J. Raimond, and S. Haroche, "Very high-q whispering-gallery mode resonances observed on fused silica microspheres," *Europhys. Lett.*, vol. 23, no. 5, p. 327, 1993.
[30] X. Yi, Q.-F. Yang, K. Y. Yang, M.-G. Suh, and K. Vahala, "Soliton frequency comb at microwave rates in a high-q silica microresonator," *Optica*, vol. 2, no. 12, pp. 1078–1085, 2015.
[31] Q. Li, A. A. Eftekhar, P. Alipour, A. H. Atabaki, S. Yegnanarayanan, and A. Adibi, "Low-loss microdisk-based delay lines for narrowband optical filters," *IEEE Photonics Technology Letters*, vol. 24, no. 15, pp. 1276–1278, 2012.
[32] Q. Li, T. C. Briles, D. Westly, J. Stone, R. Ilic, S. Diddams, S. Papp, and K. Srinivasan, "Octave-spanning microcavity kerr frequency combs with harmonic dispersive-wave emission on a silicon chip," in *Frontiers in Optics*, pp. FW6C–5, Optical Society of America, 2015.
[33] D. Armani, T. Kippenberg, S. Spillane, and K. Vahala, "Ultra-high-q toroid microcavity on a chip," *Nature*, vol. 421, no. 6926, pp. 925–928, 2003.
[34] T. Herr, V. Brasch, J. D. Jost, I. Mirgorodskiy, G. Lihachev, M. L. Gorodetsky, and T. J. Kippenberg, "Mode spectrum and temporal soliton formation in optical microresonators," *Phys. Rev. Lett.*, vol. 113, no. 12, p. 123901, 2014.
[35] C. Bao, H. Taheri, L. Zhang, A. Matsko, Y. Yan, P. Liao, L. Maleki, and A. E.

Willner, "High-order dispersion in kerr comb oscillators," *Journal of the Optical Society of America B (JOSA B), under review*, 2016.
[36] I. S. Grudinin and N. Yu, "Dispersion engineering of crystalline resonators via microstructuring," *Optica*, vol. 2, no. 3, pp. 221–224, 2015.
[37] K. Saha, Y. Okawachi, B. Shim, J. S. Levy, R. Salem, A. R. Johnson, M. A. Foster, M. R. Lamont, M. Lipson, and A. L. Gaeta, "Modelocking and femtosecond pulse generation in chip-based frequency combs," *Opt. Express*, vol. 21, no. 1, pp. 1335–1343, 2013.
[38] H. Lee, T. Chen, J. Li, K. Y. Yang, S. Jeon, O. Painter, and K. J. Vahala, "Chemically etched ultrahigh-q wedge-resonator on a silicon chip," *Nat. Photon.*, vol. 6, no. 6, pp. 369–373, 2012.
[39] J. Li, H. Lee, K. Y. Yang, and K. J. Vahala, "Sideband spectroscopy and dispersion measurement in microcavities," *Opt. Express*, vol. 20, no. 24, pp. 26337–26344, 2012.
[40] P. Del'Haye, A. Coillet, W. Loh, K. Beha, S. B. Papp, and S. A. Diddams, "Phase steps and resonator detuning measurements in microresonator frequency combs," *Nat. Commun.*, vol. 6, 2015.
[41] M. H. Dunn and M. Ebrahimzadeh, "Parametric generation of tunable light from continuous-wave to femtosecond pulses," *Science*, vol. 286, no. 5444, pp. 1513–1517, 1999.
[42] M. Soltani, *Novel integrated silicon nanophotonic structures using ultra-high Q resonators*. PhD thesis, Georgia Institute of Technology, 2009.
[43] M. A. Foster, A. C. Turner, M. Lipson, and A. L. Gaeta, "Nonlinear optics in photonic nanowires," *Opt. Express*, vol. 16, no. 2, pp. 1300–1320, 2008.
[44] J. Riemensberger, K. Hartinger, T. Herr, V. Brasch, R. Holzwarth, and T. J. Kippenberg, "Dispersion engineering of thick high-q silicon nitride ring-resonators via atomic layer deposition," *Opt. Express*, vol. 20, no. 25, pp. 27661–27669, 2012.
[45] S. Minissale, S. Yerci, and L. Dal Negro, "Nonlinear optical properties of low temperature annealed silicon-rich oxide and silicon-rich nitride materials for silicon photonics," *Applied Physics Letters*, vol. 100, no. 2, p. 021109, 2012.
[46] K. Y. Yang, K. Beha, D. C. Cole, X. Yi, P. Del'Haye, H. Lee, J. Li, D. Y. Oh, S. A. Diddams, S. B. Papp, *et al.*, "Broadband dispersion-engineered microresonator on a chip," *Nature Photonics*, vol. 10, no. 5, pp. 316–320, 2016.
[47] P. Del'Haye, O. Arcizet, M. L. Gorodetsky, R. Holzwarth, and T. J. Kippenberg, "Frequency comb assisted diode laser spectroscopy for measurement of microcavity dispersion," *Nature Photonics*, vol. 3, no. 9, pp. 529–533, 2009.
[48] V. Lobanov, G. Lihachev, N. Pavlov, A. Cherenkov, T. Kippenberg, and M. Gorodetsky, "Harmonization of chaos into a soliton in kerr frequency combs," *Optics Express*, vol. 24, no. 24, pp. 27382–27394, 2016.
[49] A. M. Turing, "The chemical basis of morphogenesis," *Philosophical Transactions of the Royal Society of London B: Biological Sciences*, vol. 237, no. 641, pp. 37–72, 1952.
[50] J. Pfeifle *et al.*, "Coherent terabit communications with microresonator kerr frequency combs," *Nat. Photon.*, vol. 8, no. 5, pp. 375–380, 2014.

[51] J. Pfeifle, A. Coillet, R. Henriet, K. Saleh, P. Schindler, C. Weimann, W. Freude, I. V. Balakireva, L. Larger, C. Koos, and Y. K. Chembo, "Optimally coherent kerr combs generated with crystalline whispering gallery mode resonators for ultrahigh capacity fiber communications," *Phys. Rev. Lett.*, vol. 114, no. 9, p. 093902, 2015.

[52] H. Taheri, A. A. Eftekhar, W. Kurt, and A. Ali, "Anatomy of phase locking in hyperparametric oscillations based on kerr nonlinearity," *IEEE Photonics Journal, under review*, 2016.

[53] A. A. Savchenkov, A. B. Matsko, V. S. Ilchenko, I. Solomatine, D. Seidel, and L. Maleki, "Tunable optical frequency comb with a crystalline whispering gallery mode resonator," *Phys. Rev. Lett.*, vol. 101, no. 9, p. 093902, 2008.

[54] T. Herr, V. Brasch, J. Jost, C. Wang, N. Kondratiev, M. Gorodetsky, and T. Kippenberg, "Temporal solitons in optical microresonators," *Nat. Photon.*, vol. 8, no. 2, pp. 145–152, 2014.

[55] V. Brasch, M. Geiselmann, T. Herr, G. Lihachev, M. Pfeiffer, M. Gorodetsky, and T. Kippenberg, "Photonic chip-based optical frequency comb using soliton cherenkov radiation," *Science*, vol. 351, no. 6271, pp. 357–360, 2016.

[56] I. Barashenkov and Y. S. Smirnov, "Existence and stability chart for the ac-driven, damped nonlinear schrödinger solitons," *Physical Review E*, vol. 54, no. 5, p. 5707, 1996.

[57] A. Matsko, A. Savchenkov, W. Liang, V. Ilchenko, D. Seidel, and L. Maleki, "Mode-locked kerr frequency combs," *Opt. Lett.*, vol. 36, no. 15, pp. 2845–2847, 2011.

[58] L. A. Lugiato and R. Lefever, "Spatial dissipative structures in passive optical systems," *Phys. Rev. Lett.*, vol. 58, no. 21, p. 2209, 1987.

[59] M. Haelterman, S. Trillo, and S. Wabnitz, "Dissipative modulation instability in a nonlinear dispersive ring cavity," *Optics Commun.*, vol. 91, no. 5, pp. 401–407, 1992.

[60] S. Coen, H. G. Randle, T. Sylvestre, and M. Erkintalo, "Modeling of octave-spanning kerr frequency combs using a generalized mean-field lugiato-lefever model," *Opt. Lett.*, vol. 38, no. 1, pp. 37–39, 2013.

[61] Y. K. Chembo and C. R. Menyuk, "Spatiotemporal lugiato-lefever formalism for kerr-comb generation in whispering-gallery-mode resonators," *Phys. Rev. A*, vol. 87, no. 5, p. 053852, 2013.

[62] T. S. Raju, C. N. Kumar, and P. K. Panigrahi, "On exact solitary wave solutions of the nonlinear schrödinger equation with a source," *Journal of Physics A: Mathematical and General*, vol. 38, no. 16, p. L271, 2005.

[63] W. H. Renninger and P. T. Rakich, "Closed-form solutions and scaling laws for kerr frequency combs," *Scientific reports*, vol. 6, 2016.

[64] P. Del'Haye, K. Beha, S. B. Papp, and S. A. Diddams, "Self-injection locking and phase-locked states in microresonator-based optical frequency combs," *Phys. Rev. Lett.*, vol. 112, no. 4, p. 043905, 2014.

[65] A. Coillet and Y. Chembo, "On the robustness of phase locking in kerr optical frequency combs," *Opt. Lett.*, vol. 39, no. 6, pp. 1529–1532, 2014.

[66] Y. H. Wen, M. R. Lamont, I. M. Kloumann, S. H. Strogatz, and A. L.

Gaeta, "Self-organization in soliton modelocked parametric frequency combs," *arXiv:1412.0119*, 2014.
[67] I. V. Barashenkov and E. V. Zemlyanaya, "Travelling solitons in the externally driven nonlinear schrödinger equation," *Journal of Physics A: Mathematical and Theoretical*, vol. 44, no. 46, p. 465211, 2011.
[68] G. P. Agrawal, *Nonlinear Fiber Optics*. Academic Press, 5th ed., 2013.
[69] Y. K. Chembo and N. Yu, "Modal expansion approach to optical-frequency-comb generation with monolithic whispering-gallery-mode resonators," *Phys. Rev. A*, vol. 82, no. 3, p. 033801, 2010.
[70] A. Coillet and Y. K. Chembo, "Routes to spatiotemporal chaos in kerr optical frequency combs," *Chaos: An Interdisciplinary Journal of Nonlinear Science*, vol. 24, no. 1, p. 013113, 2014.
[71] P. Del'Haye, A. Schliesser, O. Arcizet, T. Wilken, R. Holzwarth, and T. Kippenberg, "Optical frequency comb generation from a monolithic microresonator," *Nature*, vol. 450, no. 7173, pp. 1214–1217, 2007.
[72] A. B. Matsko, A. A. Savchenkov, D. Strekalov, V. S. Ilchenko, and L. Maleki, "Optical hyperparametric oscillations in a whispering-gallery-mode resonator: Threshold and phase diffusion," *Physical Review A*, vol. 71, no. 3, p. 033804, 2005.
[73] J. K. Jang, M. Erkintalo, S. G. Murdoch, and S. Coen, "Writing and erasing of temporal cavity solitons by direct phase modulation of the cavity driving field," *Opt. Lett.*, vol. 40, no. 20, pp. 4755–4758, 2015.
[74] H. Taheri, A. Eftekhar, K. Wiesenfeld, and A. Adibi, "Soliton formation in whispering-gallery-mode resonators via input phase modulation," *IEEE Photonics J.*, vol. 7, no. 2, pp. 1–9, 2015.
[75] P. Grelu and N. Akhmediev, "Dissipative solitons for mode-locked lasers," *Nat. Photon.*, vol. 6, no. 2, pp. 84–92, 2012.
[76] T. Herr, K. Hartinger, J. Riemensberger, C. Wang, E. Gavartin, R. Holzwarth, M. Gorodetsky, and T. Kippenberg, "Universal formation dynamics and noise of kerr-frequency combs in microresonators," *Nat. Photon.*, vol. 6, no. 7, pp. 480–487, 2012.
[77] C. Godey, I. V. Balakireva, A. Coillet, and Y. K. Chembo, "Stability analysis of the spatiotemporal lugiato-lefever model for kerr optical frequency combs in the anomalous and normal dispersion regimes," *Phys. Rev. A*, vol. 89, no. 6, p. 063814, 2014.
[78] G. Kozyreff, "Localized turing patterns in nonlinear optical cavities," *Physica D: Nonlinear Phenomena*, vol. 241, no. 10, pp. 939–946, 2012.
[79] A. V. Oppenheim and R. W. Schafer, *Discrete-time signal processing*. New Jersey, Printice Hall Inc, 1989.
[80] T. Hansson, D. Modotto, and S. Wabnitz, "On the numerical simulation of kerr frequency combs using coupled mode equations," *Opt. Commun.*, vol. 312, pp. 134–136, 2014.
[81] Y. K. Chembo, D. V. Strekalov, and N. Yu, "Spectrum and dynamics of optical frequency combs generated with monolithic whispering gallery mode resonators," *Phys. Rev. Lett.*, vol. 104, no. 10, p. 103902, 2010.

[82] S. Trillo and S. Wabnitz, "Dynamics of the nonlinear modulational instability in optical fibers," *Optics letters*, vol. 16, no. 13, pp. 986–988, 1991.
[83] T. Hansson, D. Modotto, and S. Wabnitz, "Dynamics of the modulational instability in microresonator frequency combs," *Physical Review A*, vol. 88, no. 2, p. 023819, 2013.
[84] E. D. Farnum and J. N. Kutz, "Dynamics of a low-dimensional model for short pulse mode locking," *Photonics*, vol. 2, no. 3, pp. 865–882, 2015.
[85] H. Taheri, A. A. Eftekhar, K. Wiesenfeld, and A. Adibi, "Anatomy of phase locking in parametric frequency combs," in *Frontiers in Optics 2015*, p. JW2A.12, Optical Society of America, 2015.
[86] R. Adler, "A study of locking phenomena in oscillators," *Proceedings of the IRE*, vol. 34, no. 6, pp. 351–357, 1946.
[87] H. Taheri, P. Del'Haye, A. A. Eftekhar, W. Kurt, and A. Ali, "Self-synchronization phenomena in the lugiato-lefever equation," *Physical Review A, under review*, 2016.
[88] H. Haken, *Synergetics: Introduction and Advanced Topics*. Springer-Verlag, 2004.
[89] N. Akhmediev and A. Ankiewicz, *Dissipative Solitons, Lecture Notes in Physics*, vol. 661. Springer, 2005.
[90] H. A. Haus, "Mode-locking of lasers," *IEEE J. Sel. Top. Quantum Electron.*, vol. 6, no. 6, pp. 1173–1185, 2000.
[91] A. B. Matsko, A. A. Savchenkov, V. S. Ilchenko, D. Seidel, and L. Maleki, "Hard and soft excitation regimes of kerr frequency combs," *Phys. Rev. A*, vol. 85, no. 2, p. 023830, 2012.
[92] W. Loh, P. Del'Haye, S. B. Papp, and S. A. Diddams, "Phase and coherence of optical microresonator frequency combs," *Phys. Rev. A*, vol. 89, no. 5, p. 053810, 2014.
[93] A. Pikovsky, M. Rosenblum, and J. Kurths, *Synchronization: a universal concept in nonlinear sciences*. Cambridge University Press, 2003.
[94] M. R. Lamont, Y. Okawachi, and A. L. Gaeta, "Route to stabilized ultrabroadband microresonator-based frequency combs," *Opt. Lett.*, vol. 38, no. 18, pp. 3478–3481, 2013.
[95] J. A. Jaramillo-Villegas, X. Xue, P.-H. Wang, D. E. Leaird, and A. M. Weiner, "Deterministic single soliton generation and compression in microring resonators avoiding the chaotic region," *Opt. Express*, vol. 23, no. 8, pp. 9618–9626, 2015.
[96] F. Leo, S. Coen, P. Kockaert, S.-P. Gorza, P. Emplit, and M. Haelterman, "Temporal cavity solitons in one-dimensional kerr media as bits in an all-optical buffer," *Nat. Photon.*, vol. 4, no. 7, pp. 471–476, 2010.
[97] S. H. Strogatz, "From kuramoto to crawford: exploring the onset of synchronization in populations of coupled oscillators," *Physica D*, vol. 143, no. 1, pp. 1–20, 2000.
[98] N. Akhmediev, A. Ankiewicz, J. Soto-Crespo, and J. M. Dudley, "Universal triangular spectra in parametrically-driven systems," *Physics Letters A*, vol. 375, no. 3, pp. 775–779, 2011.

[99] S. Coen and M. Erkintalo, "Universal scaling laws of kerr frequency combs," *Opt. Lett.*, vol. 38, no. 11, pp. 1790–1792, 2013.
[100] E. S. Lamb, D. C. Cole, P. Del'Haye, K. Y. Yang, K. J. Vahala, S. A. Diddams, and S. B. Papp, "Stabilizing multiple solitons in kerr microresonator frequency combs," in *Conference on Lasers and Electro-Optics*, p. SW1E.3, Optical Society of America, 2016.
[101] B. A. Malomed, "Variational methods in nonlinear fiber optics and related fields," *Progress in optics*, vol. 43, pp. 71–194, 2002.
[102] A. Gordon and B. Fischer, "Phase transition theory of many-mode ordering and pulse formation in lasers," *Phys. Rev. Lett.*, vol. 89, no. 10, p. 103901, 2002.
[103] A. B. Matsko and L. Maleki, "On timing jitter of mode locked kerr frequency combs," *Optics express*, vol. 21, no. 23, pp. 28862–28876, 2013.
[104] D. V. Strekalov and N. Yu, "Generation of optical combs in a whispering gallery mode resonator from a bichromatic pump," *Phys. Rev. A*, vol. 79, no. 4, p. 041805, 2009.
[105] S. B. Papp, P. Del'Haye, and S. A. Diddams, "Parametric seeding of a microresonator optical frequency comb," *Opt. Express*, vol. 21, no. 15, pp. 17615–17624, 2013.
[106] G. S. McDonald and W. Firth, "Spatial solitary-wave optical memory," *JOSA B*, vol. 7, no. 7, pp. 1328–1335, 1990.
[107] G. McDonald and W. Firth, "Switching dynamics of spatial solitary wave pixels," *JOSA B*, vol. 10, no. 6, pp. 1081–1089, 1993.
[108] S. Wabnitz, "Suppression of interactions in a phase-locked soliton optical memory," *Opt. Lett.*, vol. 18, no. 8, pp. 601–603, 1993.
[109] M. S. G. Jang J. K., Erkintalo M. and C. S., "Transient dynamics of cavity soliton merging," in *Advanced Photonics Congress*, p. JTu6A.7, Optical Society of America, 2014.
[110] T. Tamir, *Guided-wave optoelectronics*, vol. 26. Springer, 1988.
[111] M. Abramowitz and I. A. Stegun, *Handbook of mathematical functions: with formulas, graphs, and mathematical tables*, vol. 55. Courier Corporation, 1964.
[112] R. Hardin and F. Tappert, "Applications of the split-step fourier method to the numerical solution of nonlinear and variable coefficient wave equations," *Siam Rev*, vol. 15, no. 1, pp. 423–429, 1973.
[113] A. Grudinin, D. Richardson, and D. N. Payne, "Energy quantisation in figure eight fibre laser," *Electronics Letters*, vol. 28, no. 1, pp. 67–68, 1992.
[114] E. Zemlyanaya and I. Barashenkov, "Traveling solitons in the damped-driven nonlinear schrödinger equation," *SIAM Journal on Applied Mathematics*, vol. 64, no. 3, pp. 800–818, 2004.
[115] L. Pontriagin and L. V. Rodygin, "Approximate solution of a system of ordinary differential equations involving a small parameter using derivatives," *Doklady Akademii Nauk SSSR*, vol. 131, no. 2, pp. 255–258, 1960.
[116] T. Carmon, L. Yang, and K. Vahala, "Dynamical thermal behavior and thermal self-stability of microcavities," *Opt. Express*, vol. 12, no. 20, pp. 4742–4750, 2004.

[117] F. Riehle, *Frequency standards: basics and applications*. John Wiley & Sons, 2006.
[118] E. D. Black, "An introduction to pound–drever–hall laser frequency stabilization," *American Journal of Physics*, vol. 69, no. 1, pp. 79–87, 2001.
[119] T. Hansson and S. Wabnitz, "Bichromatically pumped microresonator frequency combs," *Physical Review A*, vol. 90, no. 1, p. 013811, 2014.
[120] Y. Okawachi, M. Yu, K. Luke, D. O. Carvalho, S. Ramelow, A. Farsi, M. Lipson, and A. L. Gaeta, "Dual-pumped degenerate kerr oscillator in a silicon nitride microresonator," *Optics letters*, vol. 40, no. 22, pp. 5267–5270, 2015.
[121] S. Wang, H. Guo, X. Bai, and X. Zeng, "Broadband kerr frequency combs and intracavity soliton dynamics influenced by high-order cavity dispersion," *Optics letters*, vol. 39, no. 10, pp. 2880–2883, 2014.
[122] C. Milián and D. Skryabin, "Soliton families and resonant radiation in a micro-ring resonator near zero group-velocity dispersion," *Optics express*, vol. 22, no. 3, pp. 3732–3739, 2014.
[123] P. Parra-Rivas, D. Gomila, F. Leo, S. Coen, and L. Gelens, "Third-order chromatic dispersion stabilizes kerr frequency combs," *Optics letters*, vol. 39, no. 10, pp. 2971–2974, 2014.
[124] Y. Okawachi, M. R. Lamont, K. Luke, D. O. Carvalho, M. Yu, M. Lipson, and A. L. Gaeta, "Bandwidth shaping of microresonator-based frequency combs via dispersion engineering," *Optics letters*, vol. 39, no. 12, pp. 3535–3538, 2014.
[125] M. Erkintalo, Y. Xu, S. Murdoch, J. Dudley, and G. Genty, "Cascaded phase matching and nonlinear symmetry breaking in fiber frequency combs," *Physical review letters*, vol. 109, no. 22, p. 223904, 2012.
[126] J. M. Dudley, G. Genty, and S. Coen, "Supercontinuum generation in photonic crystal fiber," *Reviews of modern physics*, vol. 78, no. 4, p. 1135, 2006.
[127] A. Blanco-Redondo, C. M. de Sterke, J. E. Sipe, T. F. Krauss, B. J. Eggleton, and C. Husko, "Pure-quartic solitons," *Nature communications*, vol. 7, 2016.
[128] A. Savchenkov, A. Matsko, W. Liang, V. Ilchenko, D. Seidel, and L. Maleki, "Kerr frequency comb generation in overmoded resonators," *Optics express*, vol. 20, no. 24, pp. 27290–27298, 2012.
[129] N. Akhmediev and M. Karlsson, "Cherenkov radiation emitted by solitons in optical fibers," *Physical Review A*, vol. 51, no. 3, p. 2602, 1995.
[130] A. B. Matsko and L. Maleki, "Noise conversion in kerr comb rf photonic oscillators," *JOSA B*, vol. 32, no. 2, pp. 232–240, 2015.
[131] L. N. Trefethen, *Spectral methods in MATLAB*, vol. 10. Siam, 2000.
[132] T. I. Lakoba, "Instability analysis of the split-step fourier method on the background of a soliton of the nonlinear schrödinger equation," *Numerical Methods for Partial Differential Equations*, vol. 28, no. 2, pp. 641–669, 2012.
[133] T. I. Lakoba, "Instability of the finite-difference split-step method applied to the nonlinear schrödinger equation. i. standing soliton," *Numerical Methods for Partial Differential Equations*, 2015.
[134] L. Maleki, A. Savchenkov, V. Ilchenko, W. Liang, D. Eliyahu, A. Matsko, D. Seidel, N. Wells, J. Camparo, and B. Jaduszliwer, "All-optical integrated rubidium atomic clock," in *2011 Joint Conference of the IEEE International*

Frequency Control and the European Frequency and Time Forum (FCS) Proceedings, pp. 1–5, IEEE, 2011.

[135] A. Savchenkov, D. Eliyahu, W. Liang, V. Ilchenko, J. Byrd, A. Matsko, D. Seidel, and L. Maleki, "Miniature optical atomic clock: Stabilization of a kerr comb oscillator," *arXiv preprint arXiv:1301.3198*, 2013.

[136] M. A. Foster, A. C. Turner, J. E. Sharping, B. S. Schmidt, M. Lipson, and A. L. Gaeta, "Broad-band optical parametric gain on a silicon photonic chip," *Nature*, vol. 441, no. 7096, pp. 960–963, 2006.

[137] H. Zhao, B. Kuyken, S. Clemmen, F. Leo, A. Subramanian, A. Dhakal, P. Helin, S. Severi, E. Brainis, G. Roelkens, *et al.*, "Visible-to-near-infrared octave spanning supercontinuum generation in a silicon nitride waveguide," *Optics letters*, vol. 40, no. 10, pp. 2177–2180, 2015.

[138] L. Zhang, Y. Yue, R. G. Beausoleil, and A. E. Willner, "Flattened dispersion in silicon slot waveguides," *Optics express*, vol. 18, no. 19, pp. 20529–20534, 2010.

[139] C. Bao, Y. Yan, L. Zhang, Y. Yue, N. Ahmed, A. M. Agarwal, L. C. Kimerling, J. Michel, and A. E. Willner, "Increased bandwidth with flattened and low dispersion in a horizontal double-slot silicon waveguide," *JOSA B*, vol. 32, no. 1, pp. 26–30, 2015.

[140] X. Xue, Y. Xuan, Y. Liu, P.-H. Wang, S. Chen, J. Wang, D. E. Leaird, M. Qi, and A. M. Weiner, "Mode-locked dark pulse kerr combs in normal-dispersion microresonators," *Nature Photonics*, vol. 9, no. 9, pp. 594–600, 2015.

[141] X. Xue, Y. Xuan, P.-H. Wang, Y. Liu, D. E. Leaird, M. Qi, and A. M. Weiner, "Normal-dispersion microcombs enabled by controllable mode interactions," *Laser Photonics Rev.*, vol. 9, no. 4, pp. L23–L28, 2015.

[142] S. A. Miller, Y. Okawachi, S. Ramelow, K. Luke, A. Dutt, A. Farsi, A. L. Gaeta, and M. Lipson, "Tunable frequency combs based on dual microring resonators," *Optics express*, vol. 23, no. 16, pp. 21527–21540, 2015.

[143] M. Soltani, A. Matsko, and L. Maleki, "Enabling arbitrary wavelength frequency combs on chip," *Laser & Photonics Reviews*, vol. 10, no. 1, pp. 158–162, 2016.